Universität Hamburg

DER FORSCHUNG | DER LEHRE | DER BILDUNG

Protein corona formation on nanoparticles with different surface chemistry

Dissertation

zur Erlangung des Doktorgrades

an der Fakultät für Mathematik, Informatik und Naturwissenschaften

Fachbereich Chemie

der Universität Hamburg

vorgelegt von

M.Sc. Chenxi Yang

- Hamburg, 2024

GUTACHTER DER DISSERTATION:

Prof. Dr.Wolfgang J. Parak

Dr. Florian Schulz

MITGLIEDER DER PRÜFUNGSKOMMISSION:

Prof. Dr. Wolfgang J. Parak

Prof. Dr. Tobias Beck

Prof. Dr. Nadja C. Bigall

DATUM DER DISPUTATION:

15.11.2024

LEITER DES FACHBEREICHS PHYSIK:

Prof. Dr. Markus Fischer

DEKAN DER MIN-FAKULTÄT:

Prof. Dr.-Ing. Norbert Ritter

Biliography

Personal information			
Name	Chenxi	Family name	Yang
Birthplace	Hengyang, Hunan, China	Nationality	Chinese
Education			
12.2020-03.2024	University of Hamburg, AG Biophotonics (Prof. Dr. Wolfgang J. Parak), Germany		
	Doctor of Natural Sciences		
09.2017-06.2020	China Pharmaceutical University, China		
	Master of Science		
09.2013-06.2017	China Pharmaceutical University, China		
	Bachelor of Science		

Abstract

Nanomaterials have found extensive application in medicine, biology, and the chemical industry, which has led to a growing interest in exploring their behavior within biological environments. In recent years, significant progress has been made in the physical and chemical modification of biomaterial surfaces to enhance their interactions with complex biological environment. There is urgent need to focus on studying the interactions between nanomaterial surfaces and biological environments in order to provide essential insights for enhancing performance and advancing the applications of nanomaterials.

This thesis presents a comprehensive investigation into the protein corona formation, which illustrates the dynamic interaction between nanoparticles and proteins. First, various surface chemical modifications were performed on quantum dots with intrinsic fluorescence properties to endow them with different surface physicochemical characteristics, such as surface charge and hydrophilicity. Subsequently, these modified quantum dot-based nanoparticles were exposed to specific proteins under varying pH conditions. Fluorescence correlation spectroscopy (FCS) was used to track the formation process of protein corona on the surface of the nanoparticles, providing us with systematic and accurate understanding of protein corona formation.

Protein corona formation is a multifaceted process influenced by various factors, including the properties of the nanomaterial, the type of protein, and the specific biological environment. By investigating the dynamic process of protein corona formation under distinct conditions, we can gain a deeper and more comprehensive understanding of the determinants behind this phenomenon. This knowledge enables us to effectively modulate the formation of protein corona, either to mitigate or enhance it, in the design and utilization of nanomaterials in diverse application.

Zusammenfassung

Nanomaterialien finden in der Medizin, Biologie und der chemischen Industrie breite Anwendung, was zu einem wachsenden Interesse an der Erforschung ihres Verhaltens in biologischen Umgebungen geführt hat. In den letzten Jahren wurden erhebliche Fortschritte bei der physikalischen und chemischen Modifizierung von Biomaterialoberflächen erzielt, um ihre Wechselwirkungen mit komplexen biologischen Umgebungen zu verbessern. Es besteht dringender Bedarf, sich auf die Untersuchung der Wechselwirkungen zwischen Nanomaterialoberflächen und biologischen Umgebungen zu konzentrieren, um wichtige Erkenntnisse zur Leistungssteigerung und Weiterentwicklung der Anwendung von Nanomaterialien zu gewinnen.

Diese Arbeit präsentiert eine umfassende Untersuchung der Proteinkoronabildung, die die dynamische Wechselwirkung zwischen Nanopartikeln und Proteinen veranschaulicht. Zunächst wurden verschiedene chemische Oberflächenmodifikationen an Quantenpunkten mit intrinsischen Fluoreszenzeigenschaften durchgeführt, um ihnen unterschiedliche physikochemischen Oberflächeneigenschaften wie Oberflächenladung und Hydrophilie zu verleihen. Anschließend wurden diese modifizierten Nanopartikel auf Quantenpunktbasis unter unterschiedlichen pH-Bedingungen bestimmten Proteinen ausgesetzt. Mithilfe der Fluoreszenzkorrelationsspektroskopie (FCS) wurde der Bildungsprozess der Proteinkorona auf der Oberfläche der Nanopartikel verfolgt, was uns ein systematisches und genaues Verständnis der Proteinkoronabildung ermöglichte.

Die Bildung einer Proteinkorona ist ein vielschichtiger Prozess, der von verschiedenen Faktoren beeinflusst wird, darunter den Eigenschaften des Nanomaterials, der Art des Proteins und der spezifischen biologischen Umgebung. Indem wir den dynamischen Prozess der Proteinkoronabildung unter bestimmten Bedingungen untersuchen, können wir ein tieferes und umfassenderes Verständnis der Determinanten hinter diesem Phänomen erlangen. Dieses Wissen ermöglicht es uns, die Bildung der Proteinkorona bei der Entwicklung und Nutzung von Nanomaterialien in verschiedenen Anwendungen effektiv zu modulieren, um sie entweder zu mildern oder zu verstärken.

Abbreviations

FCS	Fluorescence correlation spectroscopy
MUA	11-Mercaptoundecanoic acid
PEG	Polyethylene glycol
PMA	poly (isobutylene-alt-maleic anhydride)
BSA	Bovine Serum Albumin
SDS-PAGE	Sodium dodecyl sulfate–polyacrylamide gel electrophoresis
UV-vis	Ultraviolet–visible spectroscopy
FTIR	Fourier Transform Infrared Spectroscopy
nm	Nanometers
Kda	Kilodalton
pl	Isoelectric point
K_d	Dissociation constant
QDs	Quantum dots
NPs	Nanoparticles
PBS	Phosphate buffer saline
IFT	Interfacial tension
Rh6G	Rhodamine 6G
TEM	Transmission electron microscopy
TBP	Tributylphosphin
ζ	Zeta potential
EDC	1-ethyl-3-(3-dimethylaminopropyl) carbodiimide
NHS	N-hydroxysuccinimide
ACF	Autocorrelation function
CLSM	Confocal Laser Scanning Microscopy

Contents

1. Motivation and Scope of the Work

In recent years, nanoparticles (NPs) have emerged as promising candidates for a wide range of biomedical and environmental applications, including drug delivery, clinical diagnostics, and pollution mitigation. However, they often fail to fully realize their efficacy in biological environments, primarily due to our inadequate understanding of the interactions between nanomaterials, nanomedicines, and the biological environment. Central to this understanding is the protein corona—a dynamic biomolecular layer surrounds NPs when exposed to biological fluids. The protein corona not only determines the physicochemical properties of NPs but also governs their fate and functionality in biological systems.

In biological systems, protein coronas are often composed of multiple proteins forming monolayer or multilayer structures. These protein coronas modify the physicochemical identities of NPs, including particle's size, surface charge, hydrophilicity and aggregation behavior. As a result, the interaction between NPs and biological systems also changes. The development of protein coronas is influenced by various factors, such as pH, time, temperature, protein composition, concentration, and other environmental conditions. In addition, the intrinsic properties of NPs, such as their size, shape, and surface chemistry, also play an important role. Each element significantly affects the composition and formation of the protein corona. Therefore, a deeper understanding of the formation mechanism of the protein corona and the factors that influence it has become a key area of nanomaterial research. By understanding these mechanisms and factors, we can better determine how to regulate various conditions for specific applications.

The growing interest in exploring the potential of NPs for a variety of applications has underscored the urgent need for deeper exploration of the complex interaction between NPs and the surrounded protein corona. By unraveling the composition, structure, and dynamics of the protein corona, we can elucidate how it regulates the uptake and recognition of NPs by cells, thereby affecting their biodistribution and pharmacokinetics. Furthermore, we can investigate how the protein corona affects the biological responses to NPs, including immune recognition, inflammatory responses, and cellular signaling pathways. Given that the protein corona formation can also affect the toxicity of NPs, research in this area is critical for mitigating the adverse effects of nanomedicines on human health. In addition, insights gained from studying the protein corona can inform the design of NPs with tailored surface properties, improved biocompatibility, and enhanced therapeutic efficacy.

Protein coronas can be studied using a variety of techniques, including direct and indirect detection methods. By using complementary characterization techniques, we can more comprehensively and deeply study the dynamic process of protein corona formation, thereby fully understanding the interaction between NPs and the biological environment, especially the interaction with proteins.

By thoroughly exploring the dynamic process of protein corona formation, we aim to pave the way for the rational design of NPs for various biomedical and environmental applications. Through interdisciplinary collaboration and innovative methods, we aim to investigate the differences in protein corona formation of nanoparticles with different surface chemistry. In this thesis, we selected cadmium selenide-cadmium sulfide core-shell structure quantum dots with autofluorescence properties as the research object, we further designed and synthesized a series of polymers or cap ligands with different physicochemical properties to coat the surface of quantum dots, they can be divided into three research systems.

First, a series of polymers based on poly (isobutylene-maleic anhydride) backbone were designed and synthesized, and each polymer has different surface charges by changing the composition of the polymers. Afterwards, these polymers were fully characterized to gain a preliminary understanding of their physicochemical properties. Taking advantage of their unique amphiphilic structure, these polymers were able to be coated on hydrophobic quantum dots through hydrophobic interactions, thereby achieving a phase transition from organic solvent to aqueous solution of quantum dots NPs to further investigate protein corona formation. In the second system, the surface of water-soluble quantum dot NPs was further modified with polyethylene glycol or biotin to make them resistant to protein adsorption or have specific affinity for avidin molecules. And for the third system, two water-soluble quantum dots were synthesized by cap exchange method to compare the effects of polymer coating and direct ligand exchange on the formation of protein coronas.

Throughout the study, NPs with different surface chemistries were fabricated, including different surface charges, polymer compositions, and targeted molecular modifications. This variation in surface properties facilitated the subsequent comparison and evaluation of protein corona formation. When selecting the proteins to be evaluated, in order to take the effects of different protein properties into account on protein corona formation, we ultimately chose five proteins with different physicochemical properties and evaluated the protein corona formation process. Due to the complexity of the physiological environment, environmental factors also need to be considered. Therefore, we studied the pH-dependent protein corona formation process to summarize and analyze the formation behavior of protein coronas on NPs with different surface modifications.

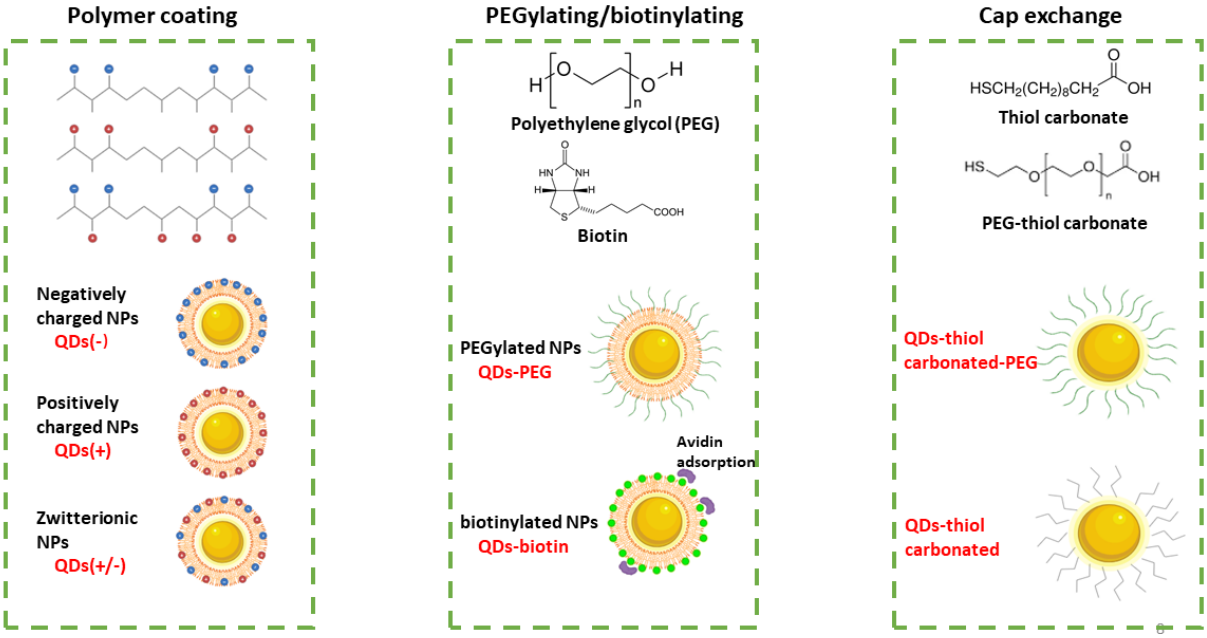

Figure 1-1. Schematic of research work.

The findings presented in this thesis provide new insights and perspectives for the application of NPs in biological environments. They also contribute to enrich the practical experience for the design and surface modification of NPs.

2. Background of Nanoparticles-Proteins' interaction

2.1 Nanoparticles

Nanoparticles (NPs) are defined as particles ranging in size from 1 to 100 nanometers (nm) that possess unprecedented properties and have become a transformative class of materials with applications in a wide range of science and technology, from life sciences to chemical engineering.[1-3] The unique size-dependent characteristics and high surface area-to-volume ratio of NPs, offering countless possibilities for innovation and advancement.[4] This thesis explores the synthesis, modification and characterization of NPs, and further uncovering their potential interaction with biological environment.

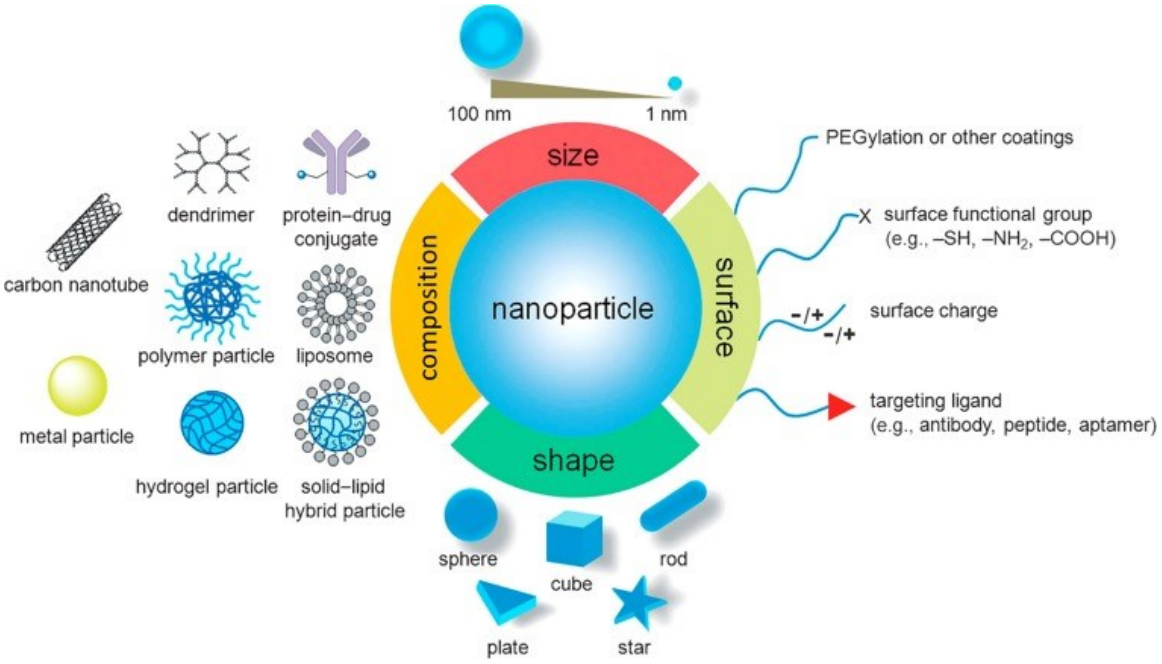

Figure 2-1. overview of nanoparticles.[1]

Diverse types of materials can be used to synthesize different kinds of NPs, each possessing distinctive properties and various range of applications. Metallic NPs, including gold, silver, and platinum NPs, exhibit exceptional catalytic activity, optical properties, and antimicrobial efficacy, making them indispensable in catalysis and biomedicine applications.[5, 6] Xiao Yen et al. improved the photothermal properties of gold NPs through the induction of aggregation, successfully enhancing their effectiveness for tumor ablation.[7] Abu Bakar Siddique and his colleagues synthesized silver NPs through an ecofriendly synthesis route, showcasing their notable photocatalytic and antibacterial properties.[8] Carbon-based NPs, such as fullerenes, carbon nanotubes, and graphene, have excellent mechanical, electrical, and thermal properties, making them as key

components in energy storage, electronics, and composite materials.[9-11] Guoqiang Song et al. used dopamine (DA) as a carbon source to synthesize hierarchical hollow carbon structures that encapsulate carbon nanotubes (CNTs) in situ, making them well-suited for high-performance supercapacitor applications.[12] Hualiang Lv and colleagues synthesized a nanoporous bilayer graphene superlattice featuring partially overlapped pores, which enables ultrathin electromagnetic absorption, efficient electromagnetic energy harvesting and conversion, low- to medium-temperature thermoelectric properties, as well as applications in photoluminescence and optoelectronic devices.[13] Polymer NPs are known for their excellent biocompatibility and stability, they also have variety of application in drug delivery systems, gene therapy platforms, and functional coatings.[14-16] Jafari-Gharabaghlou, D and colleagues utilized folate-functionalized PLGA-PEG nanoparticles to deliver metformin, significantly enhancing its therapeutic efficacy in breast cancer treatment.[17] Semiconductor NPs, such as quantum dots (QDs), have tunable optical properties, which are ideally for solar cells, Light-emitting diodes, and bioimaging applications.[18-20]

Among semiconductor nanomaterials, QDs have attracted much attention in recent years due to their unique optical and electronic properties. These nanoscale particles, which are typically between 2 and 10 nm in size, have size-dependent fluorescence properties, making them a promising candidate for a wide range of applications in biomedicine and materials science.[21, 22] When QDs are excited by an external light source, they absorb energy and elevate electrons to a higher energy state. When the electrons return to the ground state, they emit light at specific wavelengths that depend on the size of the QDs. Smaller dots emit shorter wavelengths of light, while larger dots emit longer wavelengths.[23] This ability to tailor fluorescence based on size has significant advantages among a variety of applications. In the field of biomaterials, QDs can be used as fluorescent labels for applications, including live cell imaging, in vivo imaging, and biomolecular sensors, where their high photostability, brightness, and broad absorption spectra and narrow tunable emission spectra make them superior to traditional organic fluorophores.[24, 25] In addition, their superior photophysical properties give them multiplexing capabilities, allowing for the simultaneous detection of multiple targets in biological samples.

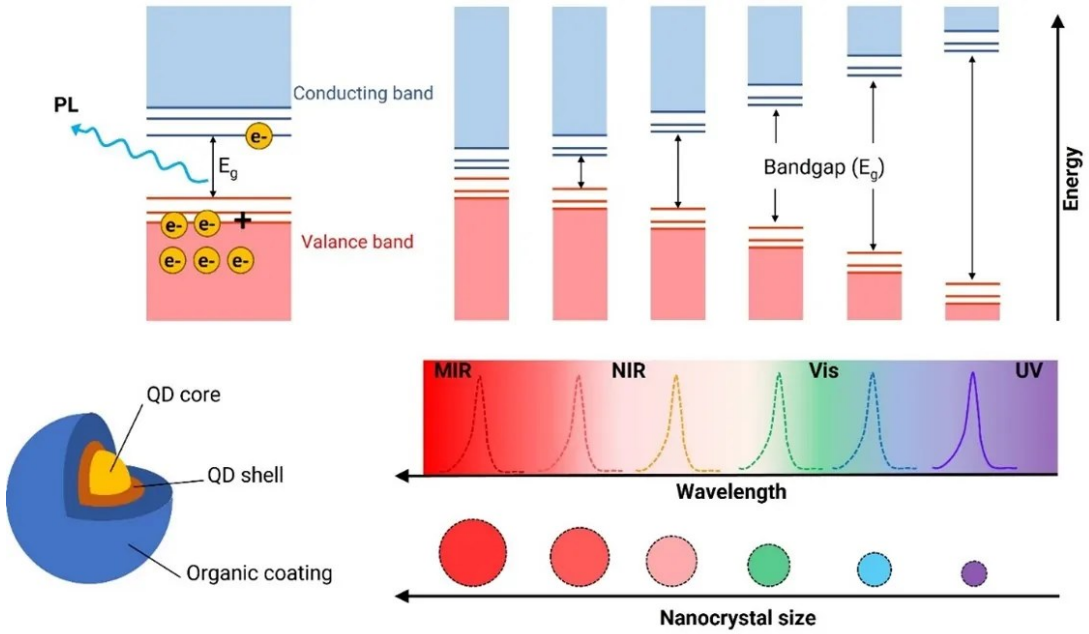

Figure 2-2. The luminescence mechanism of quantum dots. Source: Semiconductor Engineering.

As the frontier of nanoscience and nanotechnology continues to expand, NPs stand at the cutting edge of innovation, providing unprecedented opportunities for new materials, devices, and biological applications. This thesis aims to shed light on the synthesis, characterization, and interactions of NPs with biological environments, demonstrating their potential applications. By exploring the multifaceted nature of NPs across various research fields, this research aims to provide valuable insights into the extraordinary capabilities of NPs and their profound impact on advancing knowledge and promoting a sustainable future.

2.2 Surface chemistry on nanoparticles

Nanoparticles (NPs) have unique size-dependent properties and highly reactive surfaces that enable wide range of functions and applications. The surface chemistry of NPs is particularly important, as it determines their interactions with the surrounding environment, biological systems, and other materials, thereby influencing their reactivity, stability, and functionality. A comprehensive understanding of surface chemistry and the ability to modify surfaces have opened up new avenues for the application of NPs across diverse fields.

Surface modification of NPs includes a variety of methods, including physical adsorption, which relies on weak van der Waals forces or electrostatic interactions to attach molecules to the surface of NPs. This approach allows molecules to attach reversibly, usually with weak binding forces. In this method, molecules such as surfactants

or polymers are usually dissolved or dispersed in the same solvent as the NPs, and after mixing them together, the molecules adhere to the surface of the NPs through non-covalent interactions, thereby achieving enhanced stability and solubility and dispersibility.[26, 27]

There are also some chemical functionalization methods that involve the formation of covalent bonds between the surface atoms of the NPs and functional groups. This method can create more stable modifications than physical adsorption.[28, 29] Common strategies include the reaction of alkoxysilanes with oxide surfaces to form siloxane bonds, which is widely used to modify silica NPs.[30] As well as thiol-ene and thiol-click reactions, thiols group usually react with metal NPs to form strong covalent bonds, enhancing the stability of the NPs and allowing for further functionalization.[31]

Layer-by-layer (LbL) assembly is a technique that involves the sequential adsorption of oppositely charged polyelectrolytes onto the surface of NPs. By alternating layers of cationic and anionic polymers, multilayer structures are formed through electrostatic interactions, enabling the creation of controlled nanostructured coatings. This approach allows for precise regulation of both the thickness and composition of the NPs coatings, facilitating customization for specific applications. Consequently, LbL assembly can be effectively utilized in drug delivery systems and biosensing devices. [32, 33]

Ligand exchange is a widely used surface modification technique that involves replacing the original ligands bound to NPs with a different ligand. This process is particularly significant in the context of metal NPs, which typically have stabilizing ligands. The process is often driven by the relative binding affinities of the ligands, a ligand with higher binding affinity can effectively replace one with lower affinity, resulting in changes to the original properties of the NPs. [34, 35]

Polymer coating is an important surface modification strategy that involves enveloping NPs with polymer chains to create a protective layer. This method enhances the stability, solubility, and functionality of NPs, particularly in biological environments. The characteristics of the polymer can significantly influence the properties of the composite NPs by introducing various functional groups, ligands, or biomolecules on their surfaces. As a result, the physicochemical properties and interactions of the NPs with their surrounding environment can be altered.[36-38]

By manipulating the surface chemistry, researchers can optimize performance, enhance stability, and introduce functional groups that were previously unattainable. This customization allows NPs to be tailored to meet the specific requirements of diverse applications, resulting in more efficient, selective, and versatile tools for scientific and technological progress. By precisely controlling and modifying the surfaces of NPs, researchers can facilitate breakthrough discoveries and innovations across multiple disciplines, ultimately advancing science and technology.

2.3 Protein corona

When NPs are exposed to biological environments, they will inevitably interact with biomolecules including proteins and peptides, leading to a phenomenon known as the protein corona.[39]

The term “protein corona” is derived from the Latin word “corona,” meaning “crown.” The nomenclature metaphorically describes how proteins form a layer or “crown” around NPs when they enter a biological environment, especially fluids such as blood or serum. The concept emphasizes the idea that, like a crown surrounding a head, a protein corona surrounds a NP, fundamentally changing its biological identities and fate within a living system.

The formation of a protein corona deeply influences the interaction of the NP with surrounding biological matter, including cells, tissues, even the immune system.[40, 41] Rather than being a passive entity, the protein corona actively controls the fate of the NPs in vivo, therefore, understanding the dynamics of protein corona formation is critical to advancing nanomedicine and ensuring the effective application of nanotechnology in biological environments.[42, 43] This thesis explores the complex interactions between NPs and the protein corona, highlighting its significance in biomedical applications.

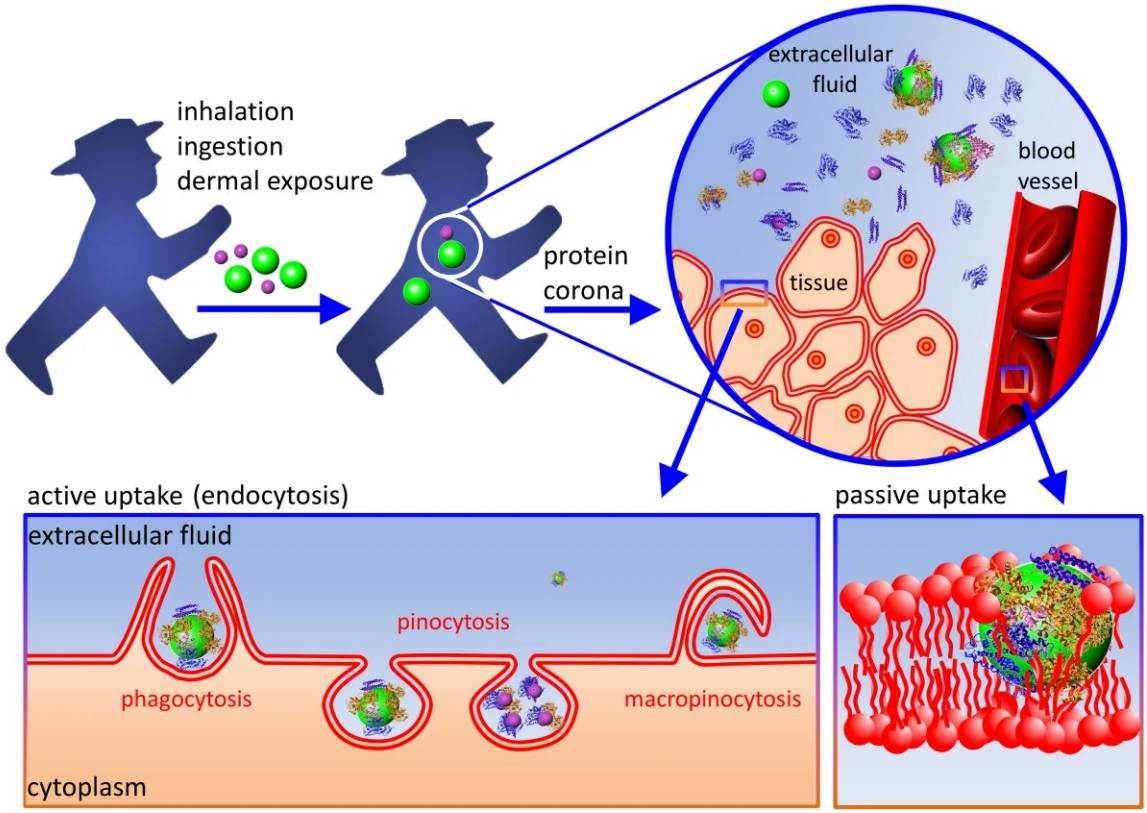

Figure 2-3. Formation of protein corona in vivo. [39]

The protein corona is comprised of two distinct layers: the hard corona and the soft corona.[44, 45] The hard corona is the inner layer, closely associated with the NPs, and generally exhibits higher affinity for the nanoparticles. In contrast, the soft corona is the outer layer, where the proteins typically have lower affinity for the NPs and exist in a dynamic equilibrium of adsorption and desorption. This competitive protein adsorption phenomenon is described as Vroman effect.[46, 47] The formation of the protein corona is a dynamic and complex process. Typically, proteins with greater mobility are the first to interact with the NPs surface, adhering to the material through various physical and chemical interactions between the proteins and the NPs surface. These initially adsorbed proteins are often replaced by proteins that exhibit a higher affinity for the surface over time. [48, 49] Once proteins are adsorbed onto the NPs surface, they may undergo conformational changes or even lose their original biological identities.[50]

Additionally, the space between adsorbed proteins becomes available for new proteins to bind to the surface. This process can lead to desorption, where proteins detach from the NPs surface. In understanding protein adsorption, it is essential to consider various protein characteristics, including size, charge, mobility, stability, and the

specific structure and composition of different protein domains that comprise the protein's tertiary structure.

The protein corona not only masks the original surface of NPs but also imparts them with biological properties, thereby dictating their interactions with cells, tissues, and biological barriers.

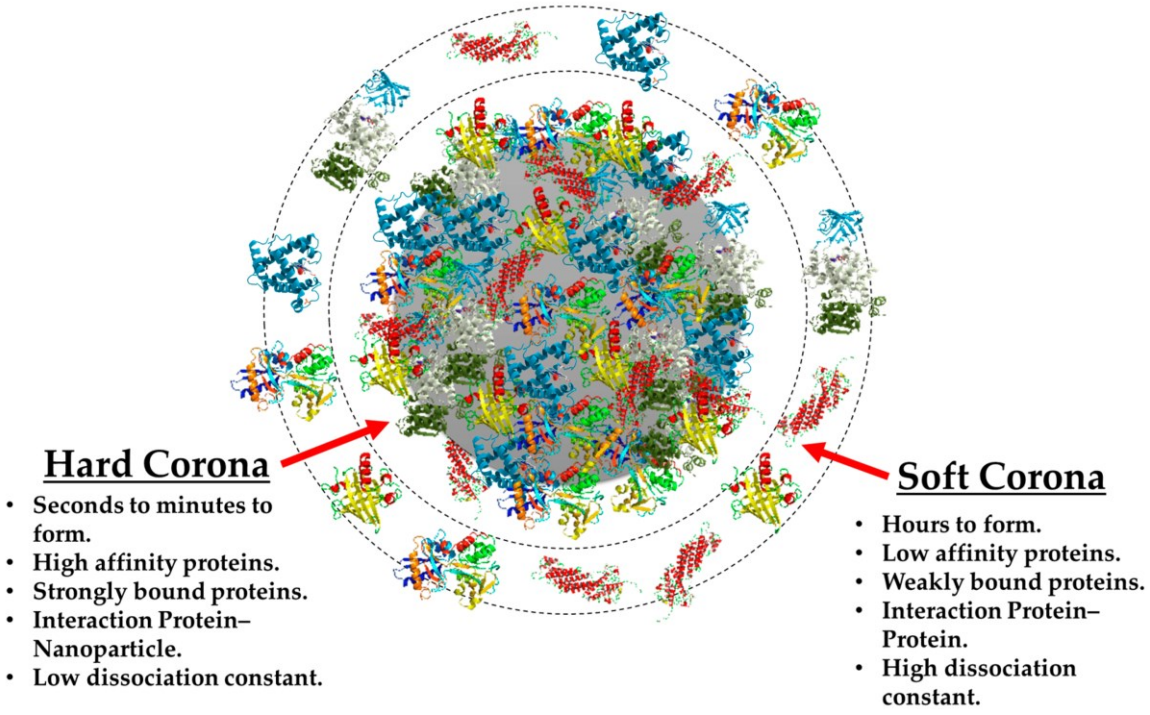

Figure 2-4. Comparison of the “hard” corona and the “soft” corona.[51]

In the realm of nanomedicine, the protein corona has profound implications for the design and efficacy of NPs-based therapeutics, drug delivery systems, and diagnostic agents. By modulating the protein corona, researchers can enhance the biological stability, targeting specificity, and therapeutic efficacy of NPs, leading to advancements in precision medicine, cancer therapy, and regenerative medicine. Furthermore, understanding the protein corona can help predict the biological fate and toxicity of NPs in vivo, guiding the development of safe and effective nanomedicines.

The protein corona represents a dynamic interface between NPs and biological systems, exerting profound influences on their biological behavior, therapeutic efficacy, and environmental fate. This thesis aims to unravel the complexities of protein corona formation on NPs, highlighting its significance for biomedical applications. By deeply exploring the protein corona interactions, this research aims to advance our

understanding of the nanointerface and its implications for developing safe and effective nanotechnologies.

2.4 Protein corona factors

The composition and formation of a protein corona around NPs is a complex process mediated by a variety of physicochemical and biological factors.[52] Understanding these factors is essential for predicting the interactions between NPs and biological systems, also pave the way for optimizing the design of nanomedicines and nanocarriers. The protein corona can significantly influence the biodistribution, immunogenicity, and therapeutic efficacy of NPs, thus underscoring the importance of recognizing the parameters that govern its formation.

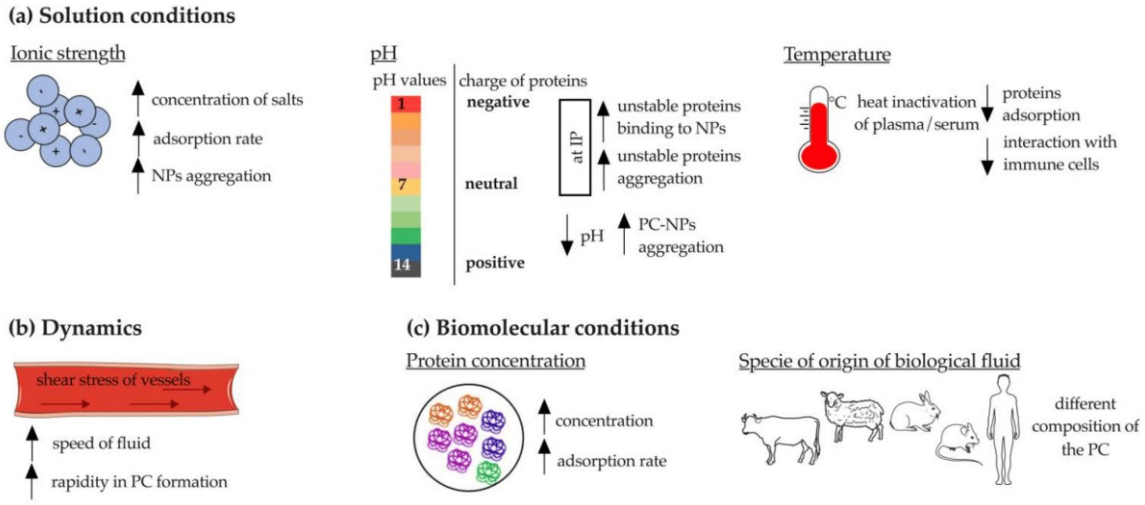

Figure 2-5. Extrinsic factors affecting the protein corona formation.[52]

Several main factors impact the protein corona formation, including the characteristics of NPs, the nature of the biological fluid, and environmental conditions.

The intrinsic properties of NPs significantly influence the composition and structure of the protein corona. The size of the NPs affects their surface area-to-volume ratio, impacting protein adsorption kinetics. smaller NPs generally have higher surface energy and greater surface area, which can enhance protein binding, while larger ones may face steric hindrance hindering adsorption.[53] Additionally, morphology of NPs also alters protein corona's orientation and composition.[54] The NPs' surface charge is crucial for electrostatic interactions, theoretically, positively charged particles attract negatively charged proteins, while negatively charged ones can repel them, influencing adsorption stability.[55] Furthermore, the chemical composition, hydrophobicity/hydrophilicity, and surface modifications of NPs such as coatings with polyethylene glycol or specific

antibodies can optimize protein binding and enhance biocompatibility or target specific proteins, thus altering the protein corona's properties.[56, 57]

Secondly, the biological environment surrounding the NPs is vital for protein corona formation. Various biological fluids contain distinct types and concentrations of proteins that influence NPs adsorption. High-abundance proteins can dominate the adsorption process, significantly altering the overall composition of the protein corona. As protein concentration increases, competition for binding sites on the NPs surface, affecting the distribution of proteins in the corona. This competitive adsorption process impacts the stability and dynamic distribution of both the hard and soft coronas.[58, 59]

Lastly, the physical and chemical environment around NPs can significantly influence protein corona dynamics. For instance, variations in pH can modify the surface charge of both proteins and NPs, impacting their interactions.[50] Ionic strength can also affect protein stability and conformational changes during adsorption. Temperature plays a crucial as well, higher temperature can enhance protein mobility and accelerate adsorption, whereas extreme temperatures may denature proteins, altering their binding properties and overall behavior in the corona.[50]

The formation of protein corona around NPs is a multifaceted process that is influenced by the interplay of NP characteristics, biofluid properties, and environmental conditions. A comprehensive understanding of these factors is essential for the rational design of NPs for biomedical applications, allowing researchers to predict and control NPs behavior in biological systems. With the rapid development of nanomedicine, elucidating the factors that influence protein corona formation will be critical to improving the efficacy and safety of nanotherapeutics.

3. Techniques for the experimental investigation of the protein corona

3.1 Basics

Studying the protein corona using advanced detection methods provides crucial insights into the composition and adsorption amounts of proteins on NPs. Research methodologies in this field can be categorized into two main types: direct measurements and indirect measurements.[60]

Direct measurements involve the explicit analysis of proteins that are adsorbed onto the surface of NPs. This approach allows for the acquisition of structural information and enables both quantitative and qualitative analyses of the proteins present. However, to minimize interference from unbound proteins in the solution, it is usually necessary to purify the protein corona and separate the protein-bound NPs from the free proteins.[43, 61] This purification step is essential for accurately determining the composition and concentration of the protein corona.

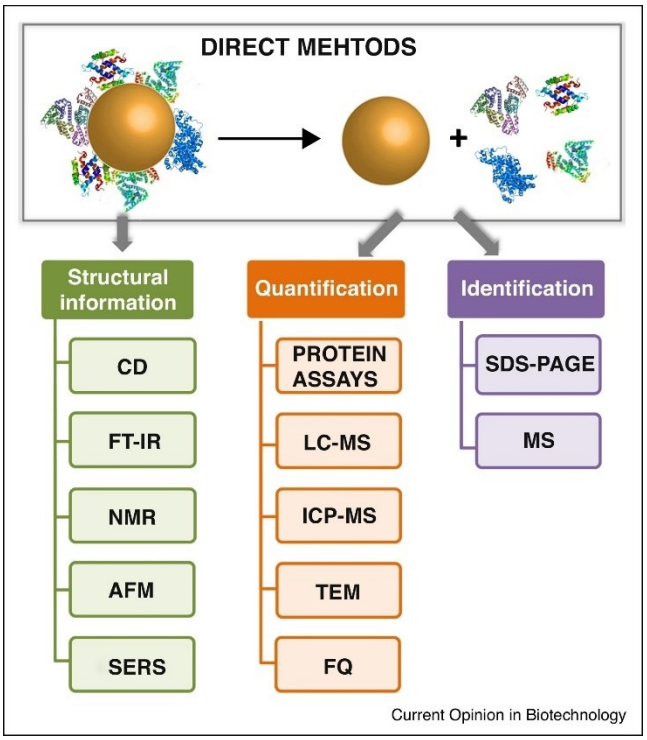

Figure 3-1. Summary of direct methods. [60]

In contrast, indirect measurements examine the protein corona by analyzing changes in the physical and chemical properties of NPs before and after protein corona formation. Key parameters assessed include variations in size, surface charge, density, absorbance,

and fluorescence. While this method eliminates the need for purification of the protein corona, it poses challenges for performing quantitative analyses of the protein composition.

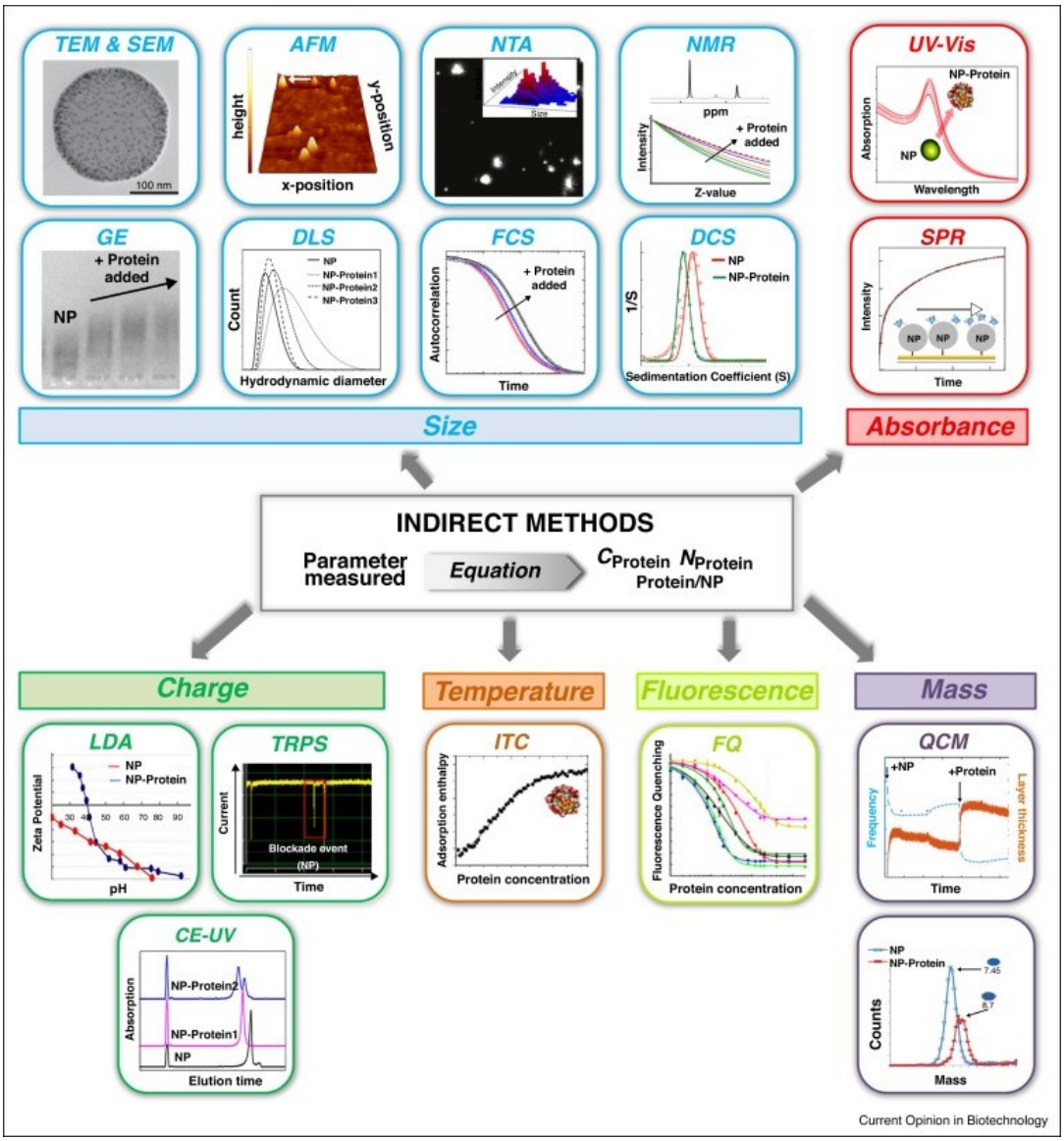

Figure 3-2. Summary of indirect methods.[60]

A range of experimental techniques has been developed to investigate the protein corona on NPs, each offering unique advantages for exploring various aspects of its formation and composition. For instance, high-throughput screening methods such as proteomics and mass spectrometry enable the identification and quantification of proteins within the corona, providing valuable insights into protein composition and abundance. Techniques like fluorescence spectroscopy and surface plasmon resonance

(SPR) allow for real-time monitoring of protein binding kinetics and affinity to NPs, provides insights on dynamic interactions at the nanoscale.

Atomic force microscopy (AFM) and transmission electron microscopy (TEM) can visualize protein corona morphology and NP-protein complexes at high spatial resolution, thus enhancing our understanding of the corona formation process. Circular dichroism (CD) spectroscopy and Fourier transform infrared spectroscopy (FTIR) reveal information about protein secondary structure and conformational changes caused by NPs interactions, elucidating conformational changes before and after protein corona formation. In addition, dynamic light scattering (DLS) and zeta potential measurements provide insights into the size distribution, aggregation behavior, and surface charge of NP-protein complexes, thus elucidating changes in physicochemical properties before and after protein corona formation.

By utilizing a variety of analytical and biophysical methods, researchers can fully reveal the complexity of protein corona formation, composition, and behavior, providing key insights into nanoscale interactions that determine the biological and environmental fate of NPs. In this thesis, we used experimental techniques to elucidate the differences in protein corona formation on different NPs surfaces, emphasizing the effects of surface chemical modifications on protein corona formation, which will help deepen our understanding of NP-protein interactions and their applications in biomedical and environmental contexts.

3.2 Fluorescence correlation microscopy for protein corona study

Fluorescence correlation spectroscopy (FCS) is an advanced analytical technique that enables the study of molecular dynamics and interactions at the single-molecule level. In the fields of nanobiology and nanomedicine, FCS has emerged as an essential tool for investigating nanoparticle behavior, particularly their interactions with biomolecules such as proteins and the formation of protein corona.[62]

The structure of FCS is shown in Figure 3-8. In confocal laser scanning microscopy (CLSM), the excitation laser beam is focused into a small excitation volume, usually only about 1 femtoliter. The fluorescence emitted by the excited sample will be collected by the same objective lens used for excitation, and the unwanted signal will be blocked by

the pinhole on the back of the objective lens, and then the signal will be guided to a single point detector.

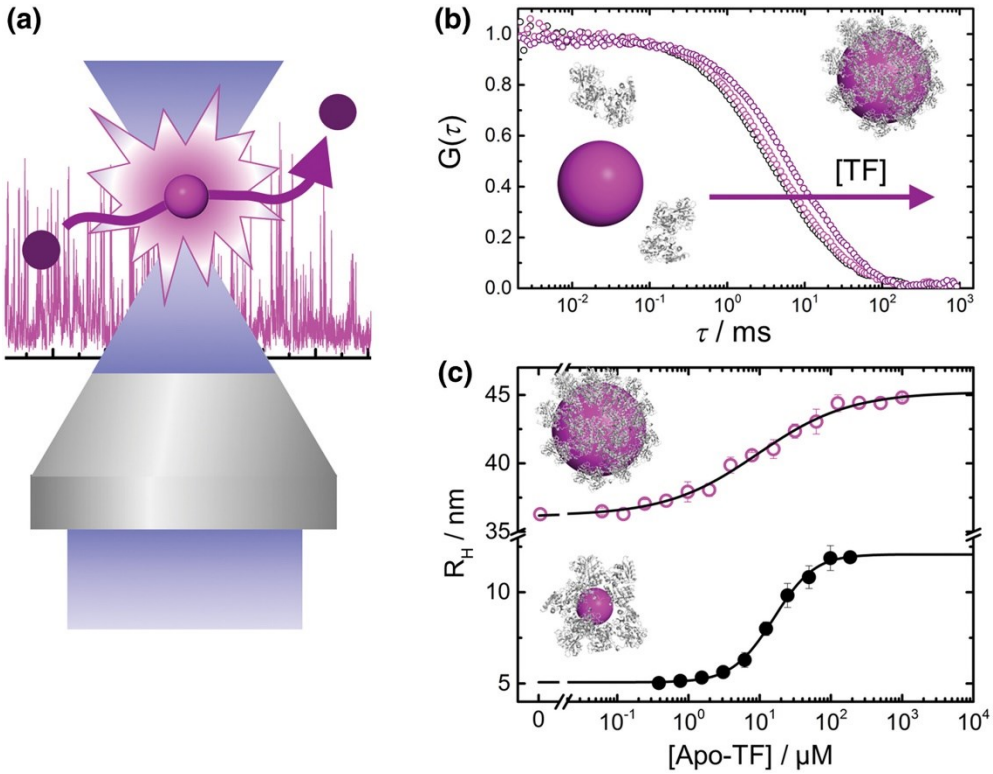

Figure 3-3. Principle of Fluorescence correlation spectroscopy (FCS).[62]

When studying the formation of protein coronas on nanoparticles, FCS presents a significant advantage as an indirect detection method for real-time monitoring of NPs-protein interactions. By incubating nanoparticles—either labeled with fluorescent dyes or exhibiting autofluorescence—with proteins, researchers can track the movement and binding of these molecules in solution without the need for sample separation to remove free proteins, thus facilitating an analysis of the dynamics of protein corona formation on the nanoparticle surface.

In FCS, the Brownian motion of particles entering and leaving the confocal volume generates signal fluctuations that are further analyzed mathematically. To better distinguish these fluctuations, it is best to perform experiments in FCS with samples at nanomolar concentrations or even lower to obtain accurate information. When mathematically treating signal fluctuations, we are looking at the average time of motion of any molecule that enters the confocal volume.

Since the emitted fluorescence intensity will vary due to these molecules randomly entering and leaving the confocal volume, the observed fluorescence intensity can be considered a time-dependent signal. The readout intensity $I(t)$ will fluctuate in the same way as the number of particles $N(t)$. These fluctuations can be described by the autocorrelation function (ACF), which quantifies the correlation between the intensity fluctuations at one time point and the fluctuations at subsequent time points.

$$G(\tau) = \frac{\langle I(t)I(t+\tau)\rangle}{\langle I(t)\rangle^2} \quad (3\text{-}1)$$

ACF can also be defined as the self-similarity after a given delay time τ. The brackets ⟨⟩ denote the time average. $I(t)$ is the fluorescence intensity at time t, $\langle I(t)\rangle$ is the average intensity. When τ is 0, the value of the ACF is at its maximum value.

$$G(0) = 1 \quad (3\text{-}2)$$

When τ is 0, we are comparing the signal to itself at the same moment, the intensity is perfectly correlated with itself. And when τ increases, $G(\tau)$ decreases accordingly, and the decay rate of $G(\tau)$ can provide insight into the dynamics of the molecules or NPs, including the rate of diffusion. When τ is very large, the fluorescence intensity at time t and $t+\tau$ are no longer correlated.

$$\lim_{\tau\to\infty} G(\tau) = 0 \quad (3\text{-}3)$$

The ACF typically exhibits an exponential decay for diffusing molecules or NPs.

$$G(\tau) = \frac{1}{1+\frac{\tau}{\tau D}} \quad (3\text{-}4)$$

τD is the characteristic time associated with the diffusion of the particles, related to how quickly the molecules or NPs move in and out of the observation volume.

When we use one photon excitation system, the diffusion time of fluorescent NPs governed by the following equation.

$$\tau D = \frac{\omega 0^2}{4D} \quad (3\text{-}5)$$

The τD indicates the diffusion time, ω0 is the lateral radius of the observation volume, D is the diffusion coefficient. We can use this system for the calibration in FCS setup.

Since the diffusion coefficient D is related to the radius r_h of the molecules or NPs, according to Stocks-Einstein equation, we can calculate r_h of NPs

$$D = \frac{k_B T}{6\pi\eta r H} \quad (3\text{-}6)$$

$$r_h = \frac{k_B T}{6\pi\eta D} \quad (3\text{-}7)$$

Where the k_B is the Boltzmann constant ($1.38*10^{-23}$ J/K), and T is the absolute temperature in Kelvin, η is the viscosity of the solvent. Therefore, by obtaining the diffusion coefficient and other parameters, we can calculate the hydrodynamic radius of the fluorescence NPs.

In our case, after protein corona formation, as the NPs diffused, some NPs will be stayed in the observation volume while others have moved out. If a particular type of protein corona has a high residence time, its fluorescence intensities will show stronger positive correlations over brief time intervals. Conversely, protein corona with lower residence times will show weaker correlations because their presence in the volume is more transient.

In the study of protein coronas, FCS experiments can be conducted at nanomolar concentrations of nanoparticles. under this condition, the nanoparticles move freely through a confocal volume on the order of 1 femtoliter (fL). By analyzing the fluctuations in fluorescence emission using the ACF, we can determine the diffusion time of the nanoparticles. This diffusion time will gradually increase as a protein corona forms around the nanoparticles. Utilizing the Stokes-Einstein equation, the hydrodynamic radius of the nanoparticles can be calculated. Consequently, this information allows for estimating the thickness of the protein corona enveloping the nanoparticles.

3.3 Information of proteins studied in this thesis

In the field of biomolecular research, understanding the interactions between nanoparticles and their surrounding environment is crucial. While some researchers have traditionally utilized whole blood samples to measure the protein corona, our research focuses on studying the adsorption behavior using single proteins. In our study, we have selected five representative proteins based on their varying isoelectric points and specific affinity to particular molecule. This approach allows us to delve deeper into the individual characteristics of these proteins and their interactions, providing valuable insights into their binding capabilities and behavior within a given environment.

In this section, I will introduce the physicochemical properties of these five proteins to better explain their subsequent adsorption behavior on nanoparticles modified with different surface chemistry.

3.2.1 Bovine serum albumin (BSA)

Bovine serum albumin (BSA) is a protein that is widely used in biochemical and molecular biology research. BSA is easily extracted, and its structure and molecular weight have been extensively studied, making it well suited for a variety of biological applications, such as using as protein standard in gel electrophoresis and enzyme immunoassays, and as stabilizer in various biochemical reactions. [63, 64] BSA is a single-chain polypeptide consisting of 583 amino acids with a molecular weight of approximately 66.4 kilodalton (kDa). The isoelectric point (pI) of BSA is from pH 5.1 to 5.5, which means that at this pH level, the protein carries no net electrical charge.[65]

In terms of its three-dimensional structure, BSA is a relatively compact protein with a globular structure. The molecular size of BSA can be determined by fluorescence anisotropy, which is approximately 163 nm^3.[66]

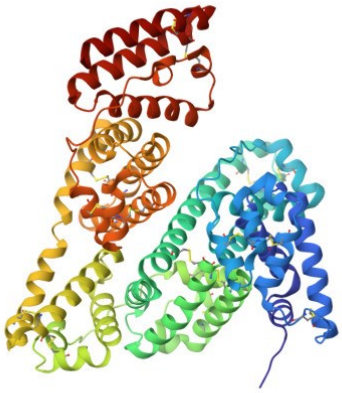

Figure 3-4. Crystal Structure of Bovine Serum Albumin (BSA). Source: Protein Data Bank.

3.2.2 Transferrin

Transferrin is a glycoprotein that binds iron in the blood and delivers it to cells that require iron for various biological processes, playing a vital role in the transport of iron in the body and maintaining the balance of iron in the body. Transferrin is a relatively large protein with a molecular weight between 76 and 81 kDa.[67, 68]

The pl of transferrin is typically between 5.6 and 6.2. This is the pH at which the protein has no net charge and is least soluble. Changes in transferrin surface charge at different pH values can affect its interactions with other molecules and its overall function.[69]

Transferrin is a bilobed protein with a unique three-dimensional structure and a large surface area that facilitates its ability to bind and transport iron. The protein consists of two symmetrical lobes, each capable of binding an iron ion. Transferrin was determined

by small-angle neutron scattering to be an oblate spheroid with a molecular volume of (144 ± 45) x 10^3 $Å^3$, approximately 144 nm^3.[70]

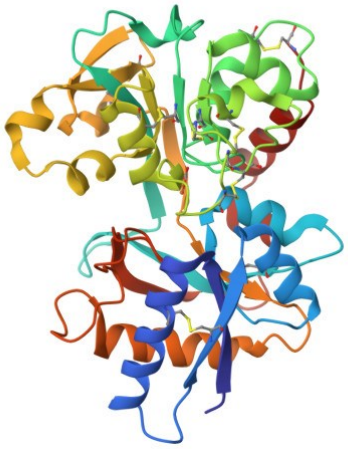

Figure 3-5. Crystal structure of Human Transferrin. Source: protein data bank.

3.2.3 Pepsin

Pepsin is an enzyme secreted in the mucosa of the stomach that plays a key role in the digestive system, breaking down proteins into smaller peptides and is one of the main proteolytic enzymes responsible for the initial digestion of dietary proteins.[71]

With a molecular weight of approximately 34 kDa and an isoelectric point (pl) of approximately 1.5 to 2.0, pepsin is an acidic protein. At this pH, pepsin has no net charge and has minimal solubility. The low isoelectric point of pepsin indicates that it is most active in the acidic environment of the stomach.[72]

Pepsin is a globular enzyme, the average pepsin dimensions under hybrid fabrication conditions amount to approximately 45×50×66 $Å^3$ calculated by molecular dynamic simulations, which is approximately 148.5 nm^3.[73] With a compact three-dimensional structure that is critical to its catalytic activity. This compact size of pepsin enables pepsin to effectively bind and cleave peptide bonds within proteins during digestion.[74]

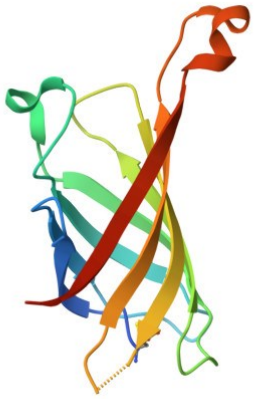

Figure 3-6. Crystal structure of pepsin. Source: protein data bank.

3.2.4 Lysozyme

Lysozyme is a bacteriolytic enzyme that is commonly found in body fluids such as tears, saliva, and mucus. It helps prevent bacterial infections by breaking down bacterial cell walls and plays a vital role in the innate immune system.[75, 76]

The pI of lysozyme is usually around 11.0 to 11.4. The high pI of lysozyme reflects its alkaline protein nature. Lysozyme's interactions with other molecules and its stability change dramatically under acidic conditions.[77]

Lysozyme is a relatively small protein with a molecular weight of approximately 14.3 kDa. The molecular size of Lysozyme can be determined by fluorescence anisotropy, which is approximately 37 nm^3.[66]

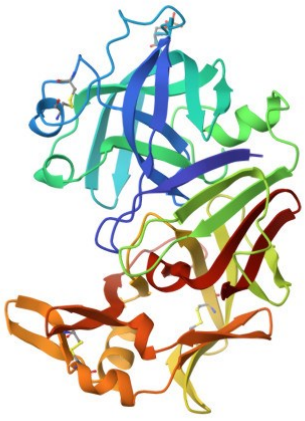

Figure3-7. Crystal structure of Lysozyme. Source: protein data bank.

3.2.5 Avidin

Avidin is a glycosylated protein known for its extremely high affinity for biotin, a vitamin essential for various metabolic processes. The binding strength between avidin and biotin is one of the strongest non-covalent interactions in nature, with a dissociation constant (Kd) of approximately 10^{-15} M. This tight binding affinity can be used in a variety of biotechnologies such as immunoassays and targeted drug delivery.[78, 79]

Avidin has a relatively high pI, ranging from 9.3 to 10.8, and therefore carries a positive charge in physiological environments.[78]

Avidin is a tetrameric protein composed of four identical subunits with a total molecular weight of approximately 65-68 kDa. The dimensions of a functional avidin tetramer are approximately 56×50×40 $Å^3$, equivalent to 112nm^3.[80]

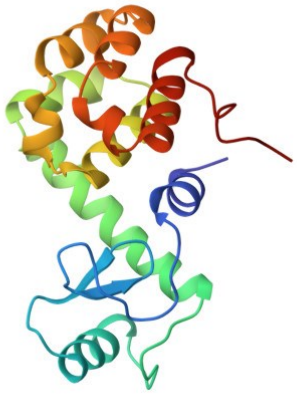

Figure 3-8. Crystal structure of Avidin. Source: protein data bank.

Proteins in living organisms are made up of only 20 amino acids, but these can be combined in countless ways to form a huge variety of proteins. The human body alone contains more than 50,000 different proteins. Studying the interaction between individual proteins and NPs is a big challenge. To address this, we selected a series of representative proteins, each with specific physical and chemical properties. This allows us to analyze the interaction between proteins with specific characteristics and NPs.

4. Chemical reagents and Instruments

4.1 Chemical reagents

List of chemicals	Purity	Company
Cadmium oxide	99 %	Sigma-Aldrich
Selenium		Sigma-Aldrich
1-octadecene	90 %	Sigma-Aldrich
Oleic acid	90 %	Sigma-Aldrich
Sulfur	99.998 %	Sigma-Aldrich
Sodium chloride	≥ 99.8 %	Sigma-Aldrich
Sodium hydroxide	≥ 99 %	Sigma-Aldrich
Myristic acid	≥ 99 %	Sigma-Aldrich
Oleylamine	≥ 98 %	Sigma-Aldrich
Tributylphosphine	97 %	Sigma-Aldrich
3-(Dimethylamino)-1-Propylamin	≥ 99 %	Sigma-Aldrich
poly (isobutylene-*alt*-maleic anhydride)	85 %	Sigma-Aldrich
Dodecylamin	≥ 98 %	Sigma-Aldrich
Chloroform	≥ 99 %	Carl Roth
Tetrahydrofuran	≥ 99 %	Carl Roth
EDC	≥ 98 %	Sigma-Aldrich
NHS	98 %	Sigma-Aldrich
BSA	≥ 96 %	Sigma-Aldrich
Transferrin	≥ 90 %	Sigma-Aldrich
Lysozyme		Roche
pepsin		Roche
Avidin		Thermo Fisher Scientific
NaCl	≥ 99.9 %	Carl Roth

KOH	≥ 85 %	Sigma-Aldrich
NaOH	≥ 99 %	Carl Roth
HCl	30 %	Sigma-Aldrich
Nitric acid	65 %	Carl Roth
Methanol	≥ 99 %	Carl Roth
MUA	95 %	Sigma-Aldrich
NH_2-PEG-SH		Rapp polymere GmbH
NH_2-PEG-biotin		Rapp polymere GmbH
Rhodamine 6G	99 %	Sigma-Aldrich

4.2 Instruments

List of instruments	**Model**	**Company**
Zetasizer	NANO ZS	Malvern Panalytical
UV-visible Spectroscopy	Agilent 8453	Agilent
Fourier-transform infrared spectroscopy	Cary 630 FTIR	Agilent
Fluorescence Spectrometer	Cary Eclipse	Agilent
Simultanthermo analysator	SDT 650	Waters
Spectral Confocal Microscopy	LSM 880	Carl-Zeiss
Transmission electron microscopy	JEM‑1400PLUS	JEOL
Rotary evaporator	Helzbad Hel-VAP	Heidolph
Drop Shape Analyzer	DSA30	Krüss
Ultracentrifuge	Optima XPN	Beckman Coulter

5. Fabrication of autofluorescent nanoparticles

5.1 Synthesis of CdSe-CdS quantum dots

CdSe-CdS core-shell quantum dots (QDs) were synthesized according to a modified synthesis protocol based on the one described by Peng et al.[81, 82] The hydrophobic QDs produced in this section can be subsequently modified on the surface to acquire various physicochemical properties.

5.1.1 Synthetic method of CdSe-CdS quantum dots

Synthesis of CdSe core QDs

Two Se-ODE precursor solutions were prepared. Se-ODE solution A (50 mM) was prepared by dissolving selenium powder (0.012 g, 0.15 mmol) in 3 mL ODE. Se-ODE solution B (100 mM) was prepared by dissolving selenium powder (0.024 g, 0.3 mmol) in 2 mL ODE and 1 mL oleic acid. CdO (0.0256 g, 0.200 mmol) and myristic acid (0.1026 g, 0.45 mmol) were added to 4 mL ODE in a 25 mL three-neck flask. The mixture was purged with nitrogen for 30 minutes and then heated to 290 °C. After a few minutes, the solution turned colorless, the temperature was reduced to 250 ℃. 1 mL of Se-ODE precursor solution A was injected swiftly into this hot solution, and it was stirred for 5 minutes. Then 0.1 mL of Se-ODE solution B was added at a speed of 0.9 mL/h to the reaction solution, and reacted for 5 minutes. This reaction cycle was continued until the CdSe cores were grown to ~ 4.2 nm. When the desired CdSe core size was reached, the heating mantle was removed to let the solution cool down rapidly. Then a mixture of chloroform, methanol and acetone (volume ratio 1:1:1) was added to the reaction solution to precipitate the CdSe QDs. After centrifugation (4000 rpm, 5 min), the supernatant containing smaller QDs was removed and 5 mL chloroform were added to disperse the QDs in the pellet. After threefold purification, CdSe core QDs were finally dispersed in ODE.

Synthesis of CdSe-CdS QDs

For the CdS shell growth process, S-ODE solution (100 mM) was firstly prepared by dispersing sulfur powder (0.016 g, 0.5 mmol) in 5 mL ODE. Then disperse CdO (0.064 g, 0.5 mmol) and myristic acid (0.251 g, 1.1 mmol) in 3.5 mL of ODE in a three-neck flask. This solution was stirring under nitrogen flow for 30 minutes and then heat up to 290 ℃ under nitrogen flow. After the solution turned colorless and transparent, the temperature was reduced to 150 ℃, and the purified CdSe core QDs which dissolved in 0.3 mL ODE was injected quickly into this solution, then the temperature was increased to 250 ℃ again. After the temperature reached 250 ℃, 0.1 mL of S-ODE solution was injected at the speed of 0.9 mL/h to the reaction solution, and reacted for 2 minutes. After that, 0.13 mL oleic acid was injected at the speed of 0.9 mL/h to the solution and reacted for 2

minutes. In the second cycle, the reaction time after both 0.1 mL S-ODE and 0.13 mL oleic acid injections was increased to 5 minutes. From the third cycle, the volume of oleic acid was decreased to 0.07 mL. This reaction cycle was continued until desired sizes of CdSe-CdS QDs were obtained. Then the heating mantle was removed to stop the reaction. After the solution had cooled down to room temperature, an equal volume of acetonitrile was added to the solution, then chloroform was added dropwise until the QDs precipitated. The QDs were completely precipitated by centrifugation at 4000 rpm for 5 minutes, then the supernatant was removed. This purification process was repeated 3 times.

Ligand exchange and shape conversion

In order to obtain spherical QDs instead of hexagonal ones, the QDs were further modified by ligand exchange and morphology transformation. A mixture of 1 mL ODE and 2 mL oleylamine were loaded into a 50 mL three-neck flask, and the mixture was heated up to 200 ℃ under nitrogen flow. Then, 0.1 mL tributylphosphine (TBP) was injected into the mixture followed by injecting purified CdSe-CdS QDs dissolved in ODE. The reaction solution was stirring at 200 ℃ for 10 minutes to achieve totally ligand exchange. Then the nitrogen flow was stopped, the solution heated directly to 220 ℃ and stirred for 5 minutes under air flow to convert the QDs from hexahedral to spherical. After shape conversion, the QDs were precipitated in a solvent mixture composed of methanol, acetone and chloroform (volume ratio=1:1:1). After centrifugation (4000 rpm, 5 minutes), the supernatant was removed. This purification procedure was repeated 3 times. The final CdSe-CdS QDs were dispersed in 5 mL chloroform, the concentration of QDs was around 100 μM.

5.1.2 UV-vis spectra of CdSe-CdS quantum dots

UltraViolet-Visible Spectroscopy (UV-vis) of CdSe-CdS core shell quantum dots was measured in chloroform, and the absorbance curve was recorded from 200 nm to 800 nm.

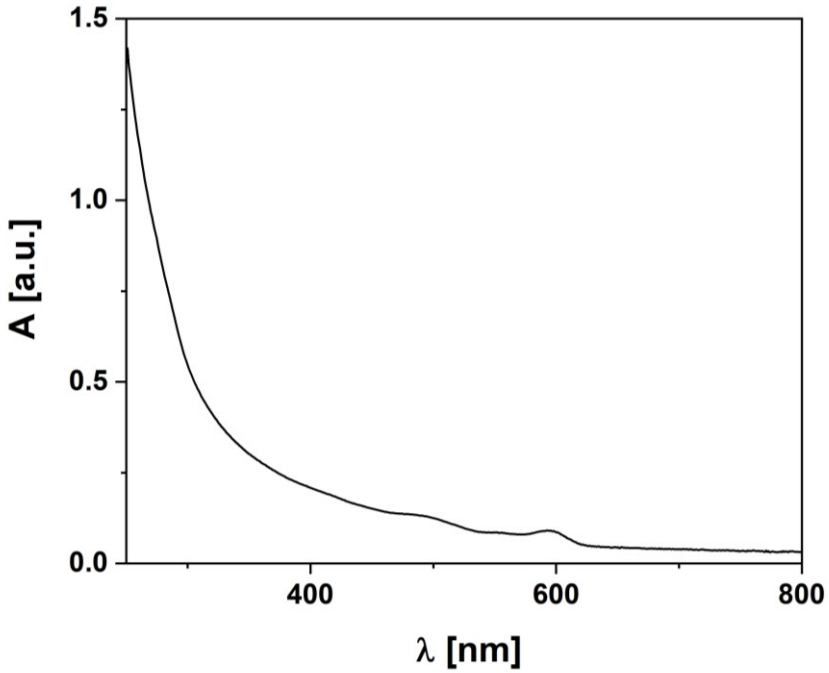

Figure 5-1. UV-vis absorbance spectrum A(λ) of CdSe-CdS QDs. CdSe-CdS QDs were dispersed in anhydrous chloroform, the first excitonic absorbance peak is at 593 nm.

From the UV-vis spectrum, the size of the as-synthesized CdSe cores was calculated as described by Peng et al [3]:

$$d(nm) = 1.6122 \times 10^{-9}\lambda^4 - 2.6575 \times 10^{-6}\lambda^3 + 1.6242 \times 10^{-3}\lambda^2 - 0.4277\lambda + 41.57 \quad (5\text{-}1)$$

In the above function, *d*(nm) is the size of nanocrystal CdSe core, and λ is the wavelength of the first excitonic absorbance peak. The resulting diameter of the CdSe cores is *d* = 4.4 nm.

5.1.3 Photoluminescence spectroscopy of CdSe-CdS quantum dots

Photoluminescence spectroscopy (PL) of CdSe-CdS core shell quantum dots was measured in chloroform, the excitation wavelength was 480 nm, and the emission range of QDs was from 600 nm to 650 nm.

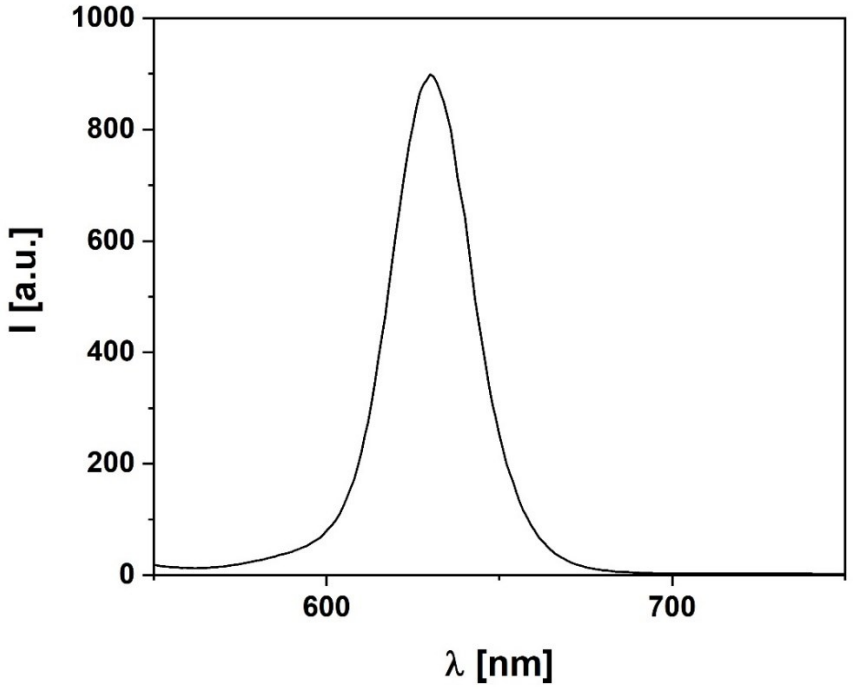

Figure 5-2. Fluorescence emission intensity I(λ) of CdSe-CdS QDs in chloroform. The excitation wavelength was 480 nm.

The CdSe-CdS QDs synthesized above exhibit narrow and symmetrical emission peaks at 620 nm, emitting orange-red light.

5.1.4 Qauntum yield calculation of CdSe-CdS QDs

To determine the quantum yield (QY) Φ of CdSe-CdS QDs, their UV-vis absorption spectra were collected and the absorbance values at λ = 480 nm were recorded for different concentrations of QDs. Then, the emission spectra of corresponding QDs were recorded with corresponding excitation at λ_{Ex} = 480 nm and the intensities were integrated from 500-700 nm and the resultant integrated intensity (I_I) was plotted with respect to the absorbance values. A similar procedure was followed for the standard dye Rhodamine 6G.[83] The gradient $\Delta I_I/A_{480}$ of each plot has been used in the following equation to calculate the QY value.[84]

$$\phi_X = \phi_{st}\left(\frac{(\Delta I_I/\Delta A_{480})_X}{(\Delta I_I/\Delta A_{480})_{st}}\right)\left(\frac{\eta_x}{\eta_{st}}\right)^2 \qquad (5\text{-}2)$$

Where ΦX is the fluorescence quantum yield of the QDs samples, Φst is the fluorescence quantum yield of the standard Rhodamine 6G in ethanol, Φst = 0.94), $(\Delta I_I)/A_{480})_x$ and $(\Delta I_I)/\Delta A_{480})_{st}$ are the gradients from the plot of integrated fluorescence intensity vs absorbance of the test samples and the standard at the same excitation wavelength of 480 nm, respectively. η_x and η_{st} are the refractive indices of the solvents of test samples ($\eta_{chloroform}$ = 1.442)[85] and the solvent of standard ($\eta_{ethanol}$ = 1.361)[86], respectively. UV-vis absorption spectra, PL spectra, and integrated intensity vs. absorbance curves of the QDs are shown below.

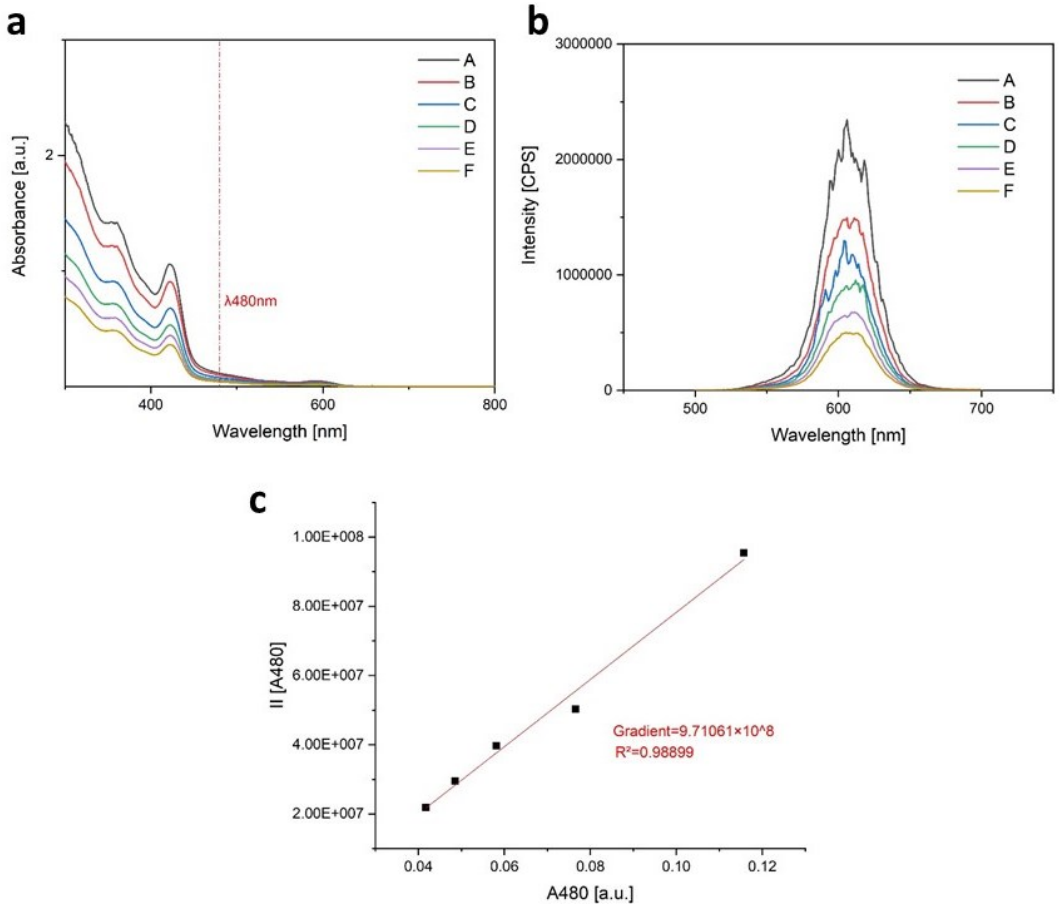

Figure 5-3. a) UV-vis adsorption and b) PL spectra of different concentrations of QDs, the excitation wavelength is the same as the wavelength of the absorbance used in the gradient plot, i.e. 480 nm). C) Linear plot of integrated PL intensity (taken in the entire wavelength range as shown in the corresponding plot) vs. absorbance A_{480} at 480 nm with different concentrations of QDs.

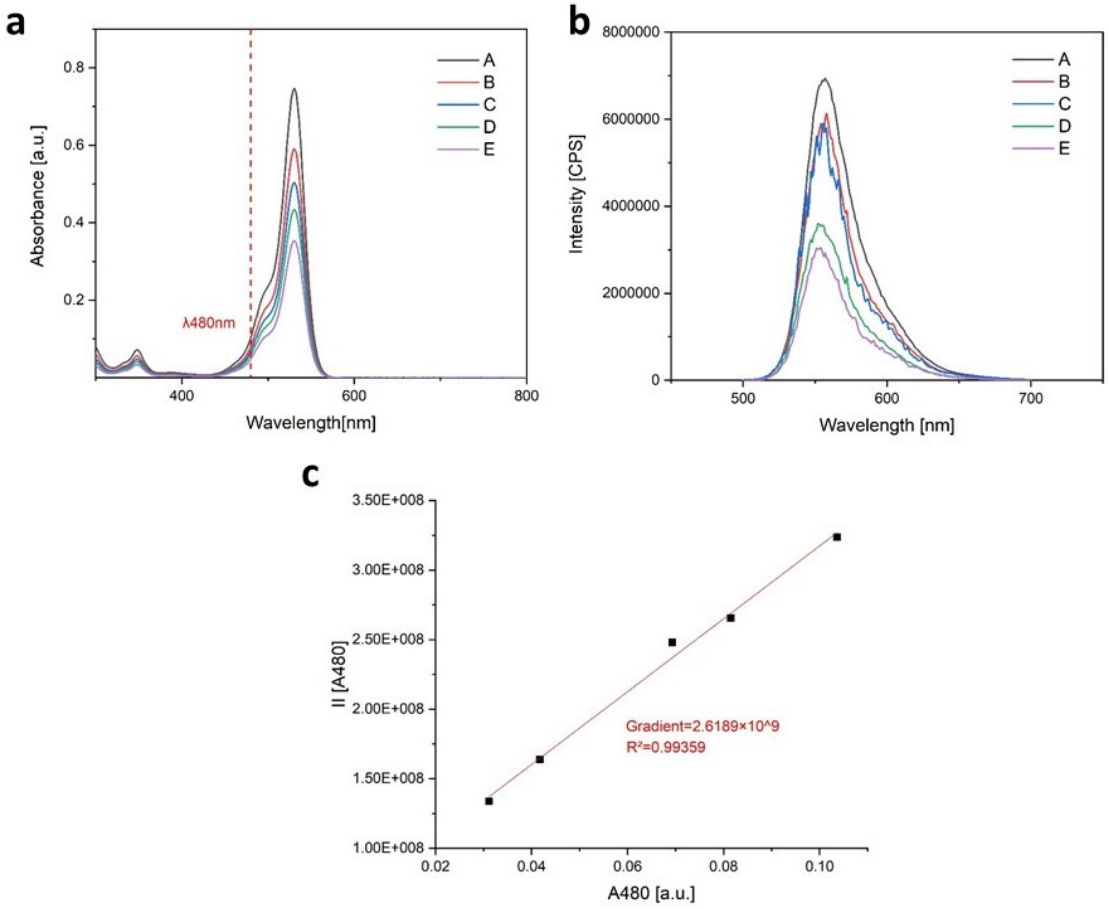

Figure 5-4. a) UV-vis adsorption and b) PL spectra of different concentrations of Rhodamine 6G, the excitation wavelength is the same as the wavelength of the absorbance used in the gradient plot, i.e. 480 nm). C) Linear plot of integrated PL intensity (taken in the entire wavelength range as shown in the corresponding plot) vs. absorbance A_{480} at 480 nm with different concentrations of Rhodamine 6G.

The quantum yield of the synthesized QDs was 39.13% compared to the standard Rhodamine 6G. This value represents that approximately 39.13% of the absorbed photons are re-emitted as luminescent photons. It is noteworthy that the quantum yield achieved here is consistent with the values previously reported for similar materials, confirming the applicability of our synthesis method.[87-89]

Our results show that the synthesized quantum dots have excellent luminescence properties. These results pave the way for further exploration of the formation of protein coronas on the surface of quantum dot nanoparticles using fluorescence correlation spectroscopy.

5.1.5 TEM images and size distribution of CdSe-CdS quantum dots

The CdSe-CdS QDs stock solution was diluted, 10 µL sample was dropped onto a 400-mesh TEM copper grid covered with carbon film. After 1 min, carefully remove the excess liquid and the TEM grid was dry completely before TEM test. The TEM image (Figure 5-3 (a)) shows spherical and evenly distributed quantum dots, this image was further analyzed by image J software to plot the histogram of QDs' diameters distribution, the mean diameter of QDs is 5.2 nm.

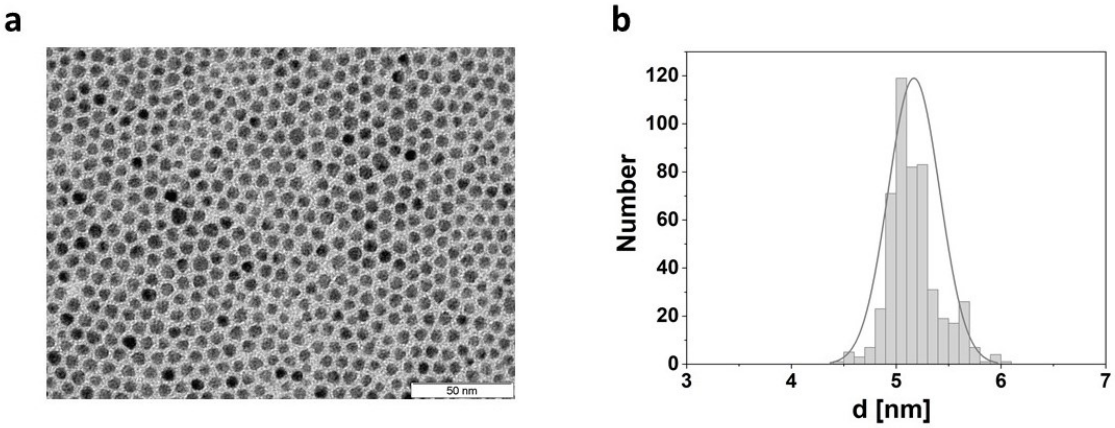

Figure 5-5. TEM image and size distribution of CdSe-CdS QDs. (a) TEM images of spherical QDs, scale bar is 50 nm. (b) Histogram of the QDs' diameters determined from the TEM image; the mean diameter is 5.2 ± 0.2 nm (N = 500 NPs).

The synthesized quantum dots have a hydrophobic surface and are dispersed in chloroform solution. They will be further surface-chemically modified for protein corona adsorption studies.

5.2 Synthesis of polymers

In order to apply hydrophobic QDs in biological research, we need to facilitate their phase transfer and dissolve them in aqueous solutions. One method to achieve this is to use amphiphilic polymers to coat the surface of the QDs. Several potential amphiphilic polymers have been developed for the polymer coating of NPs. In our study, we have chosen poly (isobutylene-alt-maleic anhydride) (PMA) as the hydrophilic backbone, as the maleic anhydride rings on the backbone can react with dodecylamine (DDA) or 3-(Dimethylamino)-1-Propylamine (DMAPA) for further functionalization, obtaining hydrophobic side chains which attach to the surface of QDs. The unreacted anhydride rings can form negatively charged carboxyl groups when the NPs are dispersed in aqueous solutions, thereby maintaining stability through electrostatic repulsion in the solution.

5.2.1 Synthetic method of polymaleimide based polymer

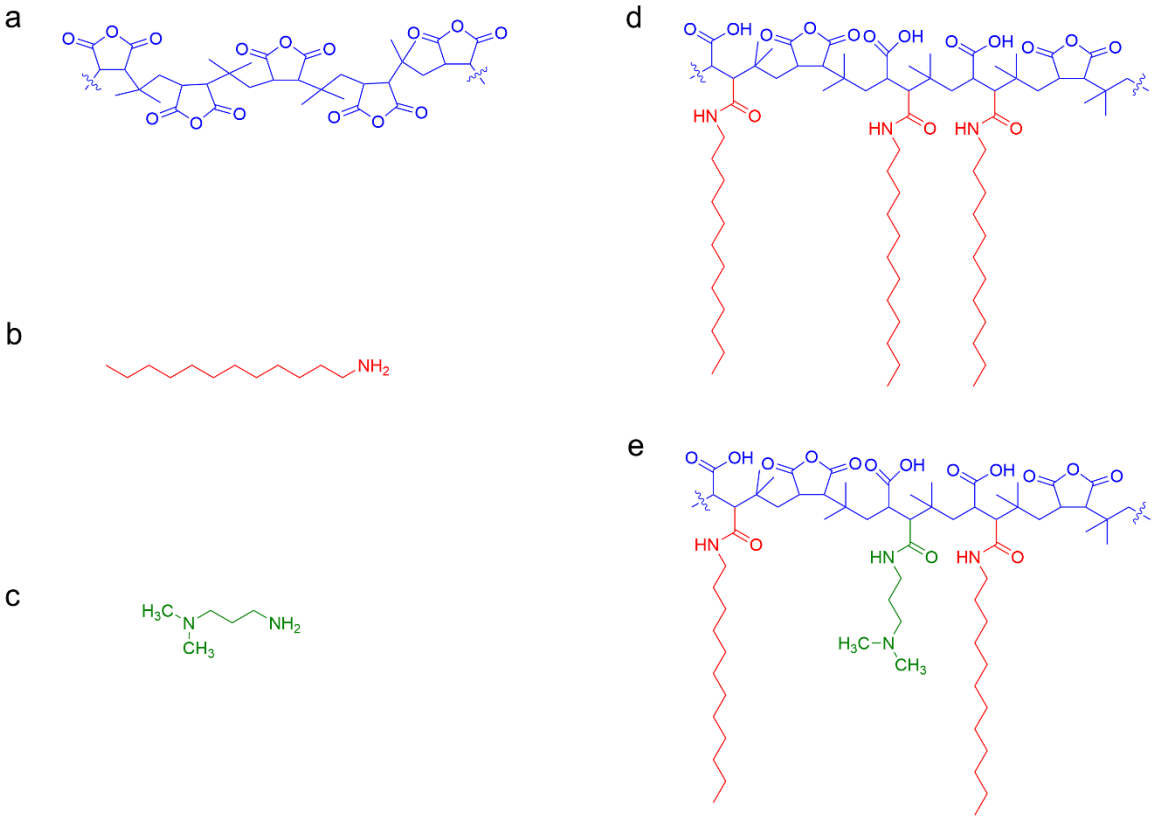

Figure 5-6. Chemical structure of a) poly (isobutylene-alt-maleic anhydride), b) Dodecylamin, c) 3-Diethylamino-1-propylamine, d) PMA-$DDA_{0.75}$-$DMAPA_0$, and e) PMA-DDA-DMAPA.

Table 5-1. List of chemical amounts use to synthesis polymer with different DMAPA ratio

Polymer	PMA (monomer concentration)	DDA	DMAPA
PMA-$DDA_{0.75}$	3.084 g (20 mmol)	2.780 g (15 mmol)	0
PMA-$DDA_{0.5}$-$DMAPA_{0.25}$	3.084 g (20 mmol)	1.854 g (10 mmol)	0.511 g (5 mmol)
PMA-$DDA_{0.5}$-$DMAPA_{0.5}$	3.084 g (20 mmol)	1.854 g (10 mmol)	1.022 g (10 mmol)
PMA-$DDA_{0.25}$-$DMAPA_{0.75}$	3.084 g (20 mmol)	0.927 g (5 mmol)	1.533 g (15 mmol)

Synthesis of PMA-$DDA_{0.75}$-$DMAPA_0$

The synthesis of PMA-$DDA_{0.75}$-$DMAPA_0$ was based on previous work. 3.1 g (0.5 mmol) PMA were prepared in a round-neck flask and 2.70 g (15 mmol) DDA were dissolved in 100 mL anhydrous THF. The DDA solution was added to the PMA under stirring, then the mixture was heated to 55-60 ℃. The mixture was turbid in the first 30 minutes and turned transparent gradually afterwards. After that, the mixture was concentrated to 30-40 mL under reduced pressure by rotary evaporation. The remaining 30-40 mL of the mixture were heated to 60 ℃ again and stirred under reflux overnight. Then the solution was completely evaporated under reduced pressure at 40 ℃. The dried polymer powder was then dissolved in 40 mL anhydrous chloroform, yielding a polymer solution with a monomer concentration of 0.5 M. The structure of chemicals is showed in Figure 5-6.

Synthesis of PMA-$DDA_{0.5}$-$DMAPA_{0.25}$, PMA-$DDA_{0.5}$-$DMAPA_{0.5}$ and PMA-$DDA_{0.25}$-$DMAPA_{0.75}$

The synthesis of PMA-$DDA_{0.5}$-$DMAPA_{0.25}$, PMA-$DDA_{0.5}$-$DMAPA_{0.5}$ and PMA-$DDA_{0.25}$-$DMAPA_{0.75}$ followed the same protocol as for PMA-$DDA_{0.75}$-$DMAPA_0$, with variations of the molar ratio of DDA and DMAPA introduced (see in Table 5-1). 3.1 g PMA (0.5 mmol) were dissolved in 50 mL of THF, then DMAPA were added to the turbid mixture under stirring. The mixture was sonicated for 3-5 minutes and DDA were added. Then, the solution was heated to 60 ℃ and stirred under reflux overnight. The next day, THF was completely removed by rotary evaporation. The polymer formed a uniform film that was dissolved in 40 mL anhydrous chloroform. The nominal final monomer concentration of polymer is 0.5 M. The structure of chemicals is showed in Figure 5-6.

5.2.2 Fourier Transform Infrared Spectroscopy (FTIR) analysis

The fourier transform infrared spectroscopy (FTIR) was measured by Agilent cary 630 FTIR spectrometer, all the samples are test for powder.

The results from the FTIR cannot be used for quantitative analysis of the polymer components. However, the characteristic peaks of polymaleamide are evident in the spectra of all polymers, indicating that the polymers share a similar hydrophilic backbone.

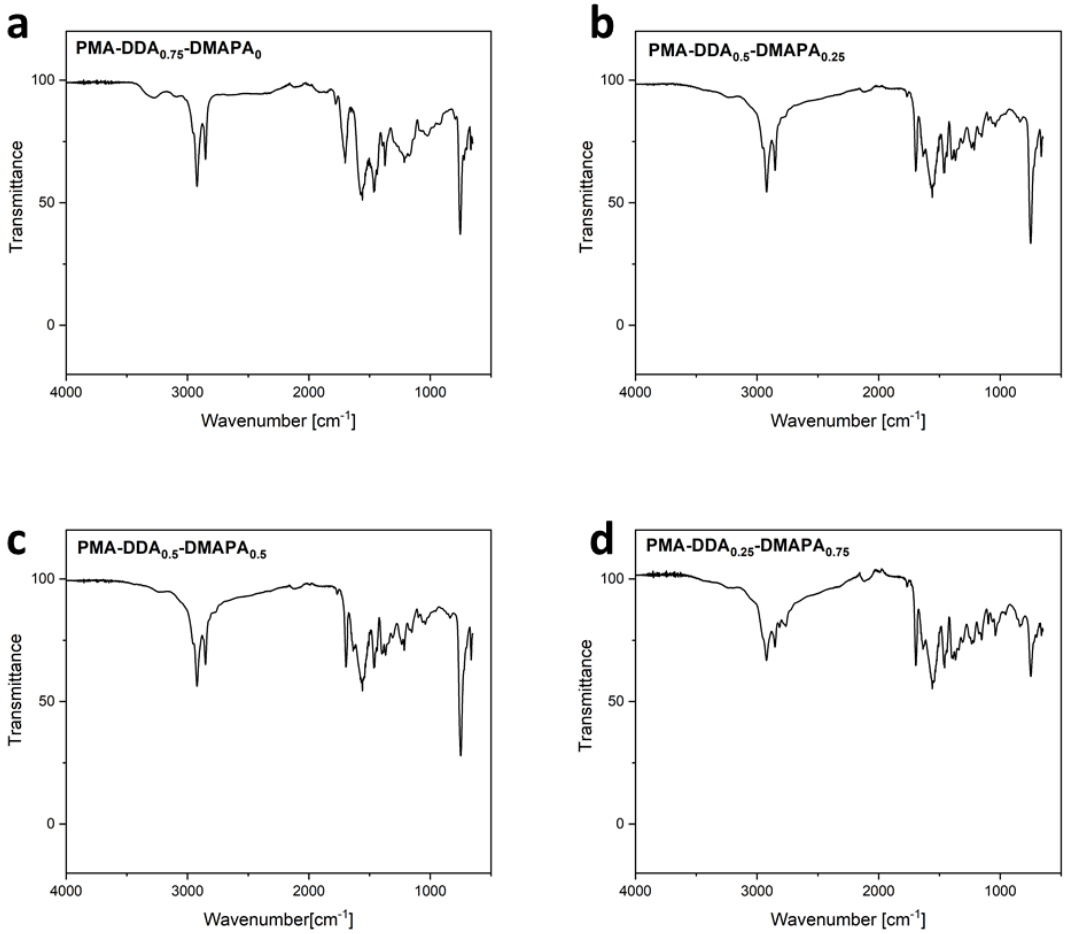

Figure 5-7. FITR of a) PMA-DDA$_{0.75}$-DMAPA$_0$, b) PMA-DDA$_{0.5}$-DMAPA$_{0.25}$, c) PMA-DDA$_{0.5}$-DMAPA$_{0.5}$, and d) PMA-DDA$_{0.25}$-DMAPA$_{0.75}$.

5.2.3 Thermogravimetric analysis (TGA)

The thermogravimetric analysis was conducted by simultanthermo analysator, the samples were tested as powder, and for each polymer, the measurements were repeated for 3 times.

While the thermogravimetric data cannot provide a quantitative analysis of the polymer proportions, the consistent temperature at which the weight of each polymer decreases indicates that all polymers exhibit similar thermal decomposition temperatures.

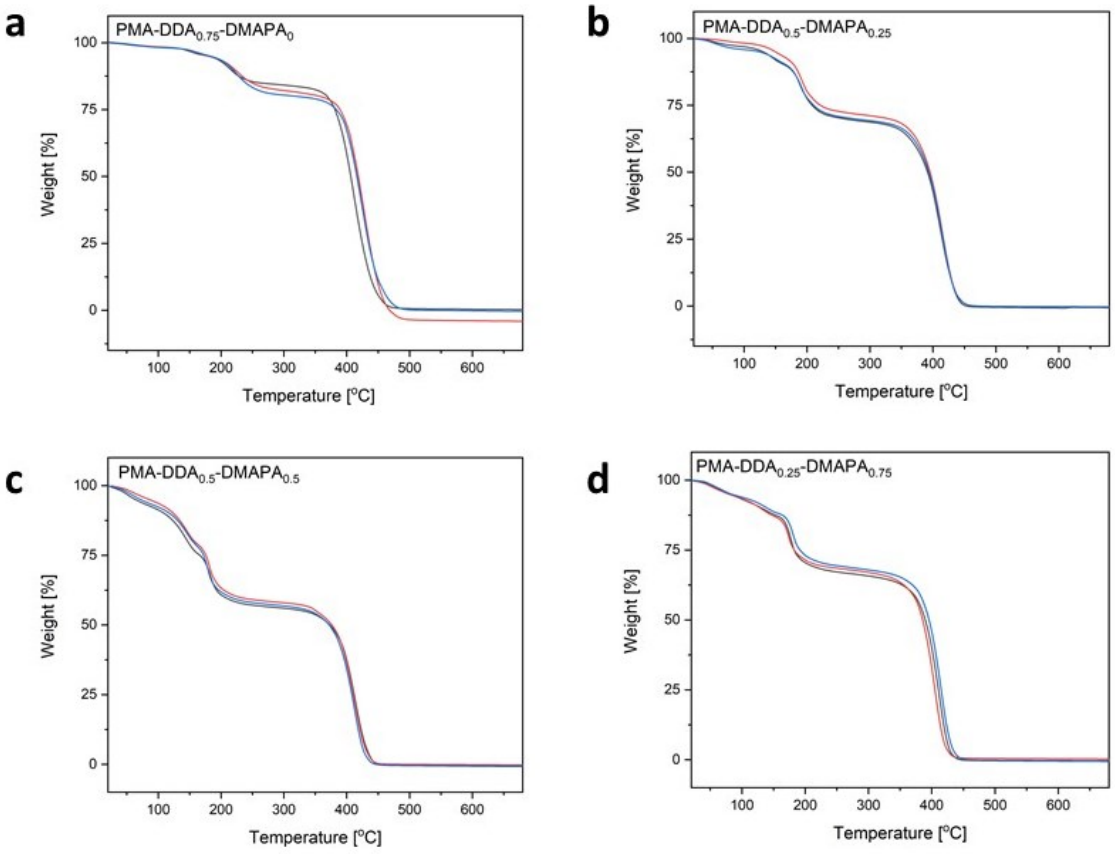

Figure 5-8. TGA of a) PMA-$DDA_{0.75}$-$DMAPA_0$, b) PMA-$DDA_{0.5}$-$DMAPA_{0.25}$, c) PMA-$DDA_{0.5}$-$DMAPA_{0.5}$, and d) PMA-$DDA_{0.25}$-$DMAPA_{0.75}$.

5.3 Fabrication of polymer coated CdSe-CdS quantum dots

This section describes the fabrication of nanoparticles overcoated with the synthesized polymer. These polymers have an amphiphilic structure, featuring a hydrophilic side (carboxylic group, secondary amine group, or PEG) and a hydrophobic side (alkane). The hydrophobic quantum dots strongly interact with the self-assembled alkane monolayer on their surface, while the hydrophilic nature of the polymers facilitates the efficient transfer of nanoparticles from an organic solvent to an aqueous phase.

Hydrophobic quantum dots are generally insoluble in aqueous environments, limiting their use in biological systems. Coating them with amphiphilic polymers facilitates their dispersion in water or other polar solvents, thereby improving solubility and stability, making the coated quantum dots suitable for biological applications such as imaging, drug delivery, and biosensing. The surface of polymer-coated nanoparticles can also provide

functional groups for further binding to biomolecules, thereby achieving targeted delivery or specific interactions with biological targets.

Coated quantum dots are used in fluorescence imaging technology due to their superior optical properties, including high brightness and photostability, and they can be used for in vivo imaging to track biological processes. Phase-transferred quantum dots can also serve as carriers for drug delivery, allowing real-time monitoring of drug distribution in vivo and achieving controlled drug release. Surface-functionalized quantum dots can be used as components in biosensors to help improve the sensitivity and selectivity of detection of various biomolecules.

5.3.1 Polymer coating process

The phase transfer of CdSe-CdS QDs (polymer coating process) was done according to previous work with some modifications. CdSe-CdS QDs stock solution was mixed with PMA-DDA$_{0.75}$-DMAPA$_0$, PMA-DDA$_{0.5}$-DMAPA$_{0.25}$, PMA-DDA$_{0.5}$-DMAPA$_{0.5}$ or PMA-DDA$_{0.25}$-DMAPA$_{0.75}$ stock solution in chloroform. The volume of polymer was calculated according to the equations below. First, we need to calculate the effective surface area A_{eff} of QDs use equation (5-3).

$$A_{eff} = 4\pi \times \left(\frac{d_{eff}}{2}\right)^2 \tag{5-3}$$

Then we can calculate the number of monomer units that needs to be added. The parameter $R_{p/Area}$ is the amount of polymer added per effective NP surface, we chose 100 nm^{-2} refer to previous research.

$$N_p = R_{p/Area} \times A_{eff} \tag{5-4}$$

$$V_p = \frac{R_{p/Area} \times A_{eff} \times c_{NP} \times V_{NP}}{c_p} \tag{5-5}$$

In these equations above, the V_p is the volume of polymer we need to add in coating process, and c_{NP} is the concentration of QDs, V_{NP} is the volume of QDs solution we add, c_p is the concentration of polymer solution.

The mixture was sonicated for 30 seconds to mix it thoroughly, then the chloroform was evaporated in a rotary evaporator at 40 °C. Upon removal of the solvent, the polymer wraps around the QDs and forms a thin film on the inner walls of the flask. Anhydrous chloroform was added to the flask to re-dissolve the polymer coated QDs. The mixture was sonicated again for 30 seconds, and the chloroform removed by rotary evaporation afterwards. These steps were carried out 3 times to obtain a homogeneous polymer coating on the QDs. Finally, the NPs were dispersed in aqueous solution. The maleic acid

anhydrides in the PMA backbone are readily hydrolyzed in water thus generating carboxylic acid groups that improve the solubility of the NPs in water. PMA-$DDA_{0.75}$-$DMAPA_0$ coated NPs were dissolved in alkaline sodium hydroxide buffer (10 mM, pH 12) to deprotonate the carboxylic acid groups for additional electrostatic stabilization. In contrast, PMA-$DDA_{0.5}$-$DMAPA_{0.25}$, PMA-$DDA_{0.5}$-$DMAPA_{0.5}$ and PMA-$DDA_{0.25}$-$DMAPA_{0.75}$ coated NPs were dispersed in acidic solution (0.1 M NaCl at pH 3.3, adjusted by HCl) and stirred for 4 hours to protonate the amino groups that were introduced via DMAPA. All the NPs were further purified by ultracentrifugation (40000 rpm, 30 minutes) after the polymer coating process to remove excess polymer in the supernatant.

5.3.2 pH dependent zeta potential of nanoparticles

Understanding the surface chemistry and charge properties of nanoparticles is essential to predict their stability, dispersion, and interactions in biological and environmental systems. One of the key parameters to evaluate is the zeta potential, which represents the electrostatic potential of the sliding plane of dispersed particles and provides

in an increase in the overall positive charge of the polymer, while at higher pH values, deprotonation will happen, resulting in a predominantly negative surface charge. insight into the stability of colloidal systems. In this experiment, we investigated the pH-dependent zeta potential of nanoparticles coated with amphiphilic polymers.

As pH changes, the protonation and deprotonation of carboxyl and dimethylamino groups in the polymers synthesized above will directly affect the surface charge of the nanoparticles. Specifically, at lower pH values, the dimethylamino groups on the polymers can be protonated, resulting

By systematically varying the pH and measuring and analyzing the changes in zeta potential over a range of pH values, this experiment aims to elucidate how the surface charge of nanoparticles coated with amphiphilic polymers responds to changes in the ionic environment, thereby affecting the formation of their surface protein corona. This understanding is essential for the rational design of nanomaterials for specific applications in a variety of scientific and industrial fields.

The nanoparticles were diffused in 1×PBS buffer under different pH value, the zeta potential was measured by Malvern zetasizer.

After encapsulation of the QDs with PMA-$DDA_{0.75}$-$DMAPA_0$, the carboxyl groups on their surface become deprotonated, resulting in a significant negative charge that remains relatively consistent across the pH range of 5 to 9. This suggests that the polymer surface modification promotes a uniform distribution of negative charge on the QDs, which enhances the stability of the nanoparticles in solution due to the increased surface charge density.

Following the introduction of DMAPA into the polymer, its protonation under acidic conditions resulted in the nanoparticles carrying both positive and negative charges, rendering QDs@PMA-DDA$_{0.5}$-DMAPA$_{0.25}$ electrically neutral in solutions at pH 5 and pH 6. However, as the pH increased, the protonation ability of DMAPA diminished, leading to a slight negative charge on the surface of the NPs (-12.7 mV).

As the proportion of DMAPA in the polymer increased, the positive charge on the surface of the NPs increased accordingly. Both QDs@PMA-DDA$_{0.5}$-DMAPA$_{0.5}$ and QDs@PMA-DDA$_{0.25}$-DMAPA$_{0.75}$ exhibit positive charges within the pH range of 5 to 9, however, this positive charge weakens under alkaline conditions at pH 8 and pH 9.

In summary, the zeta potential of QDs@PMA-DDA$_{0.75}$-DMAPA$_0$ remains largely unaffected by changes in solution pH and exhibits a strong negative charge. In contrast, QDs@PMA-DDA$_{0.5}$-DMAPA$_{0.25}$ is essentially electrically neutral. The positive surface charge of QDs@PMA-DDA$_{0.5}$-DMAPA$_{0.5}$ and QDs@PMA-DDA$_{0.25}$-DMAPA$_{0.75}$ decreases as the pH increases. Understanding the surface charges of these NPs provides valuable insights for future research on the formation of protein corona.

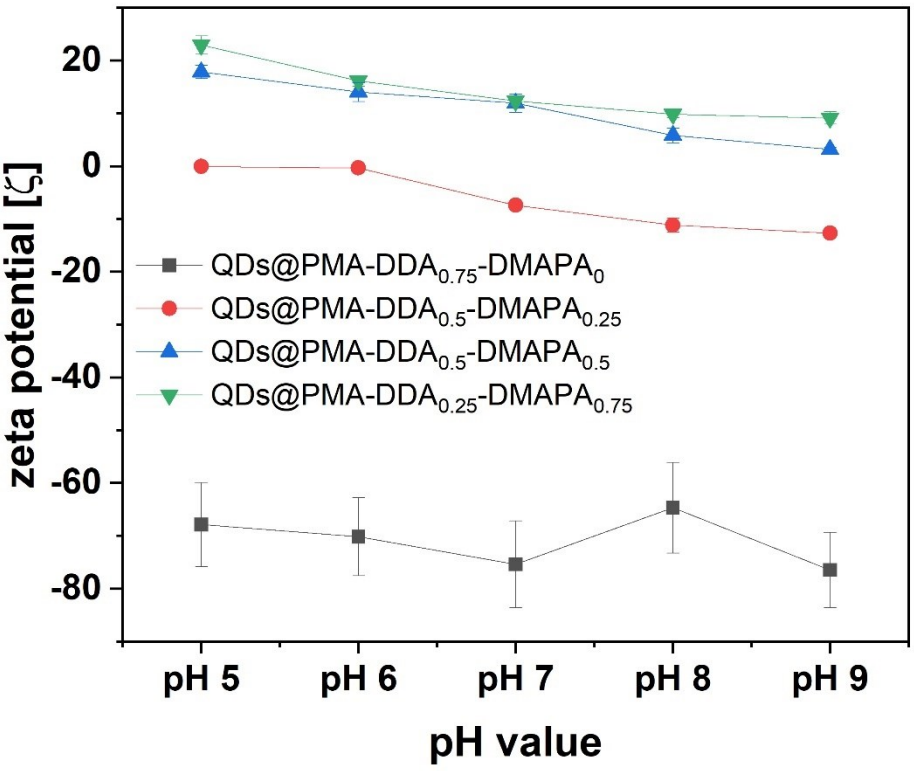

Figure 5-9. pH dependent zeta potential of QDs@PMA-$DDA_{0.75}$-$DMAPA_0$, QDs@PMA-$DDA_{0.5}$-$DMAPA_{0.25}$, QDs@PMA-$DDA_{0.5}$-$DMAPA_{0.5}$, and QDs@PMA-$DDA_{0.25}$-$DMAPA_{0.75}$.

Table 5-2. pH dependent zeta potential (ζ) of QDs@PMA-$DDA_{0.75}$-$DMAPA_0$, QDs@PMA-$DDA_{0.5}$-$DMAPA_{0.25}$, QDs@PMA-$DDA_{0.5}$-$DMAPA_{0.5}$, and QDs@PMA-$DDA_{0.25}$-$DMAPA_{0.75}$.

Zeta potential (ζ, mV)	pH 5	pH 6	pH 7	pH 8	pH 9
QDs@PMA-$DDA_{0.75}$-$DMAPA_0$	-67.9 ± 8.0	-70.2 ± 7.4	-75.4 ± 8.2	-64.7 ± 8.6	-76.5 ± 7.1
QDs@PMA-$DDA_{0.5}$-$DMAPA_{0.25}$	-0.1 ± 0.1	-0.4 ± 0.1	-7.4 ± 0.8	-11.2 ± 1.3	-12.7 ± 0.8
QDs@PMA-$DDA_{0.5}$-$DMAPA_{0.5}$	17.8 ± 1.2	14.0 ± 1.8	11.9 ± 1.7	5.8 ± 1.4	3.1 ± 0.3
QDs@PMA-$DDA_{0.25}$-$DMAPA_{0.75}$	22.9 ± 1.7	16.1 ± 1.0	12.3 ± 0.8	9.8 ± 0.6	9.1 ± 1.2

5.3.3 pH dependent hydrodynamic size of nanoparticles

The hydrodynamic size of a NPs, defined as the effective diameter of the particle as it moves through a fluid, is a key parameter that reflects its stability and behavior in solution. Our measurement technique, dynamic light scattering (DLS), is used to assess the hydrodynamic size of NPs under different pH conditions. As the pH increases or decreases, the ionization state of the surface groups leads to changes in the net charge of the NPs, which affects their colloidal stability and aggregation tendency. In the case of a high net surface charge, the repulsive forces between particles increase and the tendency to aggregate decreases, while in the case of a decreased net surface charge, the repulsive forces between particles decrease and the likelihood of aggregation increases, resulting in larger nanoparticles.

Understanding the relationship between pH and hydrodynamic size is critical to optimizing NPs design for specific applications, ensuring stable properties are maintained under physiological conditions or in the target environment.

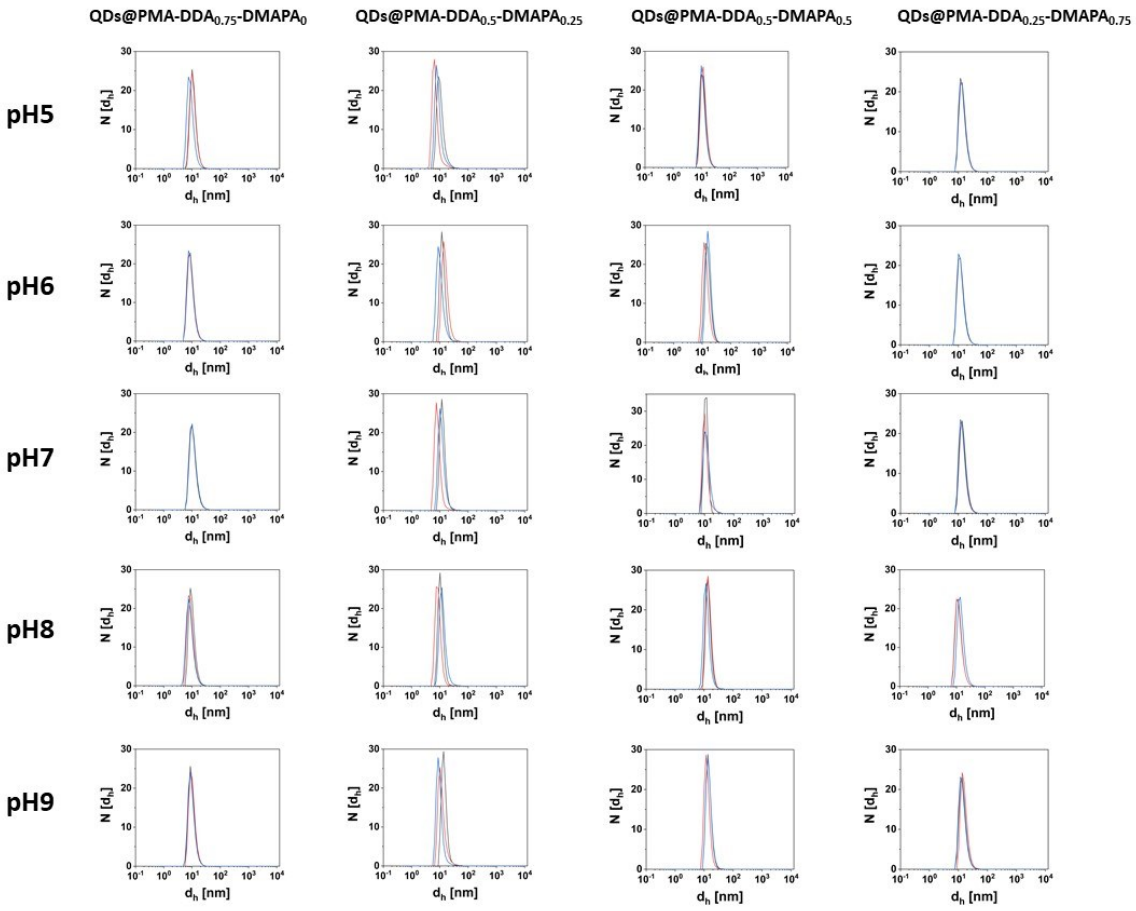

Figure 5-10. pH dependent hydrodynamic size of QDs@PMA-DDA$_{0.75}$-DMAPA$_0$, QDs@PMA-DDA$_{0.5}$-DMAPA$_{0.25}$, QDs@PMA-DDA$_{0.5}$-DMAPA$_{0.5}$, QDs@PMA-DDA$_{0.25}$-DMAPA$_{0.75}$.

Table 5-3. Hydrodynamic diameters of QD-polymer conjugates in PBS buffer from pH 5 to pH 9, the results are presented as number weighted distributions, and measurements were recorded in triplicates.

pH [1× PBS]	QDs@PMA-DDA$_{0.75}$-DMAPA$_0$ [nm]	QDs@PMA-DDA$_{0.5}$-DMAPA$_{0.25}$ [nm]	QDs@PMA-DDA$_{0.5}$-DMAPA$_{0.5}$ [nm]	QDs@PMA-DDA$_{0.25}$-DMAPA$_{0.75}$ [nm]
5	10.5 ± 1.2	9.0 ± 1.8	13.5 ± 1.0	14.4 ± 0.3
6	9.3 ± 0.2	13.0 ± 2.7	15.5 ± 1.8	12.5 ± 0.2
7	11.4 ± 0.2	11.0 ± 2.2	11.5 ± 0.5	14.5 ± 0.5

8	9.3 ± 0.7	10.9 ± 2.1	13.8 ± 1.2	13.2 ± 1.2
9	10.1 ± 0.3	12.2 ± 2.4	14.2 ± 1.1	15.0 ± 1.0

Based on the results presented in Figure 5-x and Table 5-X, the particle sizes of the four NPs exhibit minimal variation among pH 5 to pH 9, indicating that the NPs are quite stable within this pH range. Notably, QDs@PMA-DDA$_{0.5}$-DMAPA$_{0.5}$ and QDs@PMA-DDA$_{0.25}$-DMAPA$_{0.75}$ display slightly larger particle sizes. This increase may be attributed to their lower surface electrostatic charge, which compromises their stability in solution compared to QDs@PMA-DDA$_{0.75}$-DMAPA$_{0}$. In contrast, QDs@PMA-DDA$_{0.5}$-DMAPA$_{0.25}$ has a smaller particle size than the two previously mentioned nanoparticles. Despite its surface being nearly neutral, its strong hydrophilicity contributes to its stability in aqueous solution, as it carries both positive and negative charges on its surface.

This result also demonstrated that the NPs above exhibited excellent colloidal stability within the pH range of 5 to 9, thereby establishing a solid foundation for future research on protein corona formation under varying pH conditions.

5.3.4 NaCl concentration dependent hydrodynamic size of nanoparticles

The ionic strength of the solution plays an important role in regulating the electrostatic interactions between nanoparticles and their surroundings, thus affecting their hydrodynamic size.

When sodium chloride is introduced into the nanoparticle suspension, the ions can shield the surface charges on the nanoparticles. As the sodium chloride concentration increases, this shielding effect leads to a decrease in the electrostatic repulsion between the charged nanoparticles, which may lead to increased aggregation. At higher sodium chloride concentrations, the nanoparticles may aggregate together, resulting in a larger hydrodynamic size measured by dynamic light scattering (DLS). In contrast, at lower sodium chloride concentrations, the electrostatic repulsion between the nanoparticles is stronger, which favors their stability and leads to a smaller measured size.

After dispersing the nanoparticles in sodium chloride solutions of different concentrations and measuring their hydrodynamic size after 0 and 24 hours, we can analyze and compare the stability of nanoparticles encapsulated by different polymers in sodium chloride solutions and preliminarily infer their stability in physiological environments.

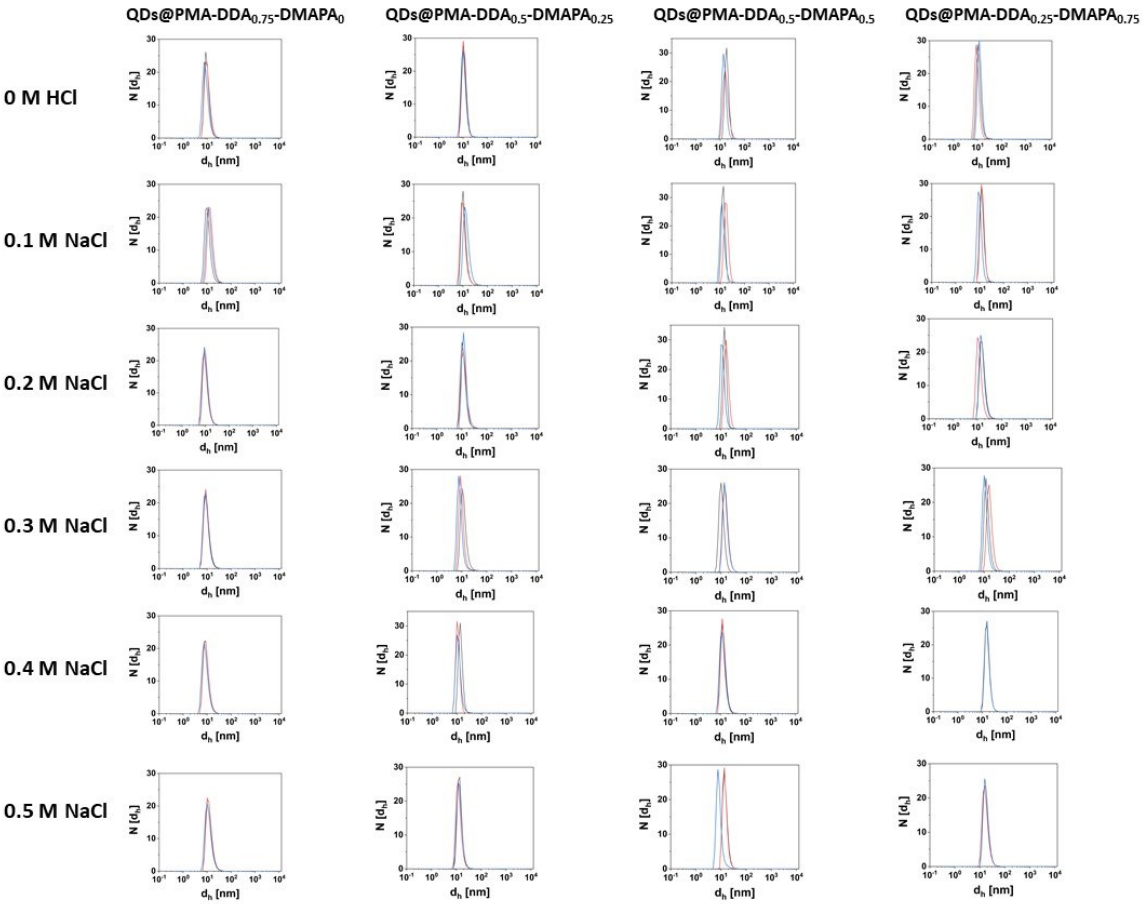

Figure 5-11. Hydrodynamic diameter of NPs in 0-0.5 M NaCl solution. The results are presented as number weighted distributions and measurements were recorded in triplicates.

Table 5-4. Hydrodynamic diameter of NPs in 0-0.5 M NaCl solution. Measurement of each NPs were conducted for 3 times.

NaCl concentration [M]	PMA-$DDA_{0.75}$-$DMAPA_0$ [nm]	PMA-$DDA_{0.5}$-$DMAPA_{0.25}$ [nm]	PMA-$DDA_{0.5}$-$DMAPA_{0.5}$ [nm]	PMA-$DDA_{0.25}$-$DMAPA_{0.75}$ [nm]
0	9.8 ± 0.5	10.9 ± 0.3	17.0 ± 2.1	11.1 ± 1.4
0.1	12.6 ± 1.7	12.0 ± 1.9	14.7 ± 2.8	11.9 ± 1.6
0.2	9.9 ± 0.4	12.6 ± 0.7	14.2 ± 2.6	14.8 ± 2.4
0.3	9.7 ± 0.3	10.2 ± 1.8	13.9 ±2.7	13.7 ± 3.0

0.4	9.1 ± 0.4	12.2 ± 1.6	13.0 ± 0.5	16.3 ± 0.1
0.5	12.3 ± 0.5	13.5 ± 0.7	13.0 ± 3.5	17.5 ± 0.6

5.3.5 Interfacial tension of nanoparticles

The chemical modification of the QDs surface plays a critical in determining the wettability of NPs surfaces. When NPs are functionalized with hydrophilic groups, they exhibit a greater affinity for the aqueous phase, which can lead to increased interfacial tension (IFT) with organic solvents. Conversely, hydrophobic modifications result in reduced IFT. A NP's hydrophilicity is a key factor influencing its interactions with biomolecules and ultimately with cells. Studies have shown that hydrophobic NPs are more prone to adsorb biomolecules, potentially triggering immune responses in vivo, while hydrophilic NPs demonstrate lower protein adsorption, contributing to a prolonged circulation time in the bloodstream.

Thus, a thorough understanding of the physicochemical properties of NPs is essential for predicting their behavior at the nano-bio interface. In this study, we evaluated the IFT of the nanoparticle system described in this thesis.

The IFT measurements of QDs-polymer conjugates were recorded by the drop shape analyzer. We used the pendant drop method for the measurement, where we produced 30 µL drop of each nanoparticle solution in a transparent glass cup filled with toluene. The shape of the drop depends on the relationship between the interfacial tension and gravity. In this method, the interfacial tension can be calculated from the projection of the hanging drop recording by a high frame rate camera implemented with the drop shape analyzer. The QDs-polymer NPs were loaded into a syringe which was then equipped with a stainless-steel needle (diameter: 1.28 mm) to produce a 30 µL drop of NP dispersion (for QDs@PMA-$DDA_{0.25}$-$DMAPA_{0.75}$ was 15 µL) in toluene. The photographs of the pendant drop were recorded for 10 hours. The IFT was calculated using the principal radius of curvature of the drop, and further calculated according to Young-Laplace fitting as shown in the following function.[90]

$$\Upsilon = \frac{\Delta\rho g d_e}{H} \qquad (5\text{-}6)$$

$\Delta\rho$ represents the difference in density between the liquid drop and the surrounding medium (toluene). The term g denotes the acceleration due to gravity. The symbol d_e indicates the largest horizontal diameter of the drop. Additionally, H is a function of the ratio S_n (which is defined as d_n/d_e), where dn refers to the horizontal diameter measured at a point located at a distance of de multiplied by (n/10) from the bottom of the drop.

The captured drop profile for each NPs was further fitted by the equation below.[91]

$$\Upsilon_t = \Upsilon_m + \frac{\Upsilon_0 + \Upsilon_m}{1 + \left(\frac{t}{t_h}\right)^n} \qquad (5\text{-}7)$$

Here, Y_t represents the interfacial tension at any given time t, while Y_0 denotes the interfacial tension of the pure solvent (water-toluene) as shown in Figure 5-X. The term Y_m indicates the interfacial tension at meso-equilibrium, n is a dimensionless exponent, which is a constant related to the hydrophobicity of the nanoparticles, usually higher n indicates stronger hydrophobicity. And t_h refers to the half-life required to achieve the meso-equilibrium state.

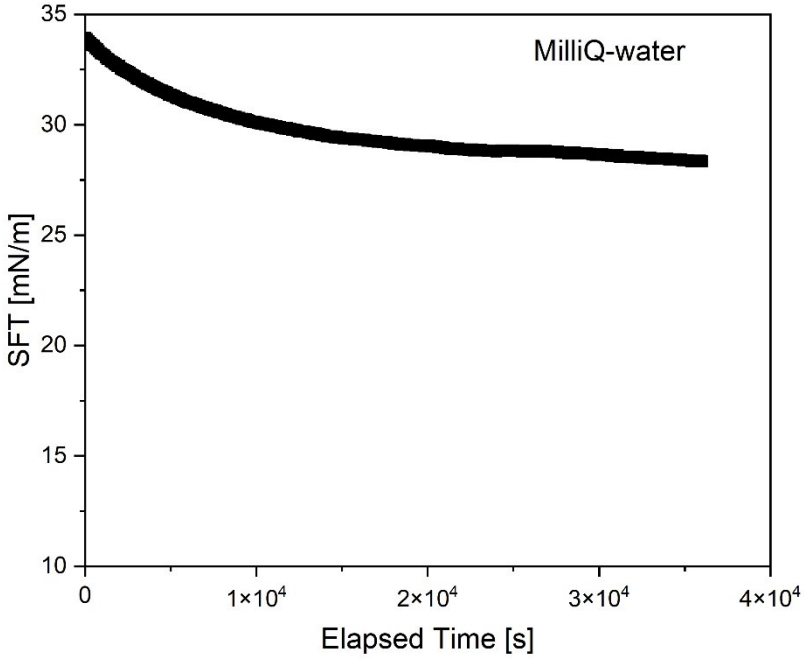

Figure 5-12. Interfacial tension of MilliQ water-toluene. The mean surface tension is 29.71 ± 1.35 mN/m.

Through the above fitting analysis, we can preliminarily evaluate the differences in hydrophobicity and hydrophilicity between the studied nanoparticles. Further, we can explore a more comprehensive understanding of the behavior of NPs by calculating the maximum decay rate of the IFT (v_{max}).

$$v_{max} = \frac{n\,(\Upsilon_0 - \Upsilon_m)}{4\,t_h} \qquad (5\text{-}8)$$

By examining the dynamic changes in surface tension of NPs in toluene over time, we can gain deeper insights into their properties and elucidate the subsequent protein corona adsorption experiments.

The changes recording in IFT and the fitting for each NPs sample in toluene are illustrated in Figure 5-X and Table 5-X. The results demonstrate that the behavior of IFT for NPs dispersed in aqueous solution significantly depends on the polymer composition.

We can evaluate the hydrophilicity of the NPs using the fitted parameters. Specifically, a higher value of γ_m indicates greater hydrophilicity, while n represents the degree of hydrophobicity; thus, a higher value of n corresponds to stronger hydrophobicity. However, evaluating the hydrophilicity of the NPs based solely on these two values is inadequate. A comprehensive analysis requires consideration of additional fitting parameters to fully characterize the properties of the nanoparticles.

Droplets of QDs@PMA-$DDA_{0.75}$-$DMAPA_0$ NPs were stable in toluene for 10 hours. During this observation period, their IFT gradually decreased from 30 mN/m in the beginning, reaching a final value of 22.5 mN/m. This slow change suggests that the initial repulsive force stemming from the strong negative charge on the NP surface hindered rapid adsorption at the interface, highlighting their significant hydrophilicity. However, the gradual decrease in interfacial tension over the 10 hours indicates that, despite the hydrophilic nature of the NPs, their ability to effectively reduce the interfacial tension at the water-toluene interface is limited. This limitation can be attributed to the strong electrostatic repulsion between the negatively charged NPs and the water-toluene interface, which restricts their ability to migrate and stabilize quickly at the interface.

After introducing DMAPA into the polymer, QDs@PMA-$DDA_{0.5}$-$DMAPA_{0.25}$ and QDs@PMA-$DDA_{0.5}$-$DMAPA_{0.5}$ exhibited similar γm values of 10.71 and 10.68, respectively, indicating that their hydrophilicity is significantly lower than that of QDs@PMA-$DDA_{0.75}$-$DMAPA_0$. Among them, QDs@PMA-$DDA_{0.5}$-$DMAPA_{0.5}$ demonstrated stronger hydrophobicity and a slower IFT decay rate. Although the electrostatic charge of QDs@PMA-$DDA_{0.5}$-$DMAPA_{0.25}$ is lower than that of QDs@PMA-$DDA_{0.5}$-$DMAPA_{0.5}$, the zwitterionic nature of this NPs facilitated the formation of a hydration layer around the NPs, thereby enhancing their hydrophilic properties.

When we introduced QDs@PMA-$DDA_{0.25}$-$DMAPA_{0.75}$ into toluene, the NPs could not remain stable in the solvent, and the droplets quickly fell apart. This instability can be attributed to the increased positive charge of the NPs, which results in poor compatibility with the solvent and inadequate stability. Additionally, the uneven distribution of positive charges on the NPs surface further diminishes droplet stability, causing them to rapidly settle in the solution.

DMAPA is a hydrophobic amine that can increase the overall hydrophobicity of the polymer structure. While DMAPA contains amine functional groups capable of forming

hydrogen bonds with water, the aliphatic chains of DMAPA create a more hydrophobic environment when incorporated into NPs. This effect can mask their hydrophilicity, leading to a net decrease in hydrophilic properties. Although amines can be protonated in aqueous solutions to generate positive charges, an excessive amount of DMAPA may result in a predominance of positive surface charges, also encourages the formation of hydrophobic domains within the NPs structure, reducing the interaction of the NPs with water molecules and lowering their affinity for water.

The IFT results indicate that the introduction of DMAPA groups decreases both the stability and hydrophilicity of NPs at the water-organic interface. Notably, irrespective of the surface charge, an increase in the proportion of DMAPA correlates with a decline in stability and an enhancement of hydrophobicity.

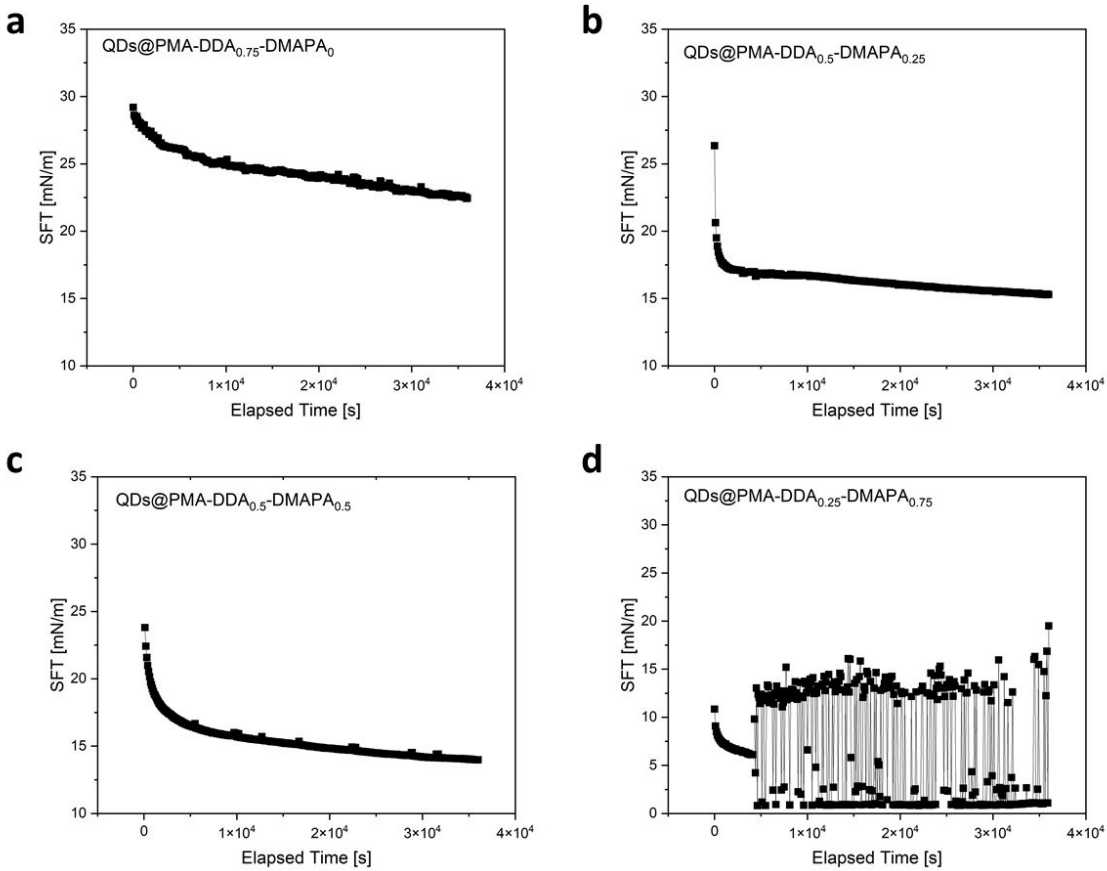

Figure 5-13. Interfacial tension (IFT) of a) QDs@PMA-$DDA_{0.75}$-$DMAPA_0$, b) QDs@PMA-$DDA_{0.5}$-$DMAPA_{0.25}$, c) QDs@PMA-$DDA_{0.5}$-$DMAPA_{0.5}$, d) QDs@PMA-$DDA_{0.25}$-$DMAPA_{0.75}$, the IFT was recorded for 10 hours. The red line represents the fitting by Hua and Rosen equation.

Table 5-5. Dynamic analysis of interfacial tension. Where γm is the meso-equilibrium interfacial tension, th is the half-life time to reach this value, n is a constant related to the

hydrophobicity, $vmax$ is the decay rate of the interfacial tension, and γmean is the mean surface tension during measurements.

NPs	Y_m [mN/m]	t_h [s]	n	v_{max} [mN/ms]
QDs@PMA-$DDA_{0.75}$-$DMAPA_0$	---	---	---	---
QDs@PMA-$DDA_{0.5}$-$DMAPA_{0.25}$	10.71 ± 0.52	50.88 ± 15.30	0.16 ± 0.009	0.015
QDs@PMA-$DDA_{0.5}$-$DMAPA_{0.5}$	10.68 ± 0.15	523.15 ± 18.47	0.36 ± 0.007	0.003
QDs@PMA-$DDA_{0.25}$-$DMAPA_{0.75}$	---	---	---	---

5.4 Biotinylating and PEGylating of polymer coated CdSe-CdS quantum dots

In the field of nanoscience, biotinylation is a powerful tool that facilitates the functionalization of nanoparticles and nanomaterials with biotin or Polyethylene glycol (PEG).

Biotin is a water-soluble B vitamin that plays a vital role in various metabolic processes, including the metabolism of fats, carbohydrates, and proteins. It acts as a coenzyme for several carboxylases and is important for fatty acid synthesis and gluconeogenesis.

Using the strong binding interaction between biotin and avidin (or streptavidin), biotinylated nanoparticles can be used in biosensors for the detection of biomolecules. For example, a surface coated with avidin can capture biotinylated DNA or proteins, allowing for sensitive detection in a variety of diagnostic applications. By conjugating biotin to drug-loaded nanoparticles, researchers can target cells with high levels of avidin or streptavidin receptors, which can significantly improve the efficacy of treatments and minimize the side effects of damage to healthy tissues. Biotinylated nanoparticles can also be used for imaging studies (e.g., fluorescence microscopy or MRI) by combining them with imaging agents.[92, 93]

Polyethylene glycol (PEG) is a biocompatible hydrophilic polymer of varying molecular weights. PEG enhances the properties and performance of biomolecules and nanomaterials. Its applications in drug delivery, imaging, and immunotherapy illustrate its importance in advancing biomedical research and developing innovative therapeutic strategies.

The large size of the PEG chain sterically hinders access of other biomolecules (such as serum proteins or immune cells) to the PEGylated surface, thereby reducing opsonization (the process of marking particles for clearance). PEGylation also increases the hydrophilicity of NPs, improving their solubility in biological fluids and minimizing the aggregation behavior of nanoparticles. By modifying the surface with PGE, the recognition and clearance of nanoparticles by the immune system can be reduced, thereby extending the circulation time of nanodrugs in the blood.[94, 95]

In this thesis, biotinylating or pegylating was introduced into the surface of QDs NPs by chemical modification. In subsequent experiments, the formation of protein corona was measured by incubation with different proteins. We were able to study the formation behavior of protein corona on the surface of biotinylated or PEGylated NPs.

5.4.1 Biotinylating of polymer coated CdSe-CdS quantum dots

The surface biotinylation was performed on QDs coated with polymers. Two specific NPs were selected for the experiment: QDs@PMA-$DDA_{0.75}$-$DMAPA_0$ and QDs@PMA-$DDA_{0.5}$-$DMAPA_{0.25}$. The biotinylation process utilized the EDC/NHS coupling method (Figure 5-15) to enable the reaction between NH_2-PEG_{5000}-biotin and the carboxyl groups present on the polymer surface.

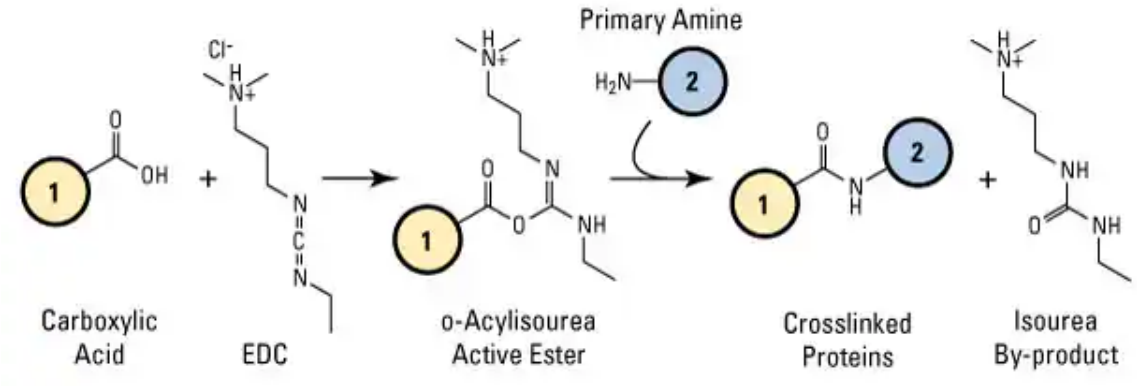

Figure 5-14. Mechanism of EDC/NHS coupling. Thermo Fisher website.

50 µL 0.02 M (EDC/NHS) fresh water solution was mixed to 1 mL of 50 µM QDs@PMA-$DDA_{0.75}$-$DMAPA_0$ or QDs@PMA-$DDA_{0.5}$-$DMAPA_{0.5}$, stirring at room temperature for 30 minutes. After 30 minutes, use ultrafiltration tube to remove unreacted EDC and NHS in the mixture solution (3500 rpm, 5 mins). The solution was re-dissolved in PBS buffer (pH 7), and add 1 mL 0.2 µM NH_2-PEG_{5000}-biotin to the mixture solution, reacted for 4 hours at room temperature. After 4 hours, use ultrafiltration tube to remove unreacted NH_2-PEG_{5000}-biotin.

5.4.2 PEGylating of polymer coated CdSe-CdS quantum dots

Synthesis of PMA-DDA$_{0.5}$-PEG$_{0.25}$

The synthesis of PMA-DDA$_{0.5}$-PEG$_{0.25}$ followed the same protocol as the polymers above, with introduction of PMA (3.084 g, 20 mmol) were dissolved in 50 mL of THF, then α-Methoxy-ω-Amino PEG (10 g, 5 mmol) were added to the turbid mixture under stirring. The mixture was sonicated for 3-5 minutes and DDA were added. Then, the solution was heated to 60 ℃ and stirred under reflux overnight. The next day, THF was completely removed by rotary evaporation. The polymer formed a uniform film that was dissolved in 40 mL anhydrous chloroform. The nominal final monomer concentration of polymer is 0.5 M. The structure of chemicals is showed in Figure 5-7, and it is named PMA-DDA$_{0.75}$-PEG$_{0.25}$.

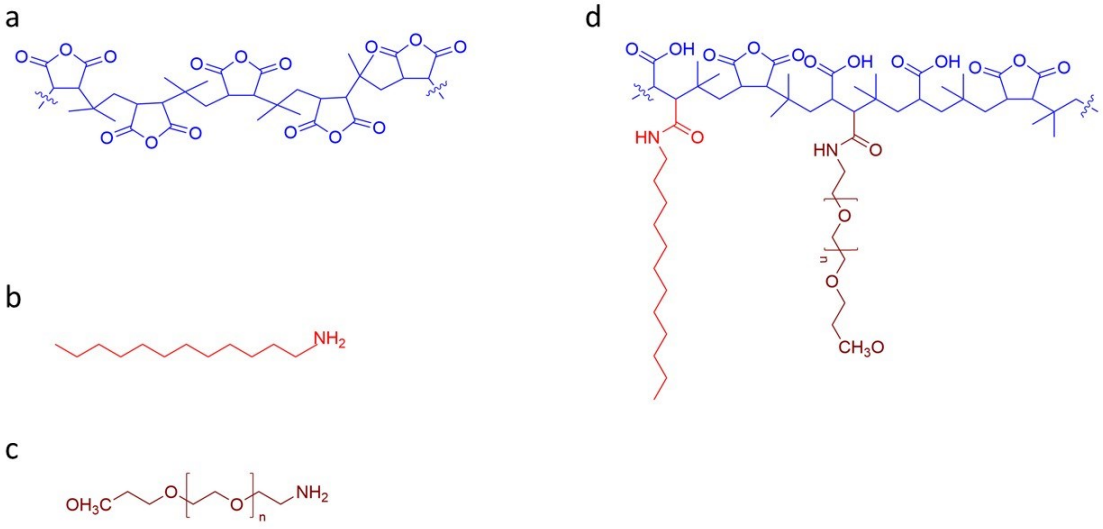

Figure 5-15. Chemical structure of a) poly (isobutylene-alt-maleic anhydride), b) Dodecylamin, c) α-Methoxy-ω-Amino PEG, and d) PMA-DDA$_{0.75}$-PEG$_{0.25}$.

Table 5-6. List of chemical amounts use to synthesis polymer grafted with PEG.

Polymer	PMA (monomer concentration)	DDA	CH_3O-PEG-NH_2
PMA-DDA$_{0.75}$-PEG$_{0.25}$	3.084 g (20 mmol)	2.780 g (15 mmol)	10 g (5 mmol)

The process of pegylating on QDs was same as polymer coating process above. The mixture of PMA-$DDA_{0.75}$-$PEG_{0.25}$ stock solution was sonicated for 30 seconds to mix it thoroughly, then the chloroform was evaporated in a rotary evaporator at 40 °C. Upon removal of the solvent, the polymer wraps around the QDs and forms a thin film on the inner walls of the flask. Anhydrous chloroform was added to the flask to re-dissolve the polymer coated QDs. The mixture was sonicated again for 30 seconds, and the chloroform removed by rotary evaporation afterwards. These steps were carried out 3 times to obtain a homogeneous polymer coating on the QDs. Finally, the NPs were dispersed in in alkaline sodium hydroxide buffer (10 mM, pH 12) to deprotonate the carboxylic acid groups for additional electrostatic stabilization. The NPs were further purified by ultracentrifugation (40000 rpm, 30 minutes) after the polymer coating process to remove excess polymer in the supernatant, and named as QDs@PMA-$DDA_{0.75}$-$PEG_{0.25}$.

5.4.3 pH dependent zeta potential of nanoparticles

The nanoparticles were diffused in 1×PBS buffer under different pH value, the zeta potential was measured by Malvern zetasizer.

After grafting PEG-biotin onto the surface of QDs@PMA-$DDA_{0.75}$-$DMAPA_0$ NPs, a significant increase in the NPs' zeta potential was observed in Figure 5-X, reaching -13.7 mV at pH 5, which is approximately 50 mV higher than before. This enhancement may result from the reaction between the amino groups on NH_2-PEG-biotin and the negatively charged carboxyl groups on the NPs surface, leading to partial neutralization of the negative charge and a decrease in the surface static charge. Moreover, the PEG portion of PEG-biotin contributes to increased hydrophilicity of the NPs. Although PEG itself is nearly neutral, its steric hindrance and hydrophilicity can still influence the interaction between ions in the solution and the NPs surface. This effect may stabilize the particles, potentially leading to increased electrostatic repulsion and may lead to a more uniform distribution of charges, thus impacting the zeta potential readings.

For the biotinylating on the surface on QDs@PMA-$DDA_{0.5}$-$DMAPA_{0.25}$-biotin, we also observed slightly zeta potential increase, but much lower than we see on the surface of QDs@PMA-$DDA_{0.75}$-$DMAPA_0$. This is likely because PMA-$DDA_{0.5}$-$DMAPA_{0.25}$ is a zwitterionic polymer that contains both positively and negatively charged groups within its structure, allowing it to maintain a neutral overall charge in solution. When biotin is grafted onto these polymers, the net charge contribution is less pronounced compared to nanoparticles (NPs) with predominantly anionic surfaces. As a result, while biotinylation does lead to some increase in zeta potential, the impact may be limited due to the zwitterionic nature of the polymer, which mitigates the overall charge change. Additionally, zwitterionic polymers can foster a more favorable hydration layer around the particles, providing stability and potentially reducing electrostatic repulsion. Consequently, this may lead to a smaller increase in zeta potential upon biotinylation in comparison to other NP systems.

Lastly, we have studied the zeta potential change of pegylated NPs under different pH conditions. Unlike the first two NPs, we directly grafted PEG onto the polymer before coating it onto the QDs to achieve phase transfer. PEG is a neutral polymer, and its grafting onto a polymer containing carboxyl groups increases the mass and surface area without significantly altering the overall surface charge after coating the nanoparticles. As a result, the inherent negative charge from the carboxyl groups continues to dominate as we see in Figure 5-16 and Table 5-7.

The zeta potential of these three NPs shows minimal variation with pH. Understanding the surface charges will enhance our ability to further study the protein corona formation.

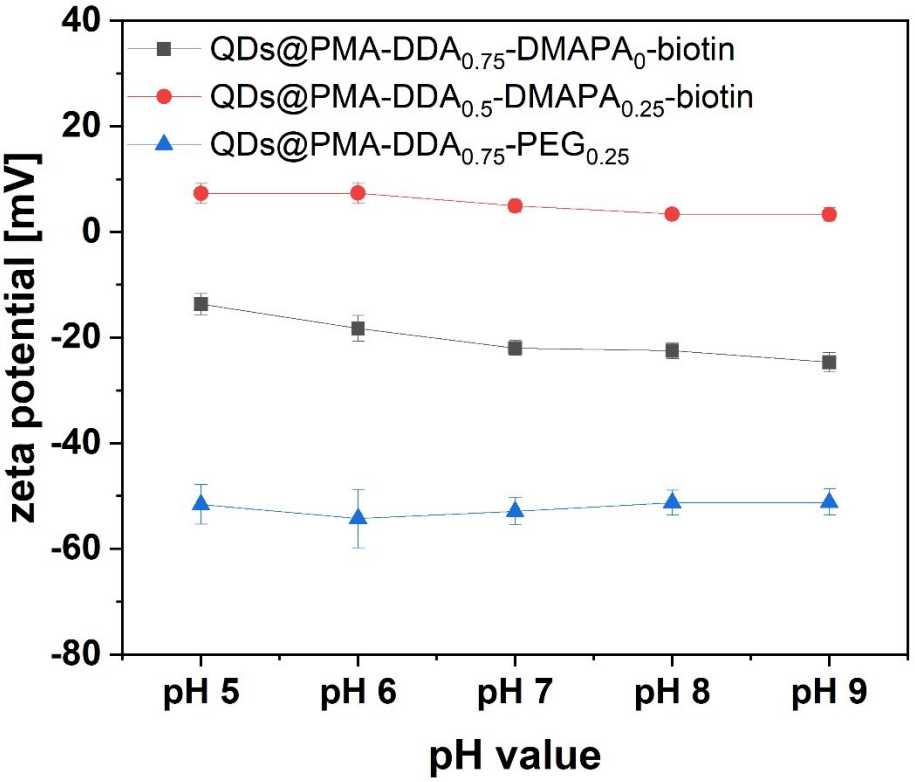

Figure 5-16. pH dependent zeta potential (ζ) of QDs@PMA-DDA$_{0.75}$-DMAPA$_0$-biotin, QDs@PMA-DDA$_{0.5}$-DMAP$_{0.25}$-biotin and QDs@PMA-DDA$_{0.75}$-PEG$_{0.25}$.

Table 5-7. pH dependent zeta potential (ζ) of QDs@PMA-DDA$_{0.75}$-DMAPA$_0$-biotin, QDs@PMA-DDA$_{0.5}$-DMAP$_{0.25}$-biotin and QDs@PMA-DDA$_{0.75}$-PEG$_{0.25}$.

Zeta potential (ζ, mV)	pH 5	pH 6	pH 7	pH 8	pH 9

QDs@PMA-DDA$_{0.75}$-PEG-biotin	-13.7 ± 2.0	-18.3 ±2.4	-22.0 ± 1.4	-22.5 ± 1.5	-24.7 ± 1.8
QDs@PMA-DDA$_{0.5}$-DMAPA$_{0.25}$-PEG-biotin	7.3 ± 1.9	7.3 ± 2.0	4.9 ± 1.2	3.4 ± 0.7	3.3 ± 1.3
QDs@PMA-DDA$_{0.75}$-PEG$_{0.25}$	-51.6 ± 3.8	-54.3 ± 5.6	-52.9 ± 2.6	-51.3 ± 2.4	-51.2 ± 2.5

5.4.4 pH dependent hydrodynamic size of nanoparticles

The hydrodynamic size of NPs was recorded under different pH conditions by zeta sizer, size distribution is shown in Figure 5-17.

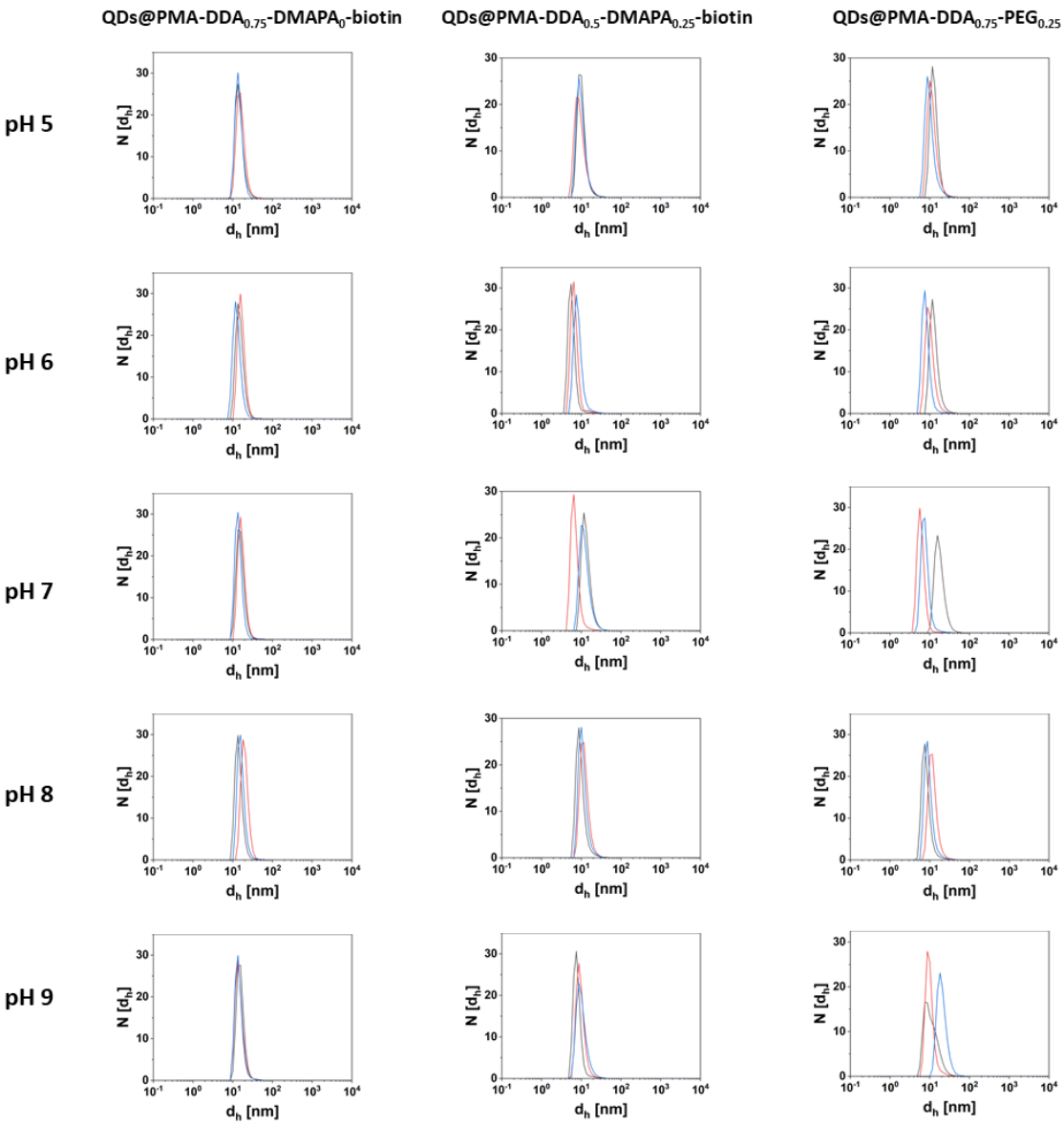

Figure 5-17. pH dependent hydrodynamic size of QDs@PMA-DDA$_{0.75}$-DMAPA$_0$-biotin, QDs@PMA-DDA$_{0.5}$-DMAPA$_{0.25}$-biotin and QDs@PMA-DDA$_{0.75}$-PEG$_{0.25}$.

The results indicate that these three NPs exhibit good colloidal stability, with particle size remaining relatively constant across different pH conditions. This stability provides a strong foundation for our subsequent investigations into protein corona formation under varying pH environments.

5.4.5 NaCl concentration dependent hydrodynamic size of nanoparticles

The hydrodynamic size of NPs was recorded under different NaCl concentration by zeta sizer, size distribution is shown in Figure 5-18.

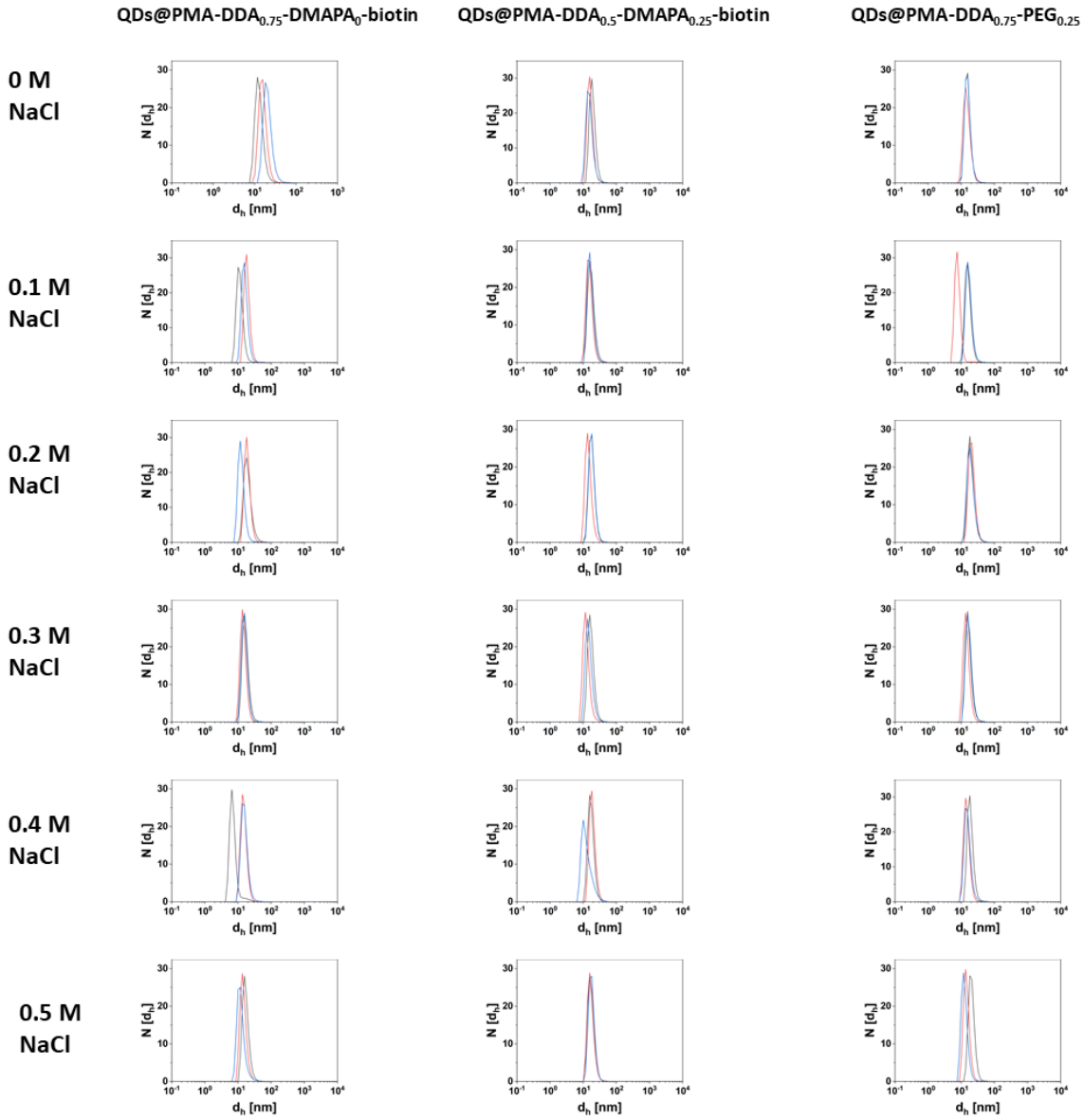

Figure 5-18. Hydrodynamic diameter of NPs in 0-0.5 M NaCl solution. The results are presented as number weighted distributions and measurements were recorded in triplicates.

The results indicate that these three nanoparticles exhibit good colloidal stability, with particle size remaining relatively constant across different NaCl concentrations. This stability provides a strong foundation for our subsequent investigations into protein corona formation in PBS buffer.

5.4.6 Interfacial tension of nanoparticles

The IFT measurements of QDs-polymer conjugates were recorded by the drop shape analyzer. We used the pendant drop method for the measurement, where we produced 30 µL drop of each NPs solution in a transparent glass cup filled with toluene. The shape of the drop depends on the relationship between the interfacial tension and gravity. In this method, the IFT can be calculated from the projection of the hanging drop recording by a high frame rate camera implemented with the drop shape analyzer. The QDs-polymer NPs were loaded into a syringe which was then equipped with a stainless-steel needle (diameter: 1.28 mm) to produce a 30 µL drop of NPs solution. The photographs of the pendant drop were recorded for 10 hours. The IFT was calculated using the principal radius of curvature of the drop, and further calculated according to Young-Laplace fitting as shown in Figure 5-19. and the change of IFT was further fitted by Hua and Rosen equation, the parameters are shown in Table 5-8.

After grafting PEG-biotin onto the surface, the interfacial tension of QDs@PMA-$DDA_{0.75}$-$DMAPA_0$-biotin significantly decreased compared to QDs@PMA-$DDA_{0.75}$-$DMAPA_0$, with a calculated γ_m of 10.54 mN/m and n of 1.33, suggesting an increase in hydrophobicity. While the incorporation of PEG-biotin would theoretically enhance the hydrophilicity of the NPs, the observed IFT results contradict this expectation. This discrepancy may arise from the substantial reduction in the surface charge of the NPs following PEG-biotin modification, which could lead to insufficient electrostatic repulsion, thereby decreasing stability. Although PEG's long chains and flexible structure provide steric hindrance that contributes to NPs stabilization, the reduction in surface negative charge may also alter the adsorption equilibrium between the aqueous and organic phases.

The QDs@PMA-$DDA_{0.5}$-$DMAPA_{0.25}$-biotin NPs droplets were unable to maintain stability in the toluene solution. After approximately 30 mins, the suspended droplet began to fall down. This instability may be attributed to the introduction of PEG-biotin, which increased the positive surface charge of the zwitterionic polymer-coated NPs. While zwitterionic polymers typically provide colloidal stability, the addition of PEG-biotin alters both the surface charge and hydrophilicity of the NPs. This change decreases the NPs' compatibility with toluene, promoting the formation of aggregates and resulting in their rapid sedimentation. The attachment of PEG-biotin may also facilitate interactions between NPs, leading to flocculation or aggregation. If the biotin groups encourage proximity between adjacent NPs, they could effectively overcome the expected steric repulsion from the zwitterionic layer, thereby accelerating NPs aggregation and settling at the bottom of the solution.

The IFT of QDs@PMA-$DDA_{0.75}$-$PEG_{0.25}$ has a sharp downward trend and quickly reaches equilibrium. The final interfacial tension is about 10 mN/m. After PEG-CH_3O is grafted into the polymer, the surface charge of the NPs also reduced, but the presence of PEG can increase the hydrophilicity and stability of the NPs. The presence of grafted PEG may enhance the wettability of the nanoparticles at the interface, leading to improved overall

distribution and contributing to a reduction in IFT. Additionally, PEG may alter the interaction dynamics of the NPs with the liquid phase at the interface, its absorption at the interface can create a "soft layer" that lowers the energy barrier for interfacial formation, further facilitating IFT reduction. Furthermore, the grafting of PEG may render the NPs surface less accessible to ions, potentially influencing surface charge measurements and the kinetics of interactions at the interface.

Surface modification by biotinylating or PEGylating, the hydrophilicity and stability of NPs at the interface have changed, potentially impacting their behavior regarding surface protein adsorption.

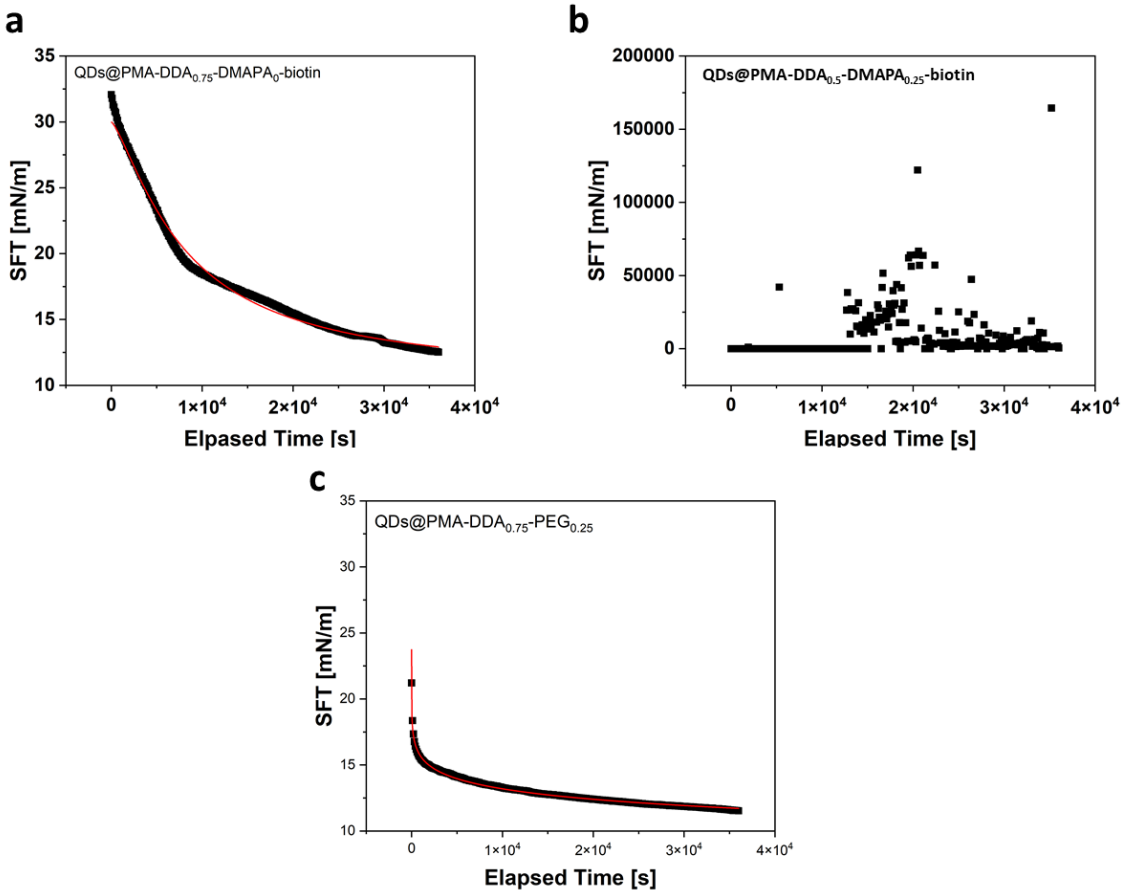

Figure 5-19. Interfacial tension (IFT) of a) QDs@PMA-DDA$_{0.75}$-DMAPA$_0$-biotin, b) QDs@PMA-DDA$_{0.5}$-DMAPA$_{0.25}$-biotin, c) QDs@PMA-DDA$_{0.75}$-PEG$_{0.25}$, the IFT was recorded for 10 hours. The red line represents the fitting by Hua and Rosen equation.

Table 5-8. Dynamic analysis of IFT. Where γ_m is the meso-equilibrium interfacial tension, t_h is the half-life time to reach this value, n is a constant related to the hydrophobicity, v_{max} is the decay rate of the interfacial tension.

NPs	Y_m [mN/m]	t* [s]	n	v_{max} [mN/m s]
QDs@PMA-$DDA_{0.75}$-$DMAPA_0$-biotin	10.54 ± 0.69	8130.25 ± 548.08	1.33 ± 0.10	0.0008
QDs@PMA-$DDA_{0.5}$-$DMAPA_{0.25}$-biotin	---	---	---	---
QDs@PMA-$DDA_{0.75}$-$PEG_{0.25}$	---	---	---	---

5.5 Fabrication of cap-exchanged CdSe-CdS quantum dots

The above polymer encapsulation of quantum dots can produce stable and uniform nanoparticles, but the polymer shell may influence the fluorescence properties and also the behavior of protein adsorption. To better compare the protein corona formation with and without the presence of polymer, in this section, we also directly attach water-soluble ligands to the surface of quantum dots, creating biocompatible QDs NPs.

Due to the high affinity of thiol groups for cadmium, we selected thiol-terminated ligands for cap exchange. This process removes the original oleylamine and TBP from the surface of the quantum dots, replacing them with hydrophilic ligands. In our study, we chose Mercaptocarbonic acid (MUA) and α-Butyric Acid-ω-Mercaptopropanamido PEG (α-Carboxy-ω-Thiol PEG). Compared to short-chain thiols, MUA provides greater steric hindrance, resulting in a more uniform distribution of ligands on the surface of quantum dots. This helps prevent quantum dots aggregation and fluorescence quenching that can occur with excessive cap exchange. Thiol-terminated PEG was used for comparison with PEG-modified polymer. Both cap-exchanged ligands have a carboxyl group at the other end, providing excellent water solubility.

5.5.1 Fabrication of CdSe-CdS@MUA

Mercaptocarbonic acid (MUA, 5 mg) was dissolved in 1 mL of methanol, and potassium hydroxide (KOH, 5 mg) was added to create a stock solution. Then, 1 mL of CdSe-CdS quantum dots stock solution (50 μM) in chloroform was mixed with 1 mL of the MUA stock solution. After vigorous shaking for 5 minutes, the solution turned cloudy. Subsequently, 5 mL of chloroform was added to this mixture. After centrifugation at 8000 rpm for 5 minutes, the MUA-capped nanoparticles precipitated. The methanol and chloroform in supernatant were discarded, and the nanoparticles were re-dissolved in PBS at different pH values, the nanoparticles are named as CdSe-CdS@MUA.

5.5.2 Fabrication of CdSe-CdS@PEG-COOH

α-Butyric Acid-ω-Mercaptopropanamido PEG (α-Carboxy-ω-Thiol PEG, 5 mg) was dissolved in 1 mL methanol, and potassium hydroxide (KOH, 5 mg) was added afterwards to make a stock solution. 1 mL CdSe-CdS quantum dots stock solution (50 uM) in chloroform was mix with 0.5 mL of the α-Carboxy-ω-Thiol PEG stock solution. After vigorous shaking for 5 minutes, 5 mL of hexane was added to this mixture. After centrifugation at 8000 rpm for 5 minutes, the α-Carboxy-ω-Thiol PEG capped nanoparticles precipitated. The methanol, chloroform and hexane in supernatant were removed, and the nanoparticles were re-dissolved in PBS at different pH values, these nanoparticles are named as CdSe-CdS@PEG-COOH.

5.5.3 pH dependent zeta potential of nanoparticles

The NPs were diffused in 1×PBS buffer under different pH value, the zeta potential was measured by Malvern zetasizer.

After cap exchange with MUA, the surface of the QDs becomes functionalized with a long hydrocarbon chain that terminates in a carboxylic acid group. At pH 5, these carboxylic acid groups are predominantly protonated, resulting in a less negatively charged surface, which is reflected in a zeta potential of -21.9 mV. As the pH increases, the carboxylic acid groups progressively deprotonate to form carboxylate anions, introducing additional negative charges to the QDs surface.

In contrast, another NPs system, QDs@PMA-$DDA_{0.75}$-$DMAPA_0$, which also possesses carboxyl groups, exhibits a significantly higher negative charge in the pH range of 5 to 9 when compared to QDs@MUA. This heightened negative charge may be attributed to the conformational behavior of the polymer, which enhances the electrostatic effects at the surface of the nanoparticles. The extended conformation of the polymer chains increases the effective surface area occupied by negative charges, leading to strengthened electrostatic repulsion between the NPs.

Conversely, the surface charge of QDs@PEG-COOH fluctuates within a narrower range of -9 mV to -14 mV. Compared to QDs capped with MUA, this indicates a less negative surface charge for the PEG-capped QDs. Although α-Carboxy-ω-Thiol PEG contains carboxyl groups, its contribution to the overall negative charge is relatively low. This can be attributed to steric hindrance and the hydrophilic nature of the polymer, which may impede effective stacking or interaction of the carboxylic acid groups, limiting the net negative charge imparted to the nanoparticles.

The lower surface charge observed for QDs@PEG-COOH suggests reduced electrostatic repulsion between the nanoparticles, which may adversely affect their stability in solution. Therefore, we further investigated the stability of QDs@MUA and QDs@PEG-COOH under varying pH conditions and different ionic strengths in subsequent experiments.

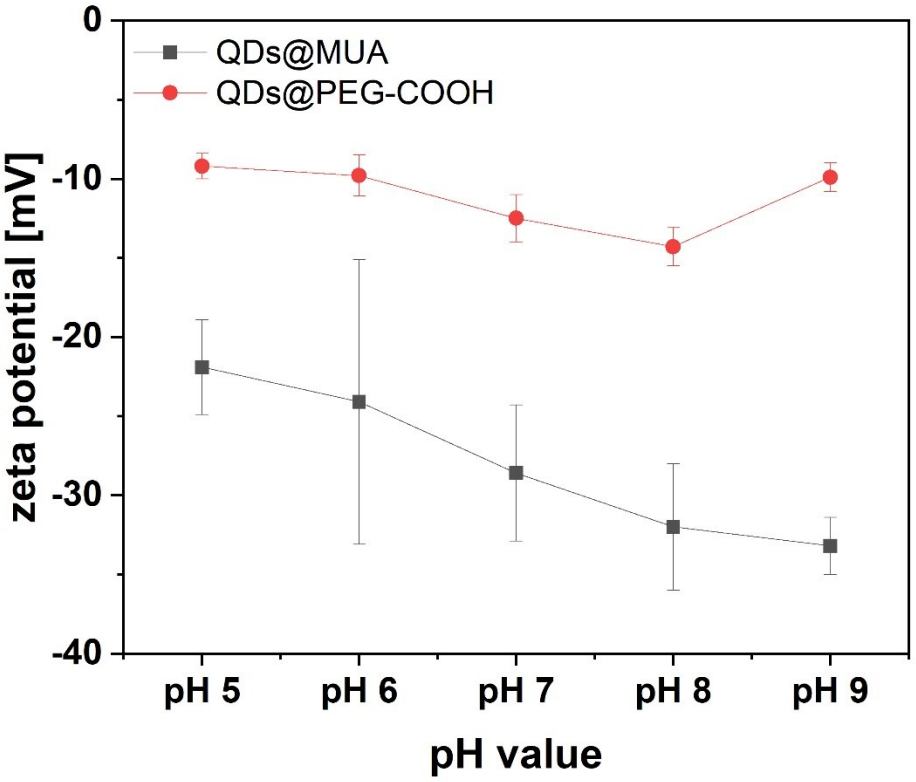

Figure 5-20. Zeta potential (ζ) in function of pH value of QDs@MUA and QDs@PEG-COOH.

Table 5-9. Zeta potential (ζ) in function of pH value of QDs@MUA and QDs@PEG-COOH.

Zeta potential (ζ)	pH 5	pH 6	pH 7	pH 8	pH 9
QDs@MUA	-21.9 ± 3.0	-24.1 ± 9.0	-28.6 ± 4.3	-32.0 ± 4.0	-33.2 ± 1.8
QDs@PEG-COOH	-9.2 ± 0.8	-9.8 ± 1.3	-12.5 ± 1.5	-14.3 ± 1.2	-9.9 ± 0.9

5.5.4 pH dependent hydrodynamic size of nanoparticles

The hydrodynamic size of NPs was recorded under different pH conditions by zeta sizer, size distribution is shown in Figure 5-21.

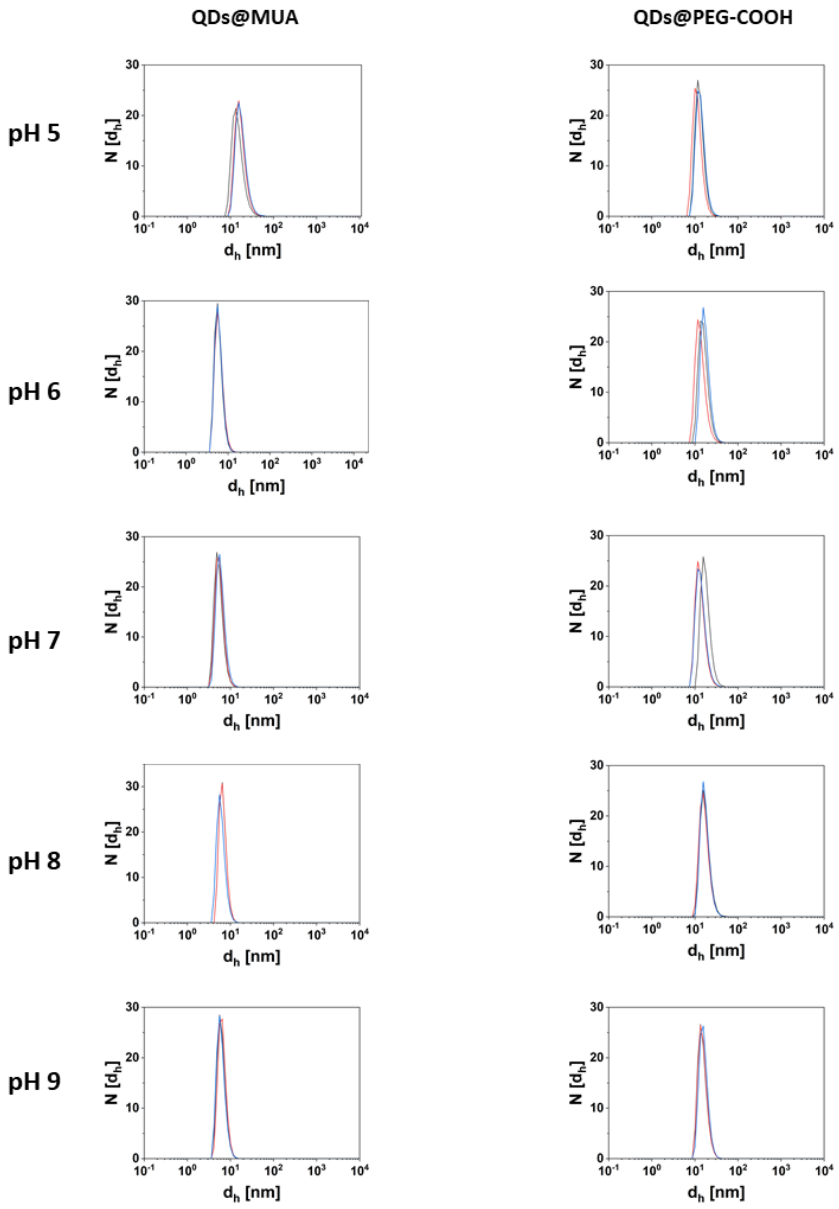

Figure 5-21. pH dependent hydrodynamic size of QDs@MUA and QDs@PEG-COOH.

The results indicate that these NPs above exhibit good colloidal stability, with particle size remaining relatively constant across different pH conditions. This stability provides a strong foundation for our subsequent investigations into protein corona formation under varying pH environments.

5.5.5 NaCl concentration dependent hydrodynamic size of nanoparticles

The hydrodynamic size of NPs was recorded under different NaCl concentration by zeta sizer, size distribution is shown in Figure 5-22.

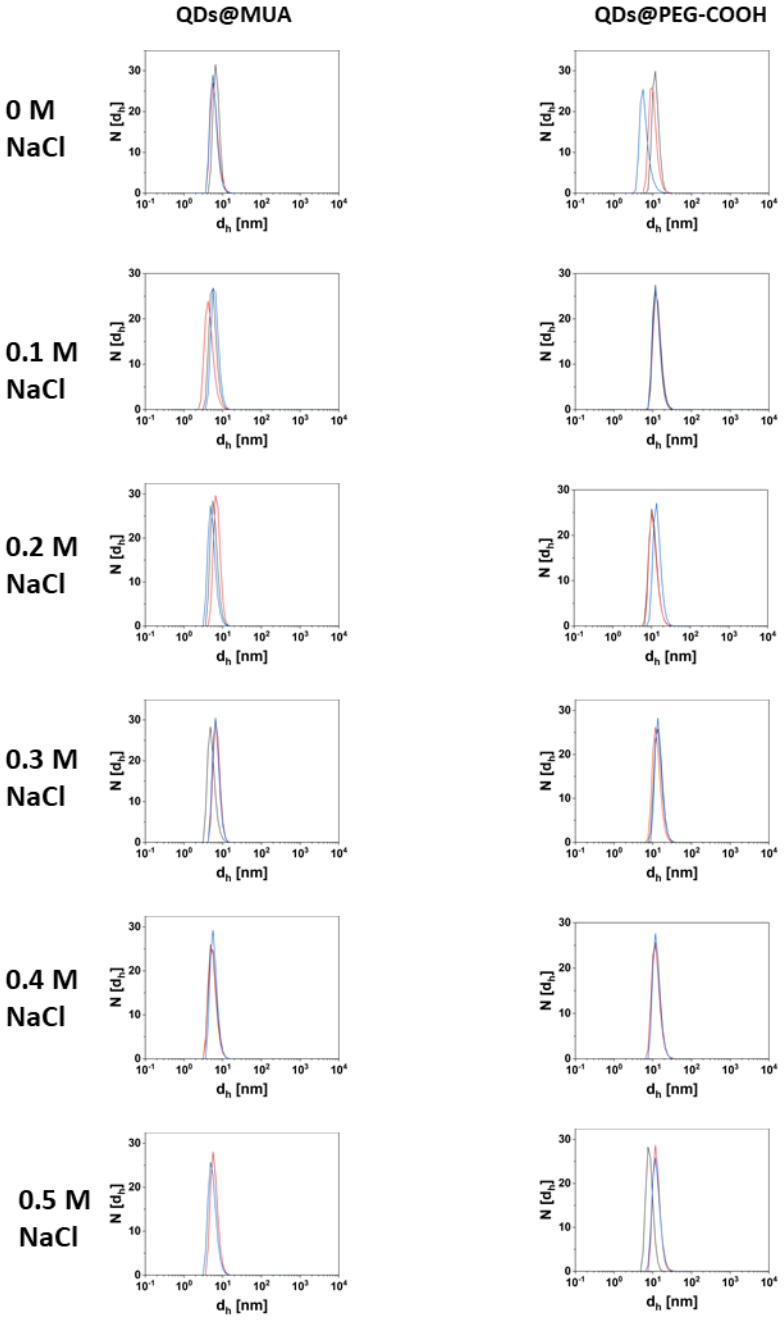

Figure 5-22. Hydrodynamic diameter of NPs in 0-0.5 M NaCl solution. The results are presented as number weighted distributions and measurements were recorded in triplicates.

The results indicate that these NPs above exhibit good colloidal stability, with particle size remaining relatively constant across different NaCl concentrations. This stability provides a strong foundation for our subsequent investigations into protein corona formation in PBS buffer.

5.5.6 Interfacial tension of nanoparticles

The IFT measurements of QDs-polymer conjugates were recorded by the drop shape analyzer. We used the pendant drop method for the measurement, where we produced 30 µL drop of each nanoparticle solution in a transparent glass cup filled with toluene. The shape of the drop depends on the relationship between the interfacial tension and gravity. In this method, the IFT can be calculated from the projection of the hanging drop recording by a high frame rate camera implemented with the drop shape analyzer. The QDs-polymer NPs were loaded into a syringe which was then equipped with a stainless-steel needle (diameter: 1.28 mm) to produce a 30 µL drop of NPs solution. The photographs of the pendant drop were recorded for 10 hours. The IFT was calculated using the principal radius of curvature of the drop, and further calculated according to Young-Laplace fitting as shown in Figure 5-23. and the change of IFT was further fitted by Hua and Rosen equation, the parameters are shown in Table 5-10.

Compared to QDs@PMA-$DDA_{0.75}$-$DMAPA_0$, which also features free carboxyl groups on the surface, QDs@MUA—synthesized from direct ligand exchange which exhibit lower IFT and took longer time to reach equilibrium than the polymer-coated NPs. This behavior suggests that the hydrocarbon chains in the MUA structure interact favorably with toluene, thereby enhancing adsorption and stabilization at the interface and significantly reducing IFT compared to the polymer-coated NPs. In contrast to the more spatially constrained environment created by the polymer layer on QDs@PMA-$DDA_{0.75}$-$DMAPA_0$, the ligands on QDs@MUA provide greater flexibility and dynamic rearrangement potential at the interface. This flexibility allows MUA-capped QDs to adapt quickly and align favorably at the water-toluene interface, facilitating the formation of a stable interface and further lowering IFT. Regarding the impact of surface charge on IFT, although both of QDs@PMA-$DDA_{0.75}$-$DMAPA_0$ and QDs@MUA possess carboxyl groups that contribute to stability, the direct ligand exchange process in QDs@MUA may result in a distinct charge distribution and interaction dynamics at the interface. This could influence the electrostatic repulsion and adsorption efficiency at the water-toluene boundary.

The IFT of QDs@PEG-COOH is comparable to that of QDs@PMA-$DDA_{0.75}$-$PEG_{0.25}$ but exhibits a two-stage decrease, characterized by a slower decline in the first stage followed by a more rapid decline in the second stage. The final IFT reaches approximately 11 mN/m, which can be attributed to several factors related to the interactions at the water-toluene interface and the surface modification properties of the QDs. In the initial stage, the

slower rate of decrease in IFT is likely due to the initial adsorption of QDs@PEG-COOH at the water-toluene interface. During this phase, the NPs began to orient themselves at the interface, facilitating interactions between the PEG-COOH functional groups and the aqueous phase. This stage is characterized by the gradual alignment of the hydrophilic PEG segments toward the aqueous phase, while hydrophobic interactions started to dominate at the interface. As IFT decreases, the ligands on the QDs may undergo rearrangement. In this initial phase, the surface ligands might not be fully optimized for interface positioning, leading to a moderate reduction in tension. The system is in an adaptation phase, with some PEG chains still interacting with water and gradually optimizing the surface configuration. After this initial adsorption phase, the surfactant behavior of PEG-COOH became more pronounced. In the second stage, the primary interactions at the interface might shift towards greater hydrophobic contributions relative to PEG, as the hydrophilic groups became fully engaged with the water phase. This effectively accelerated the reduction in IFT, while the hydrophobic regions interacted more effectively with the toluene phase. Additionally, the surface charge of QDs@PEG-COOH is higher than that of QDs@PMA-$DDA_{0.75}$-$PEG_{0.25}$. This difference in charge distribution may also influence the rate of IFT decrease.

In comparison to polymer-coated NPs, we observed that direct ligand exchange to facilitate the phase transformation of QDs alters the hydrophilic and hydrophobic properties of the NPs, as well as their capacity to achieve equilibrium at the aqueous-organic interface.

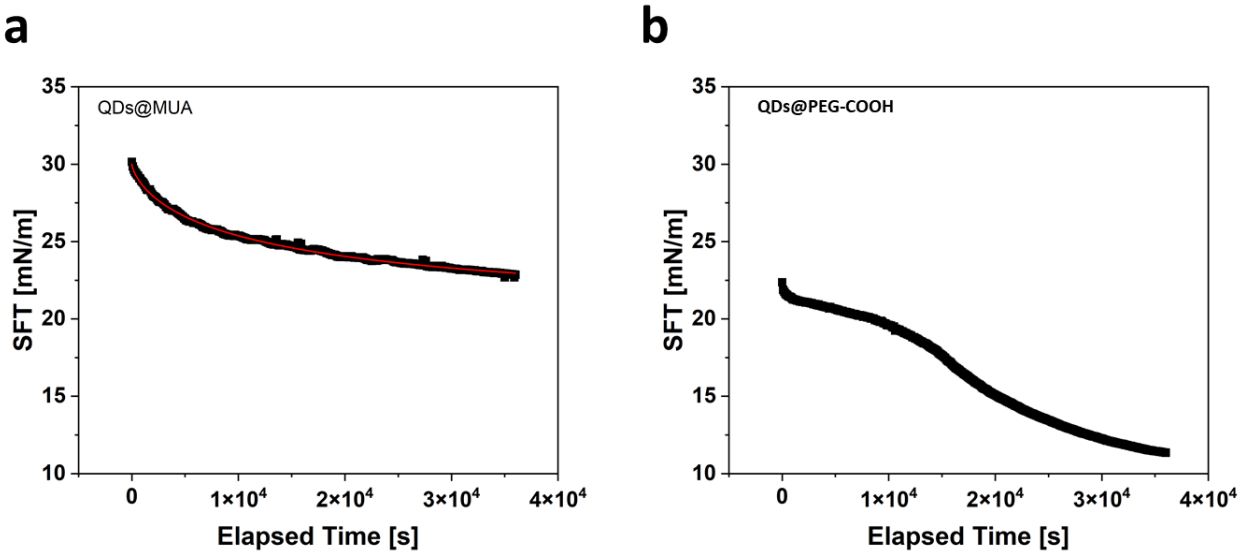

Figure 5-23. Interfacial tension (IFT) of a) QDs@MUA, b) QDs@PEG-COOH, the IFT was recorded for 10 hours. The red line represents the fitting by Hua and Rosen equation.

Table 5-10. Dynamic analysis of IFT. Where γ_m is the meso-equilibrium interfacial tension, t_h is the half-life time to reach this value, n is a constant related to the hydrophobicity, ν_{max} is the decay rate of the interfacial tension.

NPs	Y_m [mN/m]	t* [s]	n	ν_{max} [mN/m s]
QDs@MUA	19.22 ± 0.18	14899.32 ± 720.69	0.72 ± 0.01	0.00013
QDs@PEG-COOH	---	---	---	---

6. Evaluation of protein corona

6.1 FCS measurements of protein corona

The FCS measurements in this section were conducted under different pH conditions, ranging from pH 5 to pH 9, aim to investigate how variations in the acidity or alkalinity of the environment can influence the formation of the protein corona.

pH has a significant impact on protein structure, stability, and conformational changes. By studying protein corona formation at different pH levels, researchers can explore the impact on protein structural integrity, which may lead to changes in proteins-NPs binding affinity and the overall structure of protein corona.

pH changes also affect the nature and strength of interactions between proteins and NPs, including electrostatic forces, hydrophobic interactions, and hydrogen bonds. By studying protein corona formation over a wide pH range, we can demonstrate how pH affects the binding kinetics, specificity, and diversity of proteins in the corona. Understanding how pH affects the protein corona can provide insights into the fate, behavior, and potential impact of NPs in different bioenvironments.

6.1.1 Sample preparation for FCS measurements

Protein sample solution preparation

The proteins (BSA, Transferrin, Lysozyme and pepsin) were weight and dissolved in 1×PBS buffer with different Ph to make 1000 μM stock solution. Then the stock solutions were diluted into 500 μM, 200 μM, 100 μM, 50 μM, 20 μM, 10 μM, 5 μM, 2 μM, 1 μM, 0.2 μM, 0.02 μM, 0.002 μM and 0.0002 μM.

Because Avidin molecules have extremely strong affinity for biotin, we chose a lower concentration range for our study. The concentrations of Avidin solutions were 2 μM, 1.5 μM, 1 μM, 0.5 μM, 0.2 μM, 0.1 μM, 0.05 μM, 0.02 μM, 0.01 μM, 0.005 μM, 0.002 μM, 0.0002 μM and 0.00002 μM.

Proteins-NPs mixture preparation

The protein solutions prepared above were further mix with NPs with different surface chemistry The above protein solution will be further mixed with nanoparticles with different surface modifications in a 1:1 volume ratio. Finally, the concentration of nanoparticles in the solution is about 50 nM and the protein concentration is 500 μM, 250 μM, 100 μM, 50 μM, 25 μM, 10 μM, 5 μM, 2.5 μM, 1 μM, 0.5 μM, 0.1 μM, 0.01 μM, 0.001 μM, 0.0001 μM for BSA, Transferrin, pepsin and Lysozyme. And for Avidin, the concentration changes to 1 μM, 0.75 μM, 0.5 μM, 0.25 μM, 0.1 μM, 0.05 μM, 0.025 μM,

0.01 μM, 0.005 μM, 0.0025 μM, 0.001 μM, 0.0001 μM, 0.00001 μM. The mixture was incubated in room temperature for 30 minutes before measurement.

6.2 Analysis and Fitting of FCS Data

From the diffusion coefficient we obtained during the measurements, we can calculate the hydrodynamic radius of NPs after protein adsorption. With the increasing of protein adsorption, we could also observe the diffusion time of NPs shifted toward longer time, which indicates the increasing of NPs' size (Figure 6-1). To obtain more quantitative results about the adsorption process, we chose the Hill model, one of the thermodynamic models, to fit the change in hydrodynamic radius, thus briefly describing the relationship between the adsorption of protein corona on NPs and concentration. The Hill model was first proposed in 1910 to describe the binding of ligands to macromolecules, especially in the context of enzyme kinetics and receptor-ligand interactions. It provides insights into how the concentration of ligand affects its binding to the target, allowing the characterization of cooperative behaviors between multiple binding sites.[96-98]

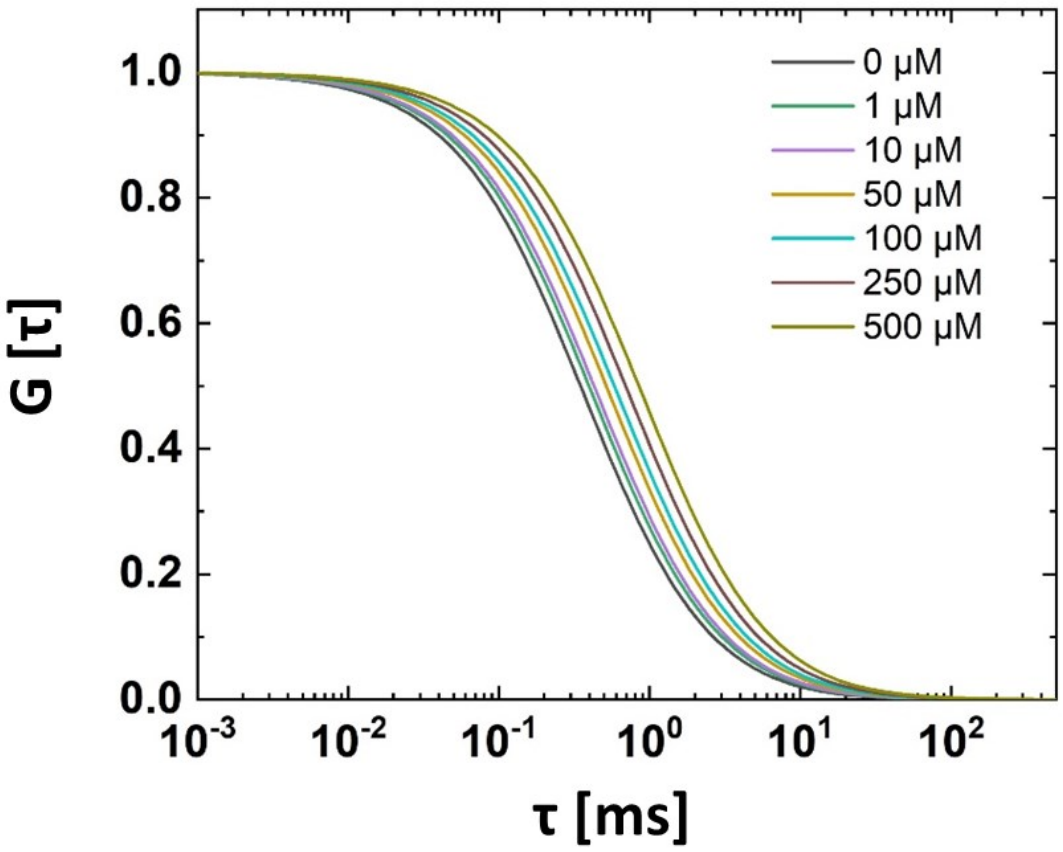

Figure 6-1. Autocorrelation curve of QDs@PMA-$DDA_{0.75}$-$DMAPA_0$ NPs after incubate with BSA at concentration of 0 μM to 500 μM.

According to the law of conservation of mass, if a NP interacts with n proteins P to form a protein-NPs complex, the proportion of saturated NPs is equal to the proportion of protein-occupied sites on the NP surface.

$$NP + n \cdot P \leftrightarrow P_n NP \tag{6-1}$$

The dissociation coefficient of this dynamic equilibrium is,

$$K_d = \frac{[N][P]^n}{[P_n NP]} \tag{6-2}$$

After NPs mix with proteins, the initial concentration of the NPs equals to the sum of free NPs in solution [NP] and the NPs that already formed complex $[P_n NP]$. Therefore, the ratio of saturated NPs is,

$$\frac{N}{N_{max}} = \frac{[P_n NP]}{[NP] + [P_n NP]} \tag{6-3}$$

Rather than using the dissociation coefficient, we propose utilizing the concentration that results in half-saturation, which is k_d. Here $k_d = (K_D)^n$, allowing the number of occupied sites to be described as follows,

$$N = \frac{N_{max}}{1 + \left(\frac{K_D}{[P]}\right)^n} \tag{6-4}$$

The Hill coefficient serves as an empirical parameter that quantifies the steepness of the adsorption profile and provides insight into the cooperativity of protein adsorption. when n>1, which means a positive cooperative binding, once the proteins are adsorbed, it will increase the likelihood for other proteins adsorption. And when n<1, it means a negative cooperative binding, once the proteins are adsorbed on the surface of NPs, it will decrease the likelihood for other proteins adsorption. And when n=1, it means a non-cooperative binding, each of protein's adsorption behavior is independent from others.

With the knowledge of the number of proteins adsorbed on the surface of the NPs, we can determine the change in their hydrodynamic size. If N proteins, each with a volume Vp, are adsorbed onto the NPs, the relationship governing the total volume of the adsorbed proteins can be described as follows:

$$V_{(N)} = V_0 + N \cdot V_p \tag{6-5}$$

In this case, if we define the ratio of the volume of protein to the volume of the NPs prior to any protein adsorption as $c = \frac{V_P}{V_0}$, referring back to equation above, we can

describe the hydrodynamic radius of the NPs as a function of the number of absorbed proteins as equation 6-6.

$$R_{h(N)} = R_{h(0)}(1 + c \cdot N)^{\frac{1}{3}} \quad (6\text{-}6)$$

By using this equation to fit the change of the hydrodynamic radius obtained by FCS, we can derive different quantitative parameters to be used to describe and compare different protein adsorption profiles, as will be discussed in the following sections.

6.3 Data analysis of FCS measurement

6.3.1 FCS measurements of pH-dependent BSA adsorption on different nanoparticles

Table 6-1 shows the predicted change in the overall charge of BSA from pH 5 to pH 9. At pH 5 and pH 6, protonation of the amino groups on the basic amino acids results in a positive charge on BSA due to being below its pKa value. Moving to pH 7, BSA approaches a neutral charge because some basic amino acids undergo partial deprotonation, resulting in a balance between positive and negative charges. As the pH increases to 8 and 9, deprotonation of the basic amino groups results in an overall negative charge on the protein. Understanding the change in surface charge of BSA can better explain its adsorption behavior on the surface of NPs.

Table 6-1. Predicted charge of BSA under pH 5 to pH 9.

Predicted charge (+/-)	pH 5	pH 6	pH 7	pH 8	pH 9
BSA	+	+/-	-	-	-

The QDs@PMA-$DDA_{0.75}$-$DMAPA_0$ NPs exhibit a negative charge (approximately -70 mV) within the pH range of 5 to 9, and electrostatic interactions play a significant in the adsorption of BSA. At pH 5, BSA is near its pl, resulting in a moderate positive charge that leads to some electrostatic attraction. However, this is insufficient to promote significant binding. This is reflected in the high Kd value of 1151.34 μM, indicating weak binding affinity and potential dominance of electrostatic repulsion. As the pH increases, BSA transitions to a slightly negative charge, leading to a significant decrease in Kd values (204.59 μM at pH 6 and 40.22 μM at pH 7), indicating stronger binding of the protein to the NPs. At pH 6, 7, and 8, the Hill coefficient n approaches 1, suggesting that the binding of one BSA molecule may facilitate the binding of additional molecules, which also indicating slight cooperativity in the adsorption system. In contrast, at pH 5 and 7, n values fall below 1, indicating negative cooperativity, where the binding of one BSA molecule decreases the likelihood of further binding due to steric hindrance or saturation of binding

sites. A higher n value at pH 9 (n = 1.89) indicates strong positive cooperativity, suggesting that binding becomes very favorable and that interactions among BSA molecules significantly enhance adhesion to the NPs surface. Interestingly, at pH 5, the maximum binding capacity (Nmax) is higher (120.53), indicating that, despite the lower affinity between BSA and the NPs, there are more available binding sites before significant saturation occurs at lower concentrations It is noteworthy that with increasing pH, both BSA and NPs become more negatively charged, but the adsorption of BSA on the NPs surface increases, indicating that protein adsorption is not driven solely by electrostatic effects. Adsorption can induce conformational changes in BSA that enhance adhesive interactions with NPs, and the ability of BSA to orient relative to the NPs surface may increase with the increased presence of more negatively charged proteins, which can enhance cooperative binding.

For the QDs@PMA-$DDA_{0.5}$-$DMAPA_{0.25}$ NPs, no adsorption of BSA was observed during the measurements. This may be attributed to the zwitterionic nature of the NPs, which possess both positive and negative charges, rendering them electrically neutral in the pH range of 5 to 9. This neutrality minimizes potential electrostatic attraction with oppositely charged proteins. Furthermore, the hydration layer formed on the surface of the zwitterionic NPs creates a barrier that reduces direct contact between proteins and the NPs surface. Additionally, the dense zwitterionic groups on the surface produce steric hindrance, physically interfering with proteins attempting to approach and bind to the NPs. This steric repulsion further inhibits protein adsorption.

The QDs@PMA-$DDA_{0.5}$-$DMAPA_{0.5}$ NPs exhibited a positive charge in the pH range of 5 to 9 but did not demonstrate any adsorption of BSA. This lack of adsorption may be attributed to the relatively low surface charge of the NPs. The positive charge from DMAPA, combined with the negative charge from the carboxyl groups on the PMA backbone, created a zwitterionic environment that hindered further adsorption of BSA.

QDs@PMA-$DDA_{0.25}$-$DMAPA_{0.75}$ NPs also carry a positive charge in the pH range of 5 to 9, which facilitates electrostatic attraction to BSA. The lowest Kd value is observed at pH 5, indicating that the acidic environment enhances the binding affinity between BSA and the positively charged NPs. The highest Kd value occurs at pH 6, likely due to some neutralization of charge interactions. Following this, the Kd values decrease at pH levels 7 to 9, but remain higher than at pH 5. This suggests that BSA may undergo conformational changes during adsorption at these pH levels, and its binding is not only driven by electrostatic interactions. The Hill coefficient showed strong positive cooperativity at pH 5, 7, 8, and 9, however, at pH 6, the n value of 1.05 indicated that the system exhibited non-cooperative binding under this condition, and the Nmax value was higher at 53.63, indicating that more BSA could be adsorbed to the NPs surface at this pH despite the lower binding affinity. This suggests that the interaction kinetics allow for more access to the surface for BSA, possibly leading to less tightly bound proteins and the formation of multilayer adsorption. At pH 5, although the binding affinity was the highest,

the number of available binding sites appeared to be limited relative to the adsorption capacity, indicating tighter monolayer binding at this time.

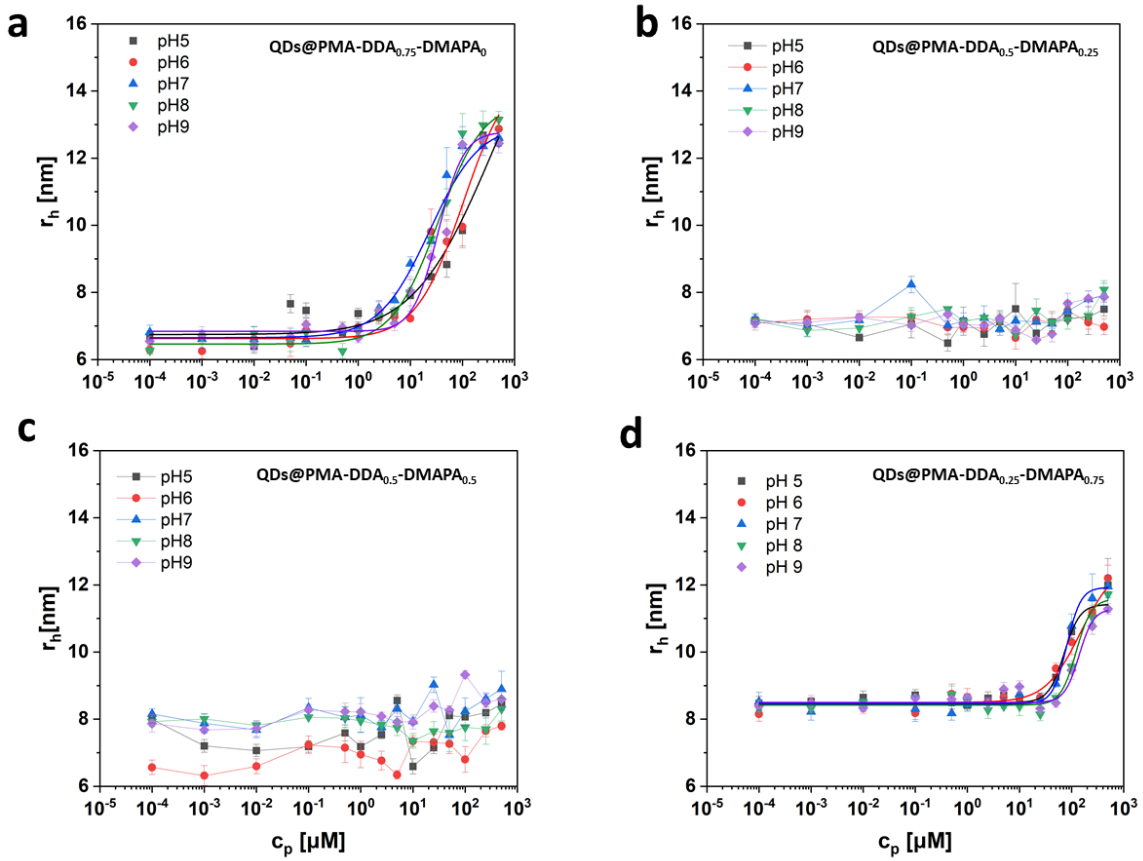

Figure 6-2. Radius(r_h)-Concentration(c_p) curve of a) QDs@PMA-DDA$_{0.75}$-DMAPA$_0$, b) QDs@PMA-DDA$_{0.5}$-DMAPA$_{0.25}$, c) QDs@PMA-DDA$_{0.5}$-DMAPA$_{0.5}$ and d) QDs@PMA-DDA$_{0.25}$-DMAPA$_{0.75}$ of BSA adsorption. The lines present the fitting by Hill function.

Table 6-2. Analyzing of FCS data of BSA adsorption on QDs@PMA-DDA$_{0.75}$-DMAPA$_0$, QDs@PMA-DDA$_{0.5}$-DMAPA$_{0.25}$, QDs@PMA-DDA$_{0.5}$-DMAPA$_{0.5}$ and QDs@PMA-DDA$_{0.25}$-DMAPA$_{0.75}$. R_0 stands for the original radius of the NPs, k_d indicates the protein concentration at half saturation stage, n is the Hill coefficient, N_{max} represents the maximum number of proteins that can adsorb onto a single NP, and ΔR_h is the difference between the radius at maximum adsorption and the NP's original radius.

NPs	pH	R_0 [nm]	K_d [μM]	n	N_{max}	ΔR_h [nm]
QDs@PMA-DDA$_{0.75}$-DMAPA$_0$	5	6.75	1151.34	0.68	120.53	5.75
	6	6.63	204.59	1.07	72.69	6.25

	7	6.65	45.22	0.97	48.52	5.95
	8	6.46	64.99	1.08	58.39	6.68
	9	6.84	47.51	1.89	45.25	5.60
QDs@PMA-$DDA_{0.5}$-$DMAPA_{0.25}$	5	8.69	---	---	---	---
	6	8.48	---	---	---	---
	7	8.46	---	---	---	---
	8	8.35	---	---	---	---
	9	7.98	---	---	---	---
QDs@PMA-$DDA_{0.5}$-$DMAPA_{0.5}$	5	8.83	---	---	---	---
	6	8.56	---	---	---	---
	7	8.76	---	---	---	---
	8	8.40	---	---	---	---
	9	8.77	---	---	---	---
QDs@PMA-$DDA_{0.25}$-$DMAPA_{0.75}$	5	8.60	79.05	3.21	21.07	3.38
	6	8.41	386.45	1.05	53.63	3.78
	7	8.46	89.99	3.27	27.88	3.49
	8	8.42	135.93	2.96	24.48	3.30
	9	8.57	155.27	3.33	20.57	2.71

We subsequently performed BSA adsorption experiments on NPs modified with either biotin or PEG on their surfaces.

After modifying the surface with biotin, the surface charge of QDs@PMA-$DDA_{0.75}$-$DMAPA_0$-biotin slightly decreased, however, it remained negatively charged within the pH range of 5 to 9. The adsorption behavior of BSA was largely consistent with that of the QDs@PMA-$DDA_{0.75}$-$DMAPA_0$ NPs. The affinity of the NPs for BSA was lowest at pH 5, with the K_d of 725.83 μM. As the pH increases, the K_d value decreases, indicating that the affinity of BSA to NPs continues to increase and is significantly higher than the affinity at pH 5. From the fitted n value, it can be seen that at pH 5, pH 6 and pH 8, the n value is less than 1, indicating that BSA is non-cooperatively adsorbed; at pH 7, the n value exceeds 1, indicating that BSA is cooperatively adsorbed; at pH 9, the n value is close to 1, indicating that the adsorption of BSA is independent and does not interfere with each other. There are obvious differences in the maximum adsorption amount of BSA under

different pH conditions. At pH 5, although BSA has the weakest affinity for NPs, Nmax is the largest, indicating that a relatively loose multilayer structure has been formed. As the pH increases, Nmax gradually decreases, and the values are similar at pH 8 and pH 9, indicating that BSA is likely to form a tight monolayer protein corona on the surface of NPs.

After biotin surface modification, zwitterionic polymer-coated QDs@PMA-$DDA_{0.5}$-$DMAPA_{0.25}$-biotin NPs showed no BSA adsorption between pH 5 and pH 7. However, adsorption was observed at pH 8 and pH 9. Biotin-modified zwitterionic NPs increased the zeta potential, thereby reducing the electrostatic repulsion, making it easier for BSA to adsorb onto the NPs surface. In addition, the hydration layer around the zwitterionic NPs hinders protein adsorption. However, at higher pH values, the stability of this hydration layer may be reduced, thereby promoting increased protein adsorption. The Kd values indicate stronger binding affinity at higher pH values, with Kd of 206.84 µM at pH 8 and 123.16 µM at pH 9. The n values further indicate strong cooperative binding at high pH, with readings of 5.26 at pH 8 and 16.43 at pH 9. This suggests that when BSA molecules bind to NPs, they promote further binding through conformational changes or aggregation effects. In addition, the Nmax value also increases with pH, indicating that BSA forms a more compact and efficient monolayer structure at higher pH values. Biotin-modified zwitterionic NPs exhibit complex biochemical interactions that increasingly favor BSA adsorption as pH increases.

Following the partial grafting of PEG-CH_3O into the polymer, the surface charge of the QDs@PMA-$DMAPA_{0.75}$-$PEG_{0.25}$ NPs became reduced and negatively charged. As a result, there was no observable BSA adsorption within the pH range of 5 to 9. This phenomenon can be attributed partly to electrostatic repulsion, as well as the increased steric hindrance caused by the flexible PEG chains, which hinder the approach of BSA molecules. Additionally, the hydration layer formed by PEG on the NPs' surface further inhibits protein adsorption.

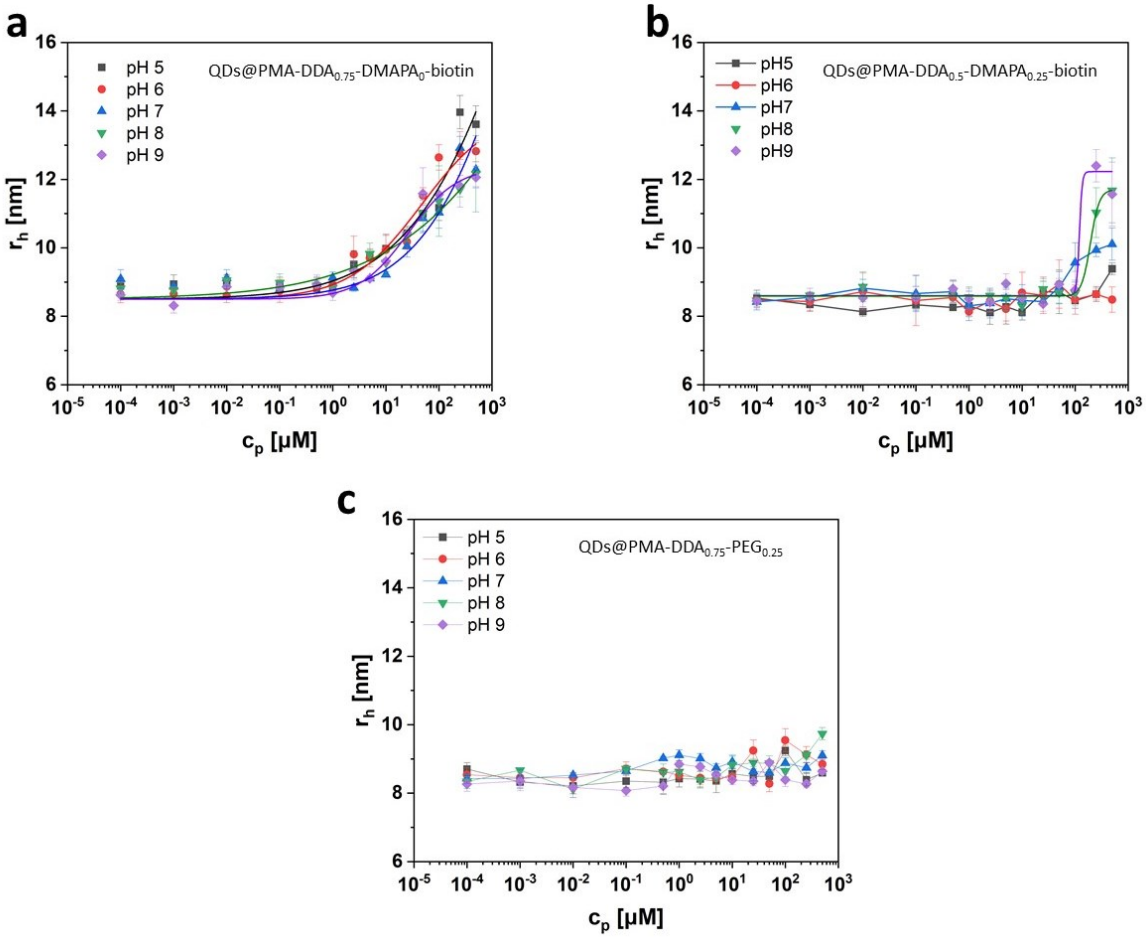

Figure 6-3. Radius(r_h)-Concentration(c_p) curve of a) QDs@PMA-DDA$_{0.75}$-DMAPA$_0$-biotin, b) QDs@PMA-DDA$_{0.5}$-DMAPA$_{0.25}$-biotin, c) QDs@PMA-DDA$_{0.75}$-PEG$_{0.25}$ of BSA adsorption. The lines present the fitting by Hill function.

Table 6-3. Analyzing of FCS data of BSA adsorption on QDs@PMA-DDA$_{0.75}$-DMAPA$_0$-biotin, QDs@PMA-DDA$_{0.5}$-DMAPA$_{0.25}$-biotin and QDs@PMA-DDA$_{0.75}$-PEG$_{0.25}$. R_0 stands for the original radius of the NPs, k_d indicates the protein concentration at half saturation stage, n is the Hill coefficient, N_{max} represents the maximum number of proteins that can adsorb onto a single NP, and ΔR_h is the difference between the radius at maximum adsorption and the NP's original radius.

NPs	pH	R_0 [nm]	K_d [µM]	n	N_{max}	ΔR_h [nm]
QDs@PMA-DDA$_{0.75}$-DMAPA$_0$-biotin	5	8.80	725.83	0.65	117.36	4.80
	6	8.67	69.31	0.82	47.67	4.14
	7	8.88	79.67	1.33	38.96	3.40

	8	8.85	40.12	0.87	28.29	3.31
	9	8.74	33.68	1.20	28.47	3.31
QDs@PMA-$DDA_{0.5}$-$DMAPA_{0.25}$-biotin	5	8.53	---	---	---	---
	6	8.48	---	---	---	---
	7	8.42	---	---	---	---
	8	8.59	206.84	5.26	24.74	3.09
	9	8.60	123.16	16.43	30.45	2.96
QDs@PMA-$DDA_{0.75}$-$PEG_{0.25}$	5	8.71	---	---	---	---
	6	8.54	---	---	---	---
	7	8.43	---	---	---	---
	8	8.34	---	---	---	---
	9	8.27	---	---	---	---

Lastly, we examined the adsorption behavior of BSA on cap exchanged QDs@MUA NPs and QDs@PEG-COOH NPs. The changes in NPs radius in relation to protein concentration are recorded in Figure 6-4, with the results of the data fitting presented in Table 6-4.

The adsorption patterns of BSA on QDs@MUA varied significantly across different pH conditions. The binding affinity, represented by the dissociation constant (K_d), was lower under acidic conditions (pH 5 and pH 6), indicating a decrease in affinity with increasing pH. The K_d value under pH 7 (723.64 μM) was higher than other pH conditions, suggesting that the interaction between BSA and the NPs was weakest under this pH. This phenomenon may be due to diminished electrostatic interactions at physiological pH (7.4), where the charged surfaces of BSA and the NPs likely repel one another. From pH 7 to pH 9, we observed a decrease in the K_d value, indicating a gradual increase in binding affinity. This enhancement may arise from an increased surface charge on the NPs or conformational changes in BSA that promote adsorption.

The adsorption pattern of BSA on QDs@MUA showed significant differences under different pH conditions. The binding affinity Kd showed lower binding under acidic conditions (pH 5 and pH 6), while the Kd value at pH 7 (723.66 μM) was the highest, indicating that the interaction between BSA and NPs was the weakest at this pH. This phenomenon may be due to the weakened electrostatic interaction at physiological pH (7.4), when the charged surfaces of BSA and NPs may repel each other. From pH 7 to pH 9, we observed a decrease in the Kd value, indicating that the binding affinity gradually

increased again. This enhancement may be due to the increase in surface charge on NPs or conformational changes in BSA that promote adsorption.

Nmax was lower under acidic conditions but peaked at pH 7 and subsequently decreased but remained above the binding capacity under acidic conditions. This suggests that despite the lower binding affinity under acidic conditions, BSA forms a stable protein corona around QDs@MUA NPs, thereby reaching the saturation phase faster. The results show that pH significantly affects the adsorption behavior of BSA on QDs@MUA NPs. Lower pH values enhance binding due to favorable electrostatic interactions, while neutral and alkaline pH levels modulate these interactions, affecting the extent of adsorption and the nature of binding cooperativity.

The QDs@PEG-COOH NPs exhibit only a weak negative charge across the pH range of 5 to 9. The presence of grafted PEG chains imparts them with the ability to resist protein adsorption. In the FCS test, no increase in NPs size was observed, indicating that there was no adsorption of BSA on the surface of the NPs.

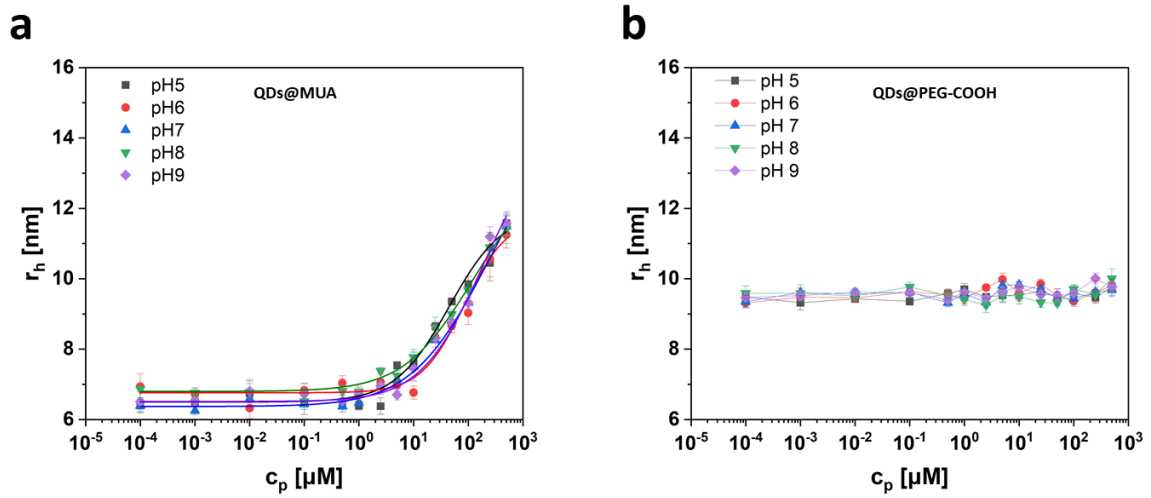

Figure 6-4. Radius(r_h)-Concentration(c_p) curve of a) QDs@MUA and b) QDs@PEG-COOH of BSA adsorption. The lines present the fitting by Hill function.

Table 6-4. Analyzing of FCS data of BSA adsorption on QDs@MUA and QDs@PEG-COOH. R_0 stands for the original radius of the NPs, k_d indicates the protein concentration at half saturation stage, n is the Hill coefficient, N_{max} represents the maximum number of proteins that can adsorb onto a single NP, and ΔR_h is the difference between the radius at maximum adsorption and the NP's original radius.

NPs	pH	R_0 [nm]	K_d [μM]	n	N_{max}	ΔR_h [nm]
QDs@MUA	5	6.42	103.32	0.84	37.85	5.18

	6	6.76	133.30	1.16	33.25	4.31
	7	6.37	723.66	0.69	73.40	5.09
	8	6.80	290.26	0.74	50.14	4.55
	9	6.51	443.14	0.84	66.22	5.07
QDs@PEG-COOH	5	9.48	---	---	---	---
	6	9.31	---	---	---	---
	7	9.35	---	---	---	---
	8	9.59	---	---	---	---
	9	9.47	---	---	---	---

6.3.2 FCS measurements of pH-dependent Transferrin adsorption on different nanoparticles

Table 6-5 illustrates the expected change in the total charge of transferrin over the pH range from 5 to 9. It is known that the isoelectric point of transferrin is about 6.2, and transferrin is positively charged at pH 5 and pH 6. At pH 7, transferrin is electrically neutral and exists as a zwitterion, the positive and negative charges keep balanced. The negative charge increases at higher pH values (pH 8 and pH 9).

Table 6-5. Predicted charge of Transferrin under pH 5 to pH 9.

Predicted charge (+/-)	pH 5	pH 6	pH 7	pH 8	pH 9
Transferrin	+	+	+/-	-	-

We first studied the Transferrin adsorption on NPs with different surface charge. The FCS result is recorded as radius change in Figure 6-5, and the data is further analyzed by Hill function in Table 6-6.

The Transferrin adsorption on QDs@PMA-$DDA_{0.75}$-$DMAPA_0$ varied from different pH conditions. The Kd values for transferrin were relatively low at pH 5, indicating strong adsorption affinity at these levels, and increased at pH 6, reaching a maximum value (53.27 μM) at pH 7, indicating a continued decrease in adsorption affinity, which may be due to weak charge interactions at this pH. At pH 8 and pH 9, the Kd values increased slightly but remained higher than the Kd values observed at pH 5, indicating that while some adsorption occurred at these pH levels, it was not as stable as at lower pH. The n values at pH 5 to 7 were less than 1, indicating that the adsorption process may be limited

by the availability of binding sites. In contrast, at pH 8 and pH 9, especially at pH 8 (n = 2.24), the n values exceeded 1, indicating cooperative adsorption behavior. This suggests that the binding of one transferrin may promote the binding of other molecules, possibly due to structural changes in transferrin that expose more binding sites. At pH 5 and pH 6, high binding affinity and maximum adsorption capacity reflect favorable interactions, which may be due to electrostatic interactions and van der Waals attractions. In contrast, at pH 7, protein adsorption decreased, probably because transferrin carries more negative charges, resulting in repulsion between transferrin and negatively charged NPs. As pH increases to 8 and 9, the adsorption capacity recovers slightly but is still lower than that under acidic conditions, and the synergy index suggests that conformational changes in transferrin may allow more binding to NPs despite unfavorable charge interactions.

QDs@PMA-$DDA_{0.5}$-$DMAPA_{0.25}$ showed no adsorption of Transferrin from pH 5 to pH 9, the zwitterionic polymer coated NPs exhibited excellent anti-adsorption ability.

Despite the positive charge of QDs@PMA-$DDA_{0.5}$-$DMAPA_{0.5}$ and QDs@PMA-$DDA_{0.25}$-$DMAPA_{0.75}$ in the pH range of 5 to 9, no significant adsorption of Transferrin was observed. This lack of adsorption may be due to insufficient electrostatic attraction to effectively engage the negatively charged regions of Transferrin. Additionally, the complex structure of Transferrin may limit the availability of suitable binding sites on the surfaces of these NPs.

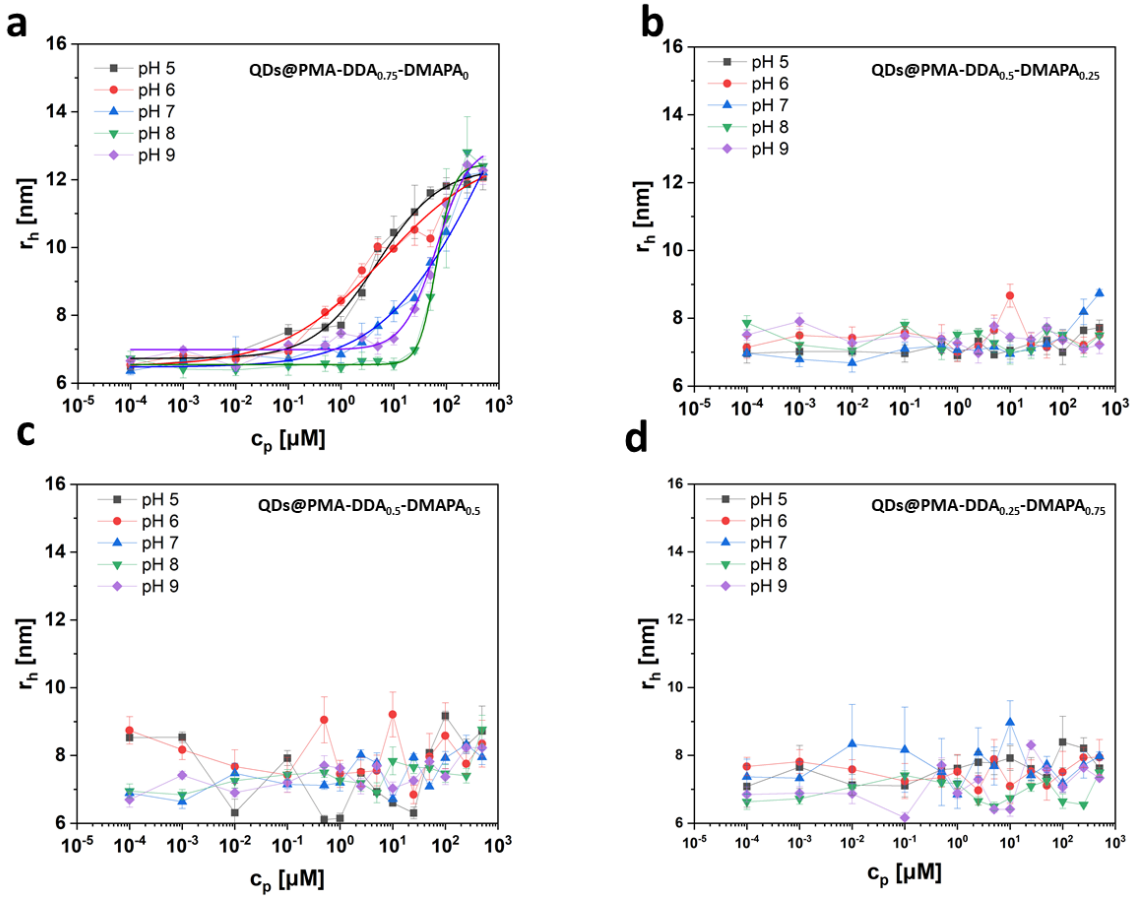

Figure 6-5. Radius(r_h)-Concentration(c_p) curve of a) QDs@PMA-DDA$_{0.75}$-DMAPA$_0$, b) QDs@PMA-DDA$_{0.5}$-DMAPA$_{0.25}$, c) QDs@PMA-DDA$_{0.5}$-DMAPA$_{0.5}$ and d) QDs@PMA-DDA$_{0.25}$-DMAPA$_{0.75}$ of Transferrin adsorption. The lines present the fitting by Hill function.

Table 6-6. Analyzing of FCS data of BSA adsorption on QDs@PMA-DDA$_{0.75}$-DMAPA$_0$, QDs@PMA-DDA$_{0.5}$-DMAPA$_{0.25}$, QDs@PMA-DDA$_{0.5}$-DMAPA$_{0.5}$ and QDs@PMA-DDA$_{0.25}$-DMAPA$_{0.75}$. R_0 stands for the original radius of the NPs, k_d indicates the protein concentration at half saturation stage, n is the Hill coefficient, N_{max} represents the maximum number of proteins that can adsorb onto a single NP, and ΔR_h is the difference between the radius at maximum adsorption and the NP's original radius.

NPs	pH	R_0 [nm]	K_d [μM]	n	N_{max}	ΔR_h [nm]
QDs@PMA-DDA$_{0.75}$-DMAPA$_0$	5	6.93	5.36	0.73	45.16	5.34
	6	6.55	25.41	0.39	59.84	5.65
	7	6.82	53.27	0.91	51.44	5.74
	8	6.52	43.30	2.24	47.84	5.85

	9	7.07	34.46	1.75	47.50	5.28
QDs@PMA-$DDA_{0.5}$-$DMAPA_{0.25}$	5	6.97	---	---	---	---
	6	7.14	---	---	---	---
	7	6.97	---	---	---	---
	8	7.87	---	---	---	---
	9	7.51	---	---	---	---
QDs@PMA-$DDA_{0.5}$-$DMAPA_{0.5}$	5	8.53	---	---	---	---
	6	8.74	---	---	---	---
	7	6.89	---	---	---	---
	8	6.95	---	---	---	---
	9	6.70	---	---	---	---
QDs@PMA-$DDA_{0.25}$-$DMAPA_{0.75}$	5	7.08	---	---	---	---
	6	7.67	---	---	---	---
	7	7.37	---	---	---	---
	8	6.63	---	---	---	---
	9	6.85	---	---	---	---

The Transferrin adsorption study on biotin and PEG modified NPs by FCS are recorded in Figure 6-6, and the data is further analyzed by Hill function, the calculated parameters are in Table 6-7.

After surface modification with biotin, QDs@PMA-$DDA_{0.75}$-$DMAPA_0$-biotin NPs showed different adsorption behaviors toward transferrin from QDs@PMA-$DDA_{0.75}$-$DMAPA_0$ NPs. The Kd values indicated that the nanoparticles had a moderate affinity for transferrin at all pH levels. The slightly lower Kd values at pH 5 and pH 6 indicated that the binding of NPs to transferrin was slightly stronger under acidic conditions and the binding remained relatively stable with increasing pH. At pH 5 and pH 6, the n values were less than 1, indicating that the adsorption process may proceed in a non-cooperative manner, possibly limited by the availability of binding sites. However, the n values at pH 7 (3.02) and pH 8 (4.61) increased significantly, indicating that the adsorption of transferrin shifted to a cooperative adsorption behavior under these pH conditions. This shift may be attributed to the conformational change or increased flexibility of transferrin. The n value at pH 9 decreased to 1.42, still reflecting some synergistic effects, although

weaker than those at pH 7 and 8. The stability of Nmax values from pH 5 to pH 9 indicates that the NPs maintain stable binding capacity for transferrin at slightly acidic to slightly alkaline pH. Surface modification with biotin significantly affects the adsorption behavior of transferrin. The presence of biotin increases the binding affinity and maximum adsorption capacity of transferrin, especially at lower pH. The observed shift in cooperative binding behavior between neutral and slightly alkaline conditions suggests that biotinylation promotes a more efficient interaction between transferrin and the NP surface. The stable adsorption of transferrin on QDs@PMA-$DDA_{0.75}$-$DMAPA_0$-biotin NPs may be due to the fact that biotin modification changes the effective surface charge of NPs, which can promote more favorable electrostatic interactions with transferrin. In addition, biotin modification may generate additional binding sites on the surface of NPs, thereby forming a spatial arrangement that enhances the attachment and interaction with multiple transferrin molecules, thereby promoting cooperative binding.

In contrast to QDs@PMA-$DDA_{0.75}$-$DMAPA_0$-biotin, the adsorption behavior of QDs@PMA-$DDA_{0.5}$-$DMAPA_{0.25}$-biotin NPs on Transferrin remained consistent with that of NPs without biotin modification. Additionally, no increase in particle size was observed across the pH range of 5 to 9. This indicates that the NPs retain their ability to resist Transferrin adsorption even with biotin modification on the surface.

QDs@PMA-$DDA_{0.75}$-$PEG_{0.25}$ exhibits effective anti-fouling properties, as no adsorption of Transferrin was observed under the experimental conditions.

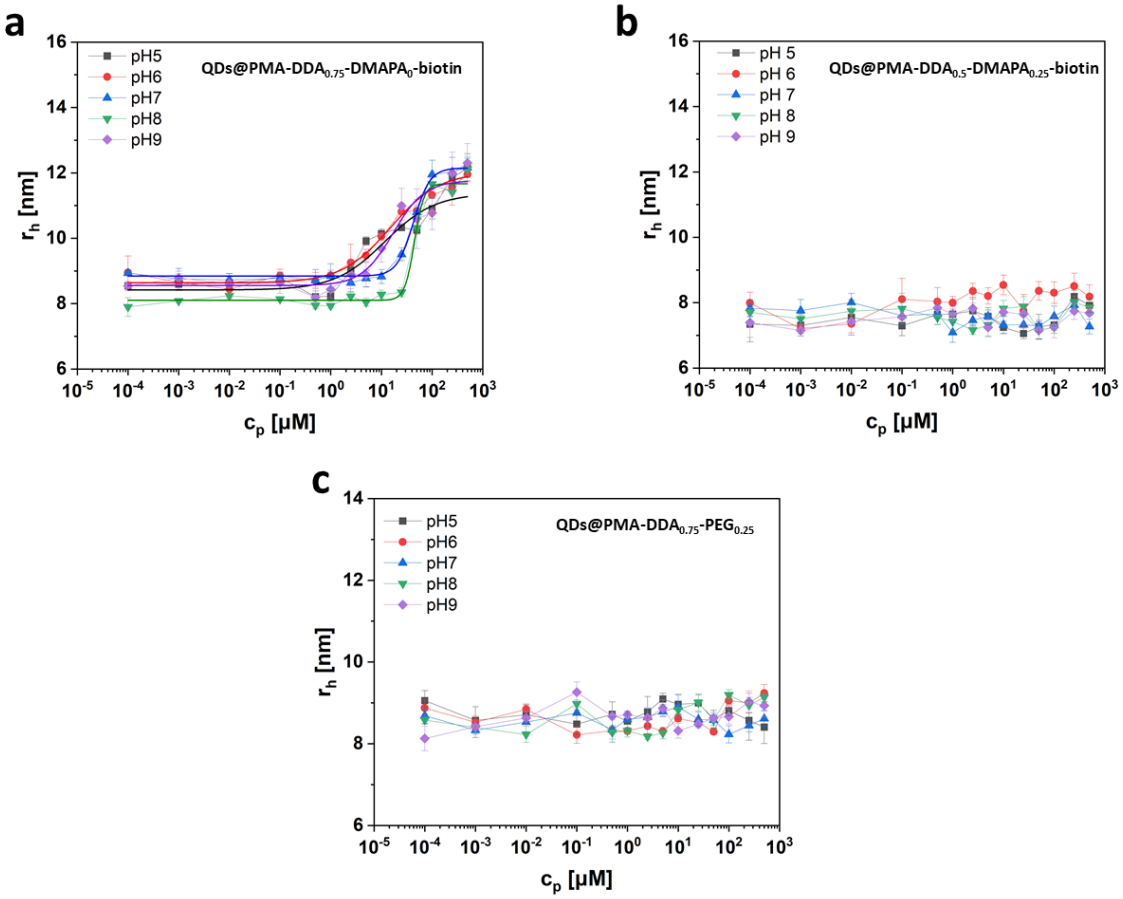

Figure 6-6. Radius(r_h)-Concentration(c_p) curve of a) QDs@PMA-DDA$_{0.75}$-DMAPA$_0$-biotin, b) QDs@PMA-DDA$_{0.5}$-DMAPA$_{0.25}$-biotin, and c) QDs@PMA-DDA$_{0.75}$-PEG$_{0.25}$ of Transferrin adsorption. The lines present the fitting by Hill function.

Table 6-7. Analyzing of FCS data of BSA adsorption on QDs@PMA-DDA$_{0.75}$-DMAPA$_0$-biotin, QDs@PMA-DDA$_{0.5}$-DMAPA$_{0.25}$-biotin and QDs@PMA-DDA$_{0.75}$-PEG$_{0.25}$. R_0 stands for the original radius of the NPs, k_d indicates the protein concentration at half saturation stage, n is the Hill coefficient, N_{max} represents the maximum number of proteins that can adsorb onto a single NP, and ΔR_h is the difference between the radius at maximum adsorption and the NP's original radius.

NPs	pH	R_0 [nm]	K_d [µM]	n	N_{max}	ΔR_h [nm]
QDs@PMA-DDA$_{0.75}$-DMAPA$_0$-biotin	5	8.42	15.67	0.90	24.92	3.75
	6	8.64	21.77	0.91	31.63	3.32
	7	8.84	44.46	3.02	31.61	3.32
	8	8.10	48.48	4.61	30.62	4.00

	9	8.55	21.29	1.42	29.01	3.76
QDs@PMA-$DDA_{0.5}$-$DMAPA_{0.25}$-biotin	5	7.34	---	---	---	---
	6	7.99	---	---	---	---
	7	7.83	---	---	---	---
	8	7.71	---	---	---	---
	9	7.39	---	---	---	---
QDs@PMA-$DDA_{0.75}$-$PEG_{0.25}$	5	9.06	---	---	---	---
	6	8.88	---	---	---	---
	7	8.69	---	---	---	---
	8	8.58	---	---	---	---
	9	8.23	---	---	---	---

Following the cap exchange on the surface, we studied Transferrin adsorption on QDs@MUA and QDs@PEG-COOH, the calculated radius of NPs is recorded in Figure 6-7, and the data was further fitted by Hill function, the parameters are shown in Table 6-8.

QDs@MUA is negatively charged at pH 5 to pH 9, and the adsorption behavior of transferrin is different under different pH conditions. The Kd value reflects the binding affinity of transferrin to QDs@MUA NPs at different pH. At pH 5, Kd is 1.09 μM, indicating a strong binding affinity between the negatively charged NPs and the positively charged regions of transferrin. As the pH increases to 6, Kd rises to 7.55 μM, indicating a decrease in binding strength, but still with strong affinity binding ability. At pH 7, Kd increases sharply to 221.32 μM, indicating a significant decrease in binding. This may be attributed to the neutralization of electrostatic interactions after the charges between the protein and NPs are balanced. At pH 9, Kd further increases to 4198.50 μM, reflecting a significant decrease in binding affinity. At these higher pH levels, conformational changes in the protein may also affect its stability and binding ability. The Hill coefficient n value reveals the mode of binding. At pH 5, the n value was 0.63, indicating non-cooperative binding, where the attachment of one transferrin molecule may reduce the possibility of binding of other molecules. At pH 6, the n value increased to 1.40, indicating a certain degree of cooperative binding, in which case, once one molecule binds, subsequent molecules will be more likely to bind, which may be due to conformational adjustments of the protein or NPs surface. However, at pH 7 and above, the n value decreased to 0.97 (pH 7), 0.93 (pH 8), and 0.43 (pH 9), indicating a decrease in cooperativity when protein molecules are adsorbed. The Nmax value showed fluctuations under different pH conditions. Interestingly, at pH 9, Nmax increased to 118.3, indicating a large binding potential

despite the high Kd value. This may mean that in an alkaline environment, more available binding sites are generated on the nanoparticle surface, allowing adsorption even with weak affinity to transferrin. FCS data showed that the adsorption of transferrin on QDs@MUA NPs was significantly affected by pH. The optimal binding occurred at lower pH levels, where strong electrostatic interactions existed between the negatively charged NPs and the positively charged transferrin regions. The binding affinity gradually decreased with increasing pH, which may be due to changes in charge balance and transferrin conformational stability.

During the Transferrin adsorption experiment on QDs@PEG-COOH, we observed no significant increase in particle size, indicating that QDs@PEG-COOH exhibits strong resistance to Transferrin adsorption.

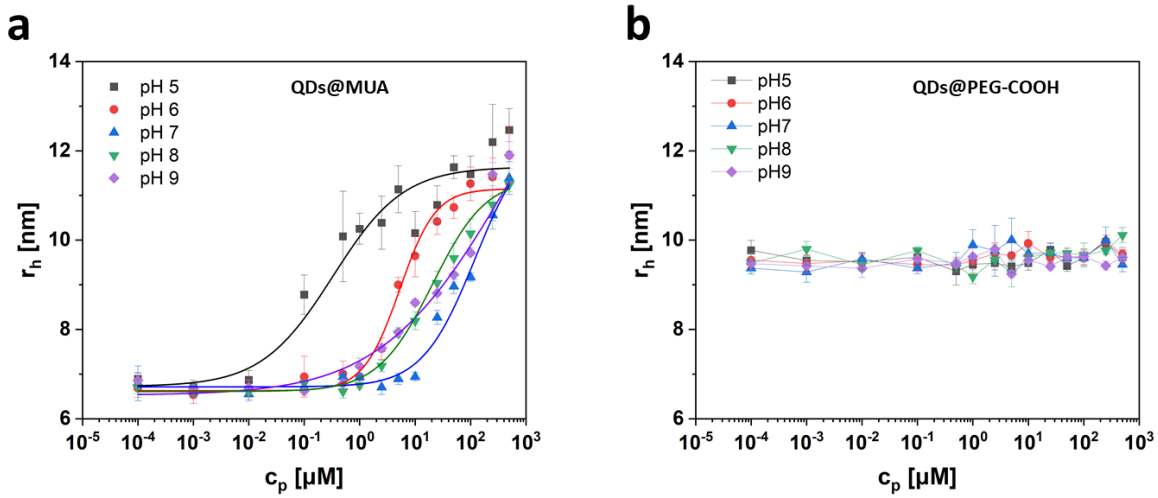

Figure 6-7. Radius(r_h)-Concentration(c_p) curve of a) QDs@MUA and b) QDs@PEG-COOH of Transferrin adsorption. The lines present the fitting by Hill function.

Table 6-8. Analyzing of FCS data of Transferrin adsorption on QDs@MUA and QDs@PEG-COOH. R_0 stands for the original radius of the NPs, k_d indicates the protein concentration at half saturation stage, n is the Hill coefficient, N_{max} represents the maximum number of proteins that can adsorb onto a single NP, and ΔR_h is the difference between the radius at maximum adsorption and the NP's original radius.

NPs	pH	R_0 [nm]	K_d [μM]	n	N_{max}	ΔR_h [nm]
QDs@MUA	5	6.71	1.09	0.63	38.70	5.74
	6	6.63	7.55	1.40	31.67	5.26
	7	6.71	221.32	0.97	49.90	4.67
	8	6.61	34.39	0.93	34.39	4.63

	9	6.52	4198.50	0.43	118.30	5.38
QDs@PEG-COOH	5	9.80	---	---	---	---
	6	9.55	---	---	---	---
	7	9.37	---	---	---	---
	8	9.49	---	---	---	---
	9	9.47	---	---	---	---

6.3.3 FCS measurements of pH-dependent pepsin adsorption on different nanoparticles

Pepsin is an acidic protein with a relatively low pI (pH 1.5 to 2). Table 6-7 shows the predicted change in total charge under experimental pH conditions. At pH 5, pepsin may still be active under acidic conditions and may have a slight positive charge because more of its ionizable groups remain protonated in the acidic environment. Starting at pH 6, pepsin may begin to shift toward a negative charge. At pH 8 and pH 9, pepsin becomes increasingly negatively charged because more of its acidic groups are deprotonated.

Table 6-9. Predicted charge of pepsin

Predicted charge (+/-)	pH 5	pH 6	pH 7	pH 8	pH 9
pepsin	+	-	-	-	-

The result of FCS measurements of pepsin adsorption on NPs with different surface charge is shown in Figure 6-8, and the data is further analyzed by Hill function in Table 6-10.

The adsorption of pepsin on the QDs@PMA-$DDA_{0.75}$-$DMAPA_0$ surface differs at different pH values. Although both pepsin and QDs@PMA-$DDA_{0.75}$-$DMAPA_0$ NPs are negatively charged and will form electrostatic repulsion, the surface of pepsin contains hydrophobic regions, which can bind well to the hydrophobic components of the polymer coating on the NPs. At pH 5 and 6, the k_d values are low, indicating that NPs have a strong binding affinity for pepsin. However, with the increase of pH, the k_d value rises sharply, reflecting that the binding affinity gradually weakens, and the affinity is the weakest at pH 9, which is 312.79 μM. At pH 5 and 9, the n values are low, indicating that the synergistic effect of binding is weak at this time, and relatively few pepsin molecules can be effectively bound. In contrast, at pH 6, 7, and 8, the n values increase significantly, indicating that there are more effective binding interactions and stronger synergistic

effects. The Nmax value stay stable under different pH conditions, but is the highest at pH 9, which indicates that although the binding affinity is weak at this condition, the probability of pepsin binding to the NPs molecules is higher, and pepsin may change to a conformation that enhances adsorption under these conditions, and the protein adsorption at this condition may not only by electrostatic interaction. The conformation of pepsin is sensitive to the change of pH conditions, at pH 7 or 8, pepsin may present another conformation that can assist the adsorption of free proteins after protein corona formation.

QDs@PMA-$DDA_{0.5}$-$DMAPA_{0.25}$ demonstrated strong anti-adsorption properties as zwitterionic NPs, with no significant pepsin adsorption observed during the experiment.

Although QDs@PMA-$DDA_{0.5}$-$DMAPA_{0.5}$ NPs and QDs@PMA-$DDA_{0.25}$-$DMAPA_{0.75}$ NPs are positively charged among the pH range of 5 to 9, there was no pepsin adsorption on the NPs detected. This may be due to the presence of a hydration layer surrounding the positively charged NPs, which creates a physical barrier that prevents pepsin molecules from accessing the surface. Additionally, the conformation of pepsin can influence its interaction with the NPs. While electrostatic interactions are important, the conformational stability of pepsin at different pH levels may result in its remaining in a non-adsorptive state when encountering positively charged surfaces. When negatively charged, pepsin may adopt a conformation that lowers its binding potential to the positively charged NPs, further contributing to the lack of adsorption.

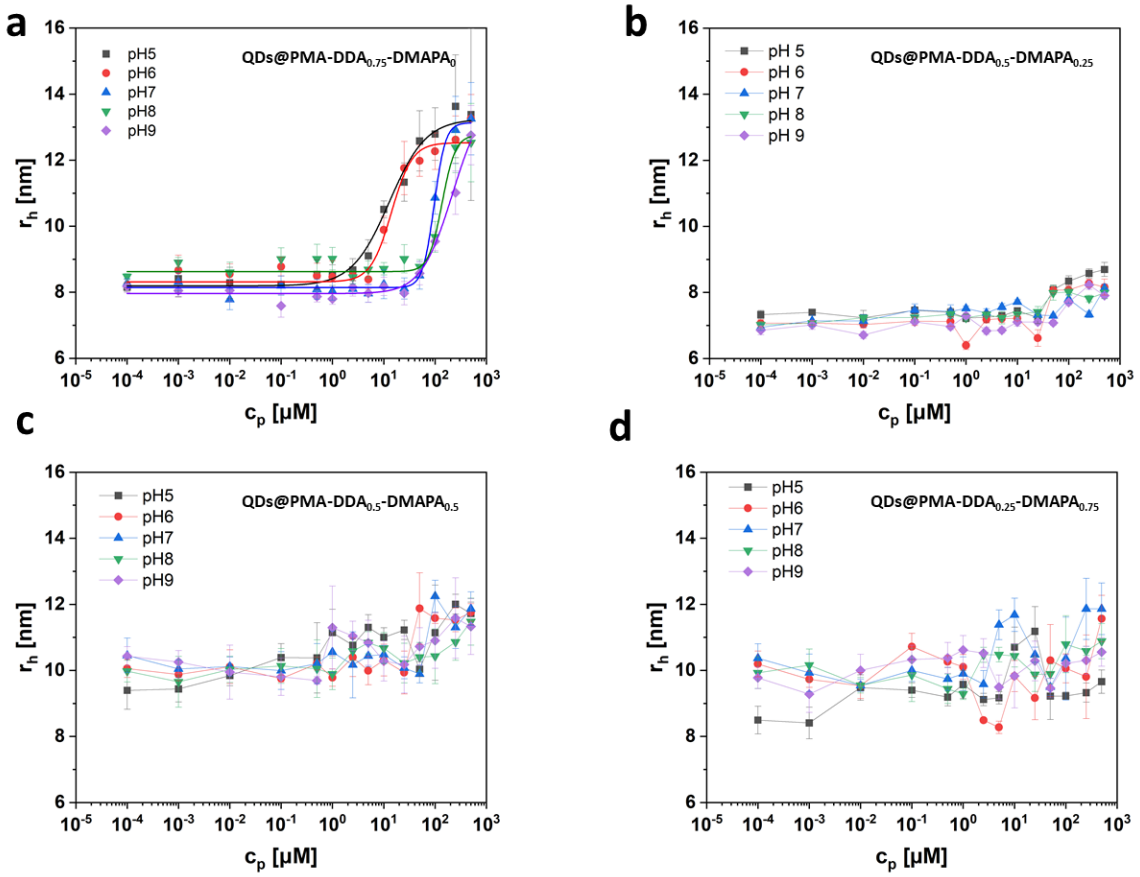

Figure 6-8. Radius(r_h)-Concentration(c_p) curve of a) QDs@PMA-DDA$_{0.75}$-DMAPA$_0$, b) QDs@PMA-DDA$_{0.5}$-DMAPA$_{0.25}$, c) QDs@PMA-DDA$_{0.5}$-DMAPA$_{0.5}$ and d) QDs@PMA-DDA$_{0.25}$-DMAPA$_{0.75}$ of pepsin adsorption. The lines present the fitting by Hill function.

Table 6-10. Analyzing of FCS data of BSA adsorption on QDs@PMA-DDA$_{0.75}$-DMAPA$_0$, QDs@PMA-DDA$_{0.5}$-DMAPA$_{0.25}$, QDs@PMA-DDA$_{0.5}$-DMAPA$_{0.5}$ and QDs@PMA-DDA$_{0.25}$-DMAPA$_{0.75}$. R_0 stands for the original radius of the NPs, k_d indicates the protein concentration at half saturation stage, n is the Hill coefficient, N_{max} represents the maximum number of proteins that can adsorb onto a single NP, and ΔR_h is the difference between the radius at maximum adsorption and the NP's original radius.

NPs	pH	R_0 [nm]	K_d [μM]	n	N_{max}	ΔR_h [nm]
QDs@PMA-DDA$_{0.75}$-DMAPA$_0$	5	8.19	18.53	1.25	49.84	5.09
	6	8.32	16.96	2.21	39.05	4.78
	7	8.14	107.36	4.04	48.44	5.15
	8	8.63	152.80	3.41	40.32	3.75

	9	7.96	312.79	1.50	62.53	4.80
QDs@PMA-$DDA_{0.5}$-$DMAPA_{0.25}$	5	7.33	---	---	---	---
	6	7.07	---	---	---	---
	7	6.94	---	---	---	---
	8	7.02	---	---	---	---
	9	6.86	---	---	---	---
QDs@PMA-$DDA_{0.5}$-$DMAPA_{0.5}$	5	9.40	---	---	---	---
	6	10.06	---	---	---	---
	7	10.45	---	---	---	---
	8	9.98	---	---	---	---
	9	10.23	---	---	---	---
QDs@PMA-$DDA_{0.25}$-$DMAPA_{0.75}$	5	9.50	---	---	---	---
	6	10.19	---	---	---	---
	7	10.37	---	---	---	---
	8	9.93	---	---	---	---
	9	9.77	---	---	---	---

We further conducted FCS measurements of pepsin adsorption on biotin or PEG modified NPs, the radius change is shown in Figure 6-9, and the data is further analyzed by Hill function in Table 6-11.

In the measurement of QDs@PMA-$DDA_{0.75}$-$DMAPA_0$-biotin, from the collected data we observed that the affinity for pepsin was the highest at pH 5, indicating that the adsorption conditions in an acidic environment are the most favorable. At lower pH levels, pepsin may exhibit positive surface charge characteristics, and the reduction of negative charges is conducive to favorable electrostatic interactions. The K_d value increased significantly from pH 5 onwards, indicating that the adsorption affinity gradually decreased, followed by a slight recovery at pH 9. It is worth noting that the highest n value was recorded at pH 9, indicating that despite the decrease in binding affinity, pepsin was more efficiently adsorbed at this pH condition. The large increase in Nmax from pH 5 to pH 8 may be due to the fact that the binding of pepsin destroys the stability of NPs, making it difficult to reach the state of adsorption saturation, but forming a loose multilayer adsorption structure. However, when the pH value is 9, there is a sharp decrease in Nmax,

which may be due to the denaturation of pepsin caused by the alkaline environment, and the change in conformation makes it unable to effectively bind to the surface of the NPs. The affinity of QDs@PMA-DDA$_{0.75}$-DMAPA$_0$-biotin NPs to pepsin is lower than that of QDs@PMA-DDA$_{0.75}$-DMAPA$_0$, which may be because the surface biotin modification increases the steric hindrance, thereby reducing its adsorption to pepsin.

QDs@PMA-DDA$_{0.5}$-DMAPA$_{0.25}$-biotin demonstrated strong anti-adsorption properties as zwitterionic NPs, with no significant pepsin adsorption observed during the experiment. Similarly, QDs@PMA-DDA$_{0.75}$-PEG$_{0.25}$ also exhibited resistance to pepsin adsorption, and there was no notable change in particle size under the experimental conditions.

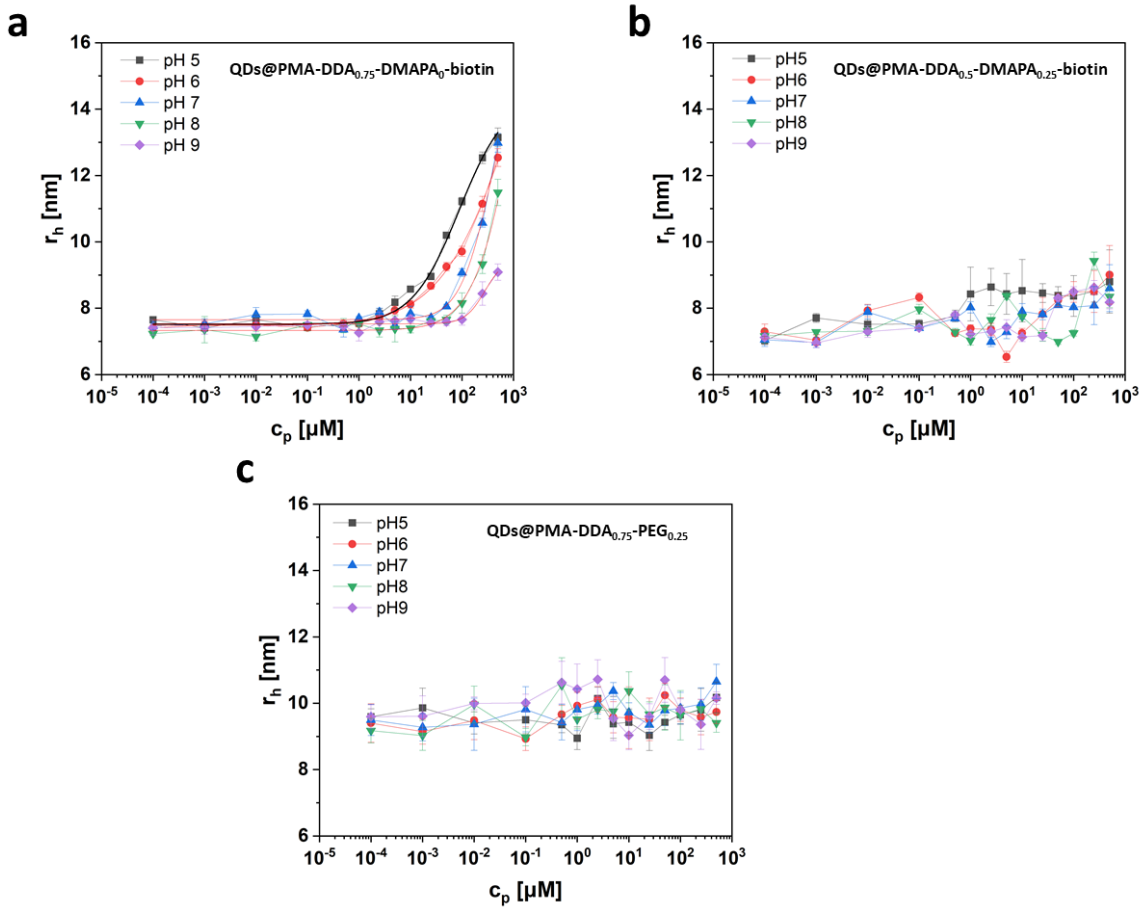

Figure 6-9. Radius(r_h)-Concentration(c_p) curve of a) QDs@PMA-DDA$_{0.75}$-DMAPA$_0$-biotin, b) QDs@PMA-DDA$_{0.5}$-DMAPA$_{0.25}$-biotin, and c) QDs@PMA-DDA$_{0.75}$-PEG$_{0.25}$ of pepsin adsorption. The lines present the fitting by Hill function.

Table 6-11. Analyzing of FCS data of pepsin adsorption on QDs@PMA-DDA$_{0.75}$-DMAPA$_0$-biotin, QDs@PMA-DDA$_{0.5}$-DMAPA$_{0.25}$-biotin and QDs@PMA-DDA$_{0.75}$-PEG$_{0.25}$. R_0 stands for

the original radius of the NPs, k_d indicates the protein concentration at half saturation stage, n is the Hill coefficient, N_{max} represents the maximum number of proteins that can adsorb onto a single NP, and ΔR_h is the difference between the radius at maximum adsorption and the NP's original radius.

NPs	pH	R_0 [nm]	K_d [μM]	n	N_{max}	ΔR_h [nm]
QDs@PMA-$DDA_{0.75}$-$DMAPA_0$-biotin	5	7.51	222.50	0.95	81.14	5.63
	6	7.48	7210.82	0.69	307.80	5.06
	7	7.65	629.77	1.53	112.78	5.33
	8	7.33	251005.74	1.17	42225.92	4.16
	9	7.53	309.87	2.27	12.21	1.56
QDs@PMA-$DDA_{0.5}$-$DMAPA_{0.25}$-biotin	5	7.02	---	---	---	---
	6	7.30	---	---	---	---
	7	7.05	---	---	---	---
	8	7.16	---	---	---	---
	9	7.12	---	---	---	---
QDs@PMA-$DDA_{0.75}$-$PEG_{0.25}$	5	9.59	---	---	---	---
	6	9.40	---	---	---	---
	7	9.50	---	---	---	---
	8	9.17	---	---	---	---
	9	9.59	---	---	---	---

The FCS measurements of pepsin adsorption on cap exchanged NPs are shown in Figure 6-10, and the data is further analyzed by Hill function in Table 6-12.

QDs@MUA NPs exhibited varying degrees of pepsin adsorption across the pH range of 5 to 9. The dissociation constant K_d increased with rising pH, indicating that the NPs demonstrated higher affinity for pepsin under acidic conditions (pH 5 and pH 6). As the pH increased, the negative charge on the pepsin surface also increased, leading to dominant electrostatic repulsion, which gradually reduced the binding interaction between the nanoparticles and pepsin. At pH levels 5, 6, 7, and 9, the binding of QDs@MUA NPs to pepsin was essentially in a non-synergistic state, while a weakly synergistic state was observed at pH 8, where the pepsin adsorbed onto the NPs surface facilitated further adsorption of additional pepsin from the solution. Notably, the

maximum amount of pepsin adsorbed onto the surface of QDs@MUA NPs increased with rising pH, despite the diminished binding strength. This observation suggests that pepsin is not tightly bound to the surface of QDs@MUA NPs, instead, it forms a loose protein corona, which facilitates the continued adsorption of additional pepsin.

The QDs@PEG-COOH did not exhibit significant particle size growth during the experiment, suggesting that pepsin did not adsorb onto the nanoparticles within the pH range of 5 to 9.

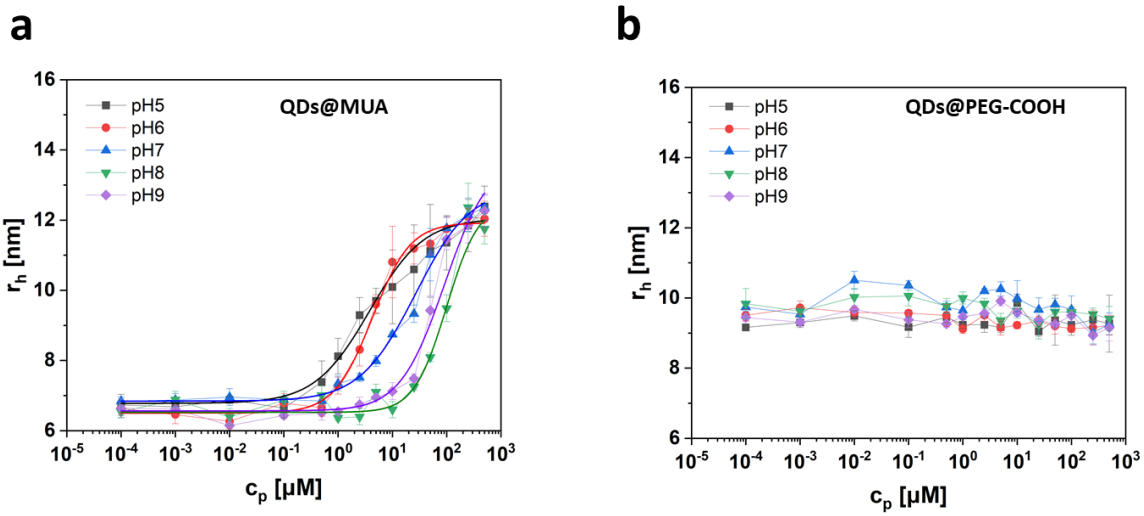

Figure 6-10. Radius(r_h)-Concentration(c_p) curve of a) QDs@MUA and b) QDs@PEG-COOH of pepsin adsorption. The lines present the fitting by Hill function.

Table 6-12. Analyzing of FCS data of pepsin adsorption on QDs@MUA and QDs@PEG-COOH. R_0 stands for the original radius of the NPs, k_d indicates the protein concentration at half saturation stage, n is the Hill coefficient, N_{max} represents the maximum number of proteins that can adsorb onto a single NP, and ΔR_h is the difference between the radius at maximum adsorption and the NP's original radius.

NPs	pH	R_0 [nm]	K_d [μM]	n	N_{max}	ΔR_h [nm]
QDs@MUA	5	6.78	7.03	0.91	40.33	5.61
	6	6.50	8.04	1.20	40.66	5.53
	7	6.85	48.06	0.95	50.31	5.51
	8	6.52	148.12	1.55	46.92	5.23
	9	6.82	68.25	2.50	43.75	5.69
	5	9.16	---	---	---	---

QDs@PEG-COOH	6	9.51	---	---	---	---
	7	9.74	---	---	---	---
	8	9.83	---	---	---	---
	9	9.44	---	---	---	---

6.3.4 FCS measurements of pH-dependent Lysozyme adsorption on different nanoparticles

Lysozyme is an alkaline protein with a high pI (pH 11). Table 6-8 shows the predicted total charge change under the experimental pH conditions. Under our experimental conditions (pH 5-pH 9), the pH value is always lower than the pI of lysozyme, so its acidic amino acid residues are deprotonated in solution and become negatively charged.

Table 6-13. Predicted charge of Lysozyme

Predicted charge (+/-)	pH 5	pH 6	pH 7	pH 8	pH 9
Lysozyme	+	+	+	+	+

The Lysozyme adsorption on QDs@PMA-DDA$_{0.75}$-DMAPA$_0$, QDs@PMA-DDA$_{0.5}$-DMAPA$_{0.25}$, QDs@PMA-DDA$_{0.5}$-DMAPA$_{0.5}$ and QDs@PMA-DDA$_{0.25}$-DMAPA$_{0.75}$ are shown in Figure 6-11. As a negatively charged NPs, Lysozyme exhibited strong adsorption onto the surface of QDs@PMA-DDA$_{0.75}$-DMAPA$_0$. When the concentration of Lysozyme reached 1 μM, significant fluctuations in the FCS reading were observed, making it impossible to calculate the size from diffusion coefficient, and also the solution turned opalescence and turbidity. This phenomenon suggests that Lysozyme adsorption compromised the stability of the NPs, leading to their aggregation. The adsorption of Lysozyme reduced the negative charge on the surface of QDs@PMA-DDA$_{0.75}$-DMAPA$_0$, thereby decreasing the repulsive forces between the NPs and further contributing to their aggregation.

QDs@PMA-DDA$_{0.5}$-DMAPA$_{0.25}$ demonstrates excellent anti-adsorption properties in the presence of Lysozyme. Over a concentration range of 0.0001 μM to 500 μM, only fluctuations in NPs radius were observed, with no significant protein adsorption detected.

Despite both QDs@PMA-$DDA_{0.5}$-$DMAPA_{0.5}$ and QDs@PMA-$DDA_{0.25}$-$DMAPA_{0.75}$ being positively charged nanoparticles, they exhibit distinct differences in their adsorption behavior with Lysozyme. The surface electrostatic charge of QDs@PMA-$DDA_{0.5}$-$DMAPA_{0.5}$ is relatively low. Although Lysozyme is also positively charged and should theoretically repel the NPs, FCS measurements showed significant fluctuations in NPs size. This does not indicate protein adsorption on the NPs surface, but suggests that Lysozyme disrupts the stability of the NPs.

QDs@PMA-$DDA_{0.25}$-$DMAPA_{0.75}$ retains a positive surface charge within the pH range of 5 to 9, effectively resisting the adsorption of Lysozyme on its surface. Consequently, no increase in NPs size was observed.

The adsorption behavior of Lysozyme varies significantly across NPs with different surface charges. The interaction with negatively charged QDs@PMA-$DDA_{0.75}$-$DMAPA_0$ is particularly strong, resulting in NPs aggregation. In contrast, no adsorption occurs on the surfaces of zwitterionic polymers or positively charged NPs.

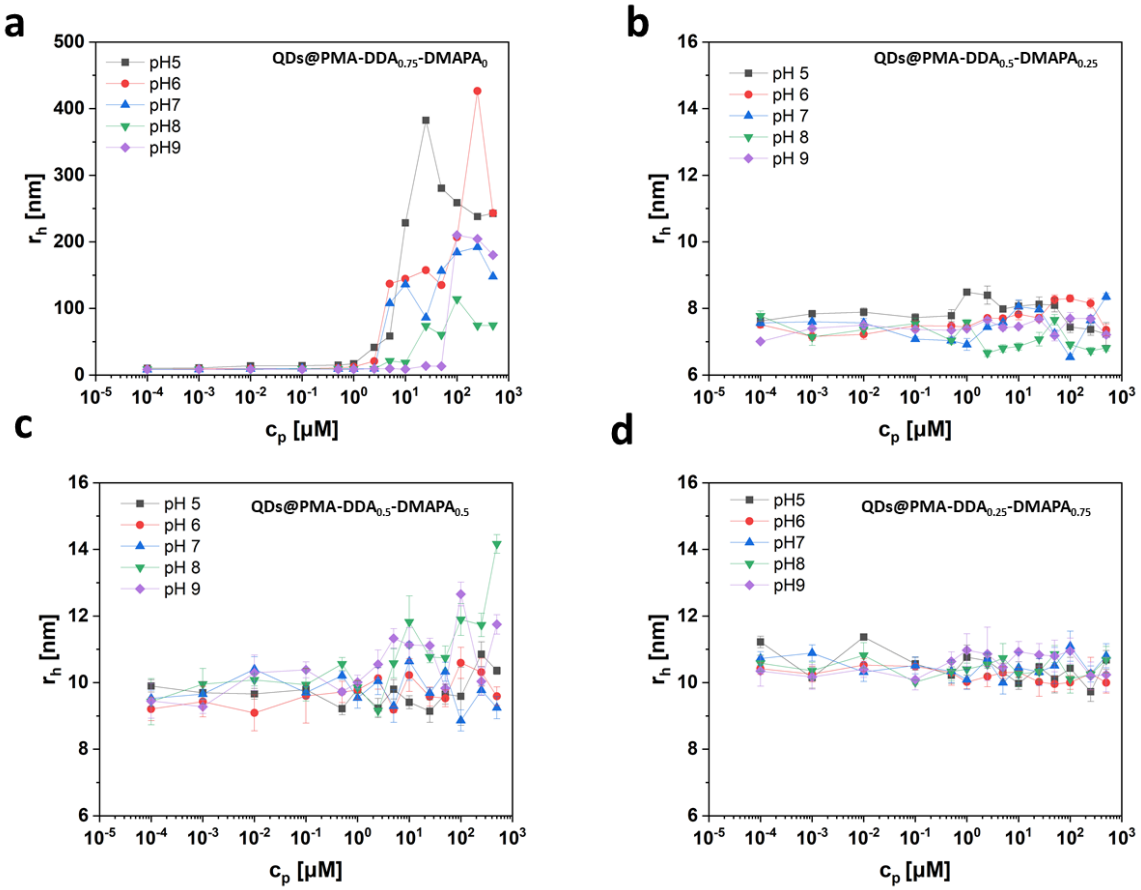

Figure 6-11. Radius(r_h)-Concentration(c_p) curve of a) QDs@PMA-DDA$_{0.75}$-DMAPA$_0$, b) QDs@PMA-DDA$_{0.5}$-DMAPA$_{0.25}$, c) QDs@PMA-DDA$_{0.5}$-DMAPA$_{0.5}$, d) QDs@PMA-DDA$_{0.25}$-DMAPA$_{0.75}$ of Lysozyme adsorption.

The Lysozyme adsorption on QDs@PMA-DDA$_{0.75}$-DMAPA$_0$-biotin, QDs@PMA-DDA$_{0.5}$-DMAPA$_{0.25}$-biotin and QDs@PMA-DDA$_{0.75}$-PEG$_{0.25}$ are shown in Figure 6-12. After the surface modification with biotin, the QDs@PMA-DDA$_{0.75}$-DMAPA$_0$-biotin NPs maintain a strong negative charge. However, the adsorption behavior of lysozyme onto these NPs differs significantly from that of QDs@PMA-DDA$_{0.75}$-DMAPA$_0$. At low lysozyme concentrations, a gradual increase in the NPs' radius is observed, indicating lysozyme adsorption. When the lysozyme concentration exceeds 100 μM, a marked increase in the NPs' radius occurs, particularly at pH 9. For instance, at 500 μM lysozyme concentration, the radius of the NPs can reach as high as 900 nm. This suggests that the adsorption of lysozyme onto QDs@PMA-DDA$_{0.75}$-DMAPA$_0$-biotin is weaker compared to QDs@PMA-DDA$_{0.75}$-DMAPA$_0$, indicating that the biotin modification partially neutralizes the negative charge. In medium to low lysozyme concentration solutions, a protein corona forms on the surface of the QDs@PMA-DDA$_{0.75}$-DMAPA$_0$-biotin NPs without causing NPs aggregation.

Despite the grafting of biotin onto the surface of QDs@PMA-DDA$_{0.5}$-DMAPA$_{0.25}$-biotin NPs, they retained the excellent anti-protein adsorption properties characteristic of zwitterionic NPs, with no lysozyme adsorption observed under pH 5 to pH 9.

For QDs@PMA-DDA$_{0.75}$-PEG$_{0.25}$ NPs, the theoretical expectation is that PEG modification would confer resistance to lysozyme adsorption. Although we did not observe any increase in NPs size during the experiments, the FCS readings showed considerable fluctuations. This may be attributed to the fact that, despite PEG grafting, QDs@PMA-DDA$_{0.75}$-PEG$_{0.25}$ remains negatively charged. Consequently, the positively charged lysozyme is attracted to the NPs due to electrostatic interactions. However, steric hindrance and the presence of a hydration layer from PEG prevent lysozyme from adsorbing onto the NPs surface, ultimately decreased NPs stability which turned into observed size fluctuations.

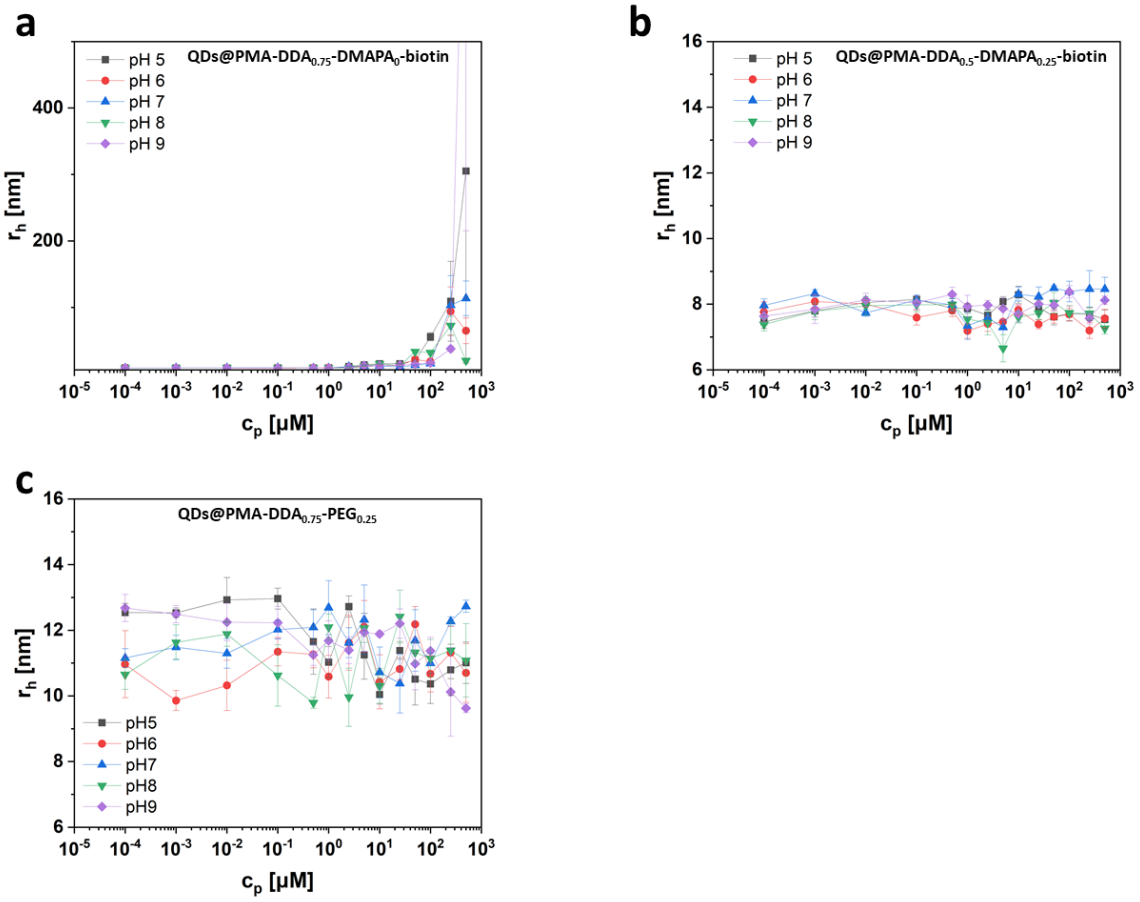

Figure 6-12. Radius(r_h)-Concentration(c_p) curve of a) QDs@PMA-DDA$_{0.75}$-DMAPA$_0$-biotin, b) QDs@PMA-DDA$_{0.5}$-DMAPA$_{0.25}$-biotin, c) QDs@PMA-DDA$_{0.75}$-PEG$_{0.25}$ of Lysozyme adsorption.

In the last NPs system, we studied the adsorption of lysozyme onto cap exchanged QDs NPs, the results are shown in Figure 6-13. After mixing the QDs@MUA NPs with lysozyme, starting at a concentration of 1 µM, we observed a significant increase in particle size. Subsequent measurements of the diffusion coefficient exceeded the normal reading range, complicating the calculation of the NPs radius and indicating particle aggregation. The negatively charged QDs@MUA NPs exhibited strong interactions with lysozyme under varying pH conditions. Notably, although the surface electrostatic charge of QDs@MUA is lower compared to QDs@PMA-DDA$_{0.75}$-DMAPA$_0$, aggregation occurred at a lower lysozyme concentration. This phenomenon may be attributed to the smaller steric hindrance on the surface of QDs@MUA NPs, which facilitates easier adsorption of proteins. This enhanced adsorption likely leads to increased protein accumulation and, ultimately, NPs aggregation.

For the QDs@PEG-COOH NPs, consistent with previous studies, no adsorption of lysozyme was observed across various concentrations and pH conditions. Additionally, the particle size remained relatively stable, indicating that these NPs possess good colloidal stability.

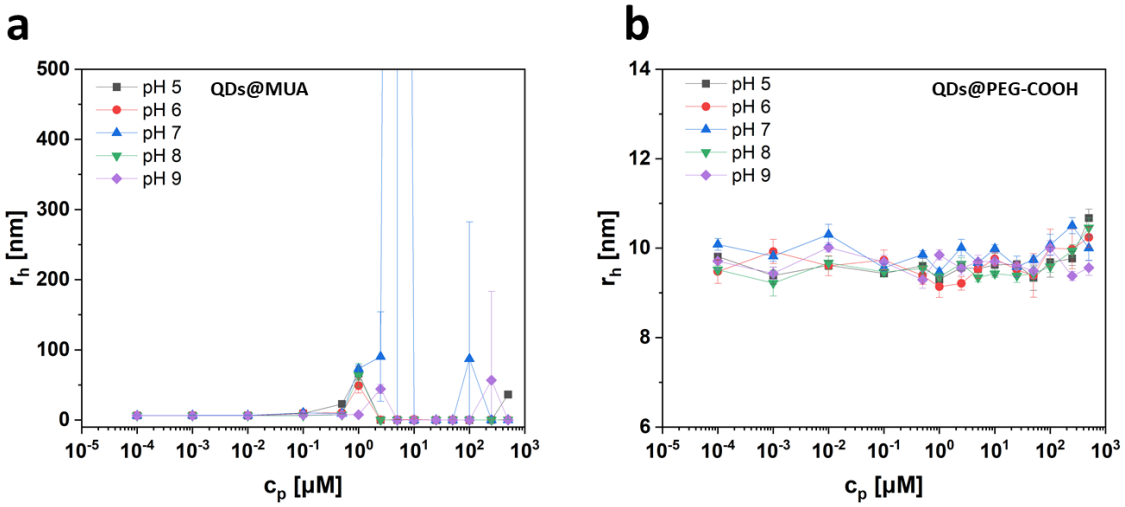

Figure 6-13. Radius(r_h)-Concentration(c_p) curve of a) QDs@MUA, b) QDs@PEG-COOH of Lysozyme adsorption.

By examining the adsorption behavior of lysozyme on NPs with various surface modifications, we found that NPs with a more negative surface charge strongly interact with lysozyme, leading to NPs aggregation upon adsorption. Among them, polymer-coated NPs exhibit significant steric hindrance, resulting in aggregation only at high lysozyme concentrations.

For NPs with a positive surface charge, electrostatic repulsion prevents lysozyme adsorption. However, lysozyme may compromise the colloidal stability of these NPs in solution.

Notably, PEG-modified and zwitterionic polymer NPs demonstrate excellent resistance to protein adsorption, as lysozyme does not adsorb to their surfaces.

6.3.5 FCS measurements of Avidin adsorption on different nanoparticles at pH 7

In the study of Avidin adsorption, we only focused on its specific adsorption performance, so we only studied it under pH 7. Avidin is similar to Lysozyme, with a high pl (pH 11). Avidin would exhibit a positive charge at pH 7.

The avidin-biotin interaction is one of the strongest known non-covalent interactions, with a dissociation constant (Kd) in the picomolar range (approximately 10^-15 M). This high affinity makes the complex extremely stable. Therefore, we chose a very low Avidin concentration (0.1 nM to 1000 nM) for protein adsorption experiments, as in previous experiments, protein adsorption was usually not observed in this concentration range.

We initially performed an adsorption experiment of Avidin on nanoparticles with varying surface charge properties. The radius(r_h)-concentration(c_p) curve of Avidin adsorption is shown in Figure 6-14, and the corresponding Hill fitting results are shown in the Table 6-14.

Since the concentration of Avidin was in a relatively lower range, when we incubate Avidin with QDs@PMA-$DDA_{0.5}$-$DMAPA_{0.25}$, QDs@PMA-$DDA_{0.5}$-$DMAPA_{0.5}$, QDs@PMA-$DDA_{0.25}$-$DMAPA_{0.75}$, there is no adsorption happened, as the radius of NPs only has slight fluctuations, but not significant increase, this may also due to the surface charge of QDs@PMA-$DDA_{0.5}$-$DMAPA_{0.25}$ remain neutral, QDs@PMA-$DDA_{0.5}$-$DMAPA_{0.5}$ and QDs@PMA-$DDA_{0.25}$-$DMAPA_{0.75}$ are positively charged, in this case, positively charged Avidin has a repulsive force towards those NPs. However, the negatively charged QDs@PMA-$DDA_{0.75}$-$DMAPA_0$ showed increased adsorption with the increasing Avidin concentration, even in the concentration lower than 1 µM, we can assume that this adsorption behavior is mainly driven by electrostatic interaction. From the parameters we got from Hill-fitting, the hill index n is 1.48, indicates a collaborative adsorption, and the radius increase is 1.87 nm, means the adsorption of Avidin only formed a single layer, at maximum there will be about 15 Avidin adsorbed on the surface of QDs@PMA-$DDA_{0.75}$-$DMAPA_0$.

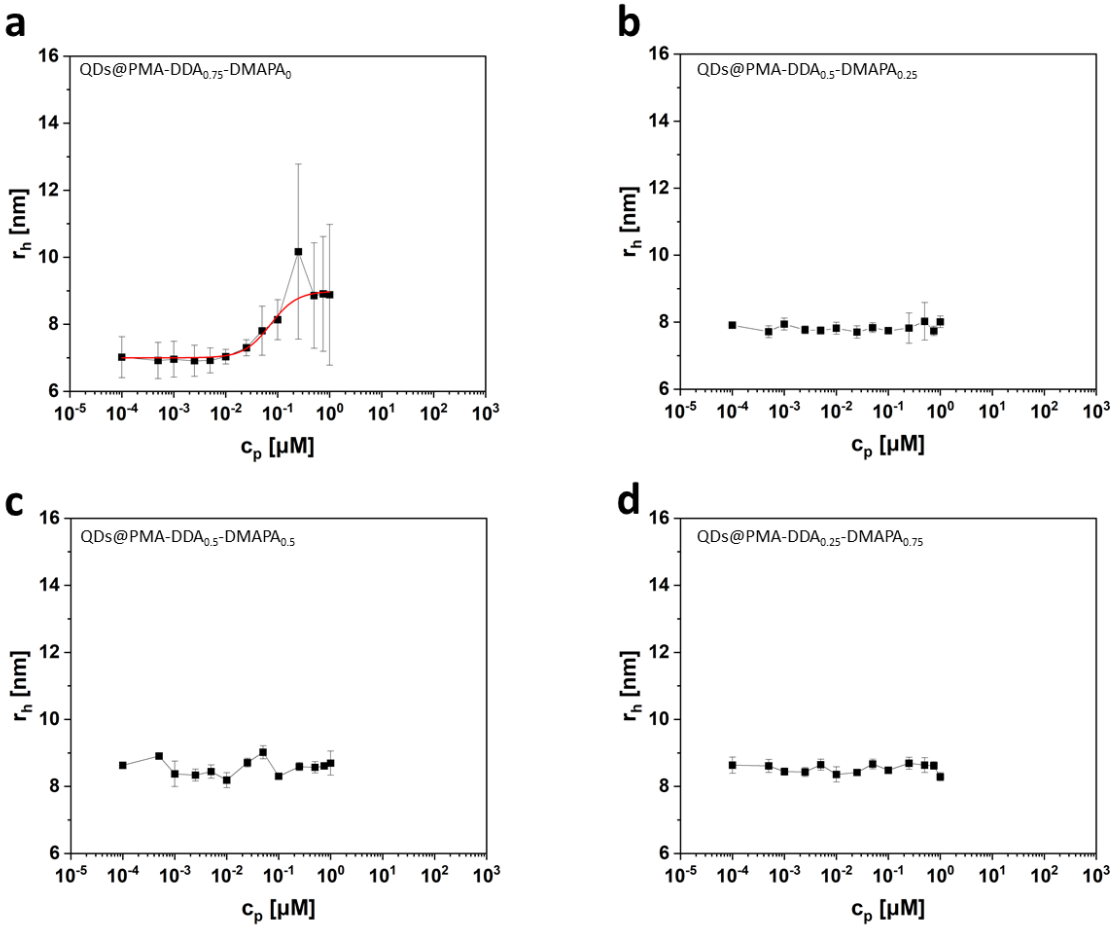

Figure 6-14. Radius(r_h)-Concentration(c_p) curve of a) QDs@PMA-DDA$_{0.75}$-DMAPA$_0$, b) QDs@PMA-DDA$_{0.5}$-DMAPA$_{0.25}$, c) QDs@PMA-DDA$_{0.5}$-DMAPA$_{0.5}$, d) QDs@PMA-DDA$_{0.25}$-DMAPA$_{0.75}$ of Avidin adsorption. The red line presents the fitting by Hill function.

Table 6-14. Analyzing of FCS data of Avidin adsorption on QDs@PMA-DDA$_{0.75}$-DMAPA$_0$, QDs@PMA-DDA$_{0.5}$-DMAPA$_{0.25}$, QDs@PMA-DDA$_{0.5}$-DMAPA$_{0.5}$, and QDs@PMA-DDA$_{0.25}$-DMAPA$_{0.75}$. R_0 stands for the original radius of the NPs, k_d indicates the protein concentration at half saturation stage, n is the Hill coefficient, N_{max} represents the maximum number of proteins that can adsorb onto a single NP, and ΔR_h is the difference between the radius at maximum adsorption and the NP's original radius.

NPs	pH	R_0 [nm]	k_d [μM]	n	N_{max}	ΔR_h [nm]
QDs@PMA-DDA$_{0.75}$-DMAPA$_0$	7	6.92	0.09	1.48	15.19	1.87
QDs@PMA-DDA$_{0.5}$-DMAPA$_{0.25}$	7	7.86	---	---	---	---

QDs@PMA-$DDA_{0.5}$-$DMAPA_{0.5}$	7	8.56	---	---	---	---
QDs@PMA-$DDA_{0.25}$-$DMAPA_{0.75}$	7	8.60	---	---	---	---

The results indicate that the strong negative charge on the surface of QDs@PMA-$DDA_{0.75}$-$DMAPA_0$ NPs leads to non-specific adsorption of Avidin. This suggests that in a physiological environment, these strongly negatively charged nanoparticles are likely to bind with positively charged proteins, which may adversely affect their functionality. To mitigate this issue, we can consider using zwitterionic nanoparticles, whose neutral surfaces can reduce protein adsorption. Alternatively, we could employ positively charged nanoparticles that would generate electrostatic repulsion with similarly charged proteins, thereby minimizing surface adsorption.

Next, we carried out the Avidin adsorption experiment on the NPs modified with biotin or PEG on their surfaces. The radius(r_h)-concentration(c_p) curve of Avidin adsorption is shown in Figure 6-15, and the corresponding Hill fitting results are shown in the Table 6-15.

After biotinylating, the adsorption of Avidin became faster and stronger on QDs@PMA-$DDA_{0.75}$-$DMAPA_0$-biotin, as the k_d decreased to 0.01 μM, and a maximum of 64 Avidin can be adsorbed on the surface of the NPs, also the Hill coefficient n increased to 4.44, means a more collaborative adsorption, the adsorbed Avidin will increase the likelihood for further adsorption. And also, the change of radius is 2.27 nm, indicated a single layer adsorption. The same is single layer adsorption, but the size change is slightly different, which may be due to the different orientation and distribution of protein adsorption.

The QDs@PMA-$DDA_{0.5}$-$DMAPA_{0.25}$-biotin NPs also exhibited a strong affinity for Avidin, even though their surface charge remained nearly neutral, demonstrating an anti-adsorption ability. After modification with biotin—known for its strong adsorption capacity for Avidin, their ability to bind Avidin was restored, although the adsorption rate was lower than that of QDs@PMA-$DDA_{0.75}$-$DMAPA_0$-biotin. This was evidenced by a k_d value of 0.47 μM and an n value of 1.30, indicating collaborative adsorption for Avidin. The N_{max} value suggests that a maximum of 52 Avidin can be adsorbed onto one single NP, and the observed increase in NP size of 2.98 implies the potential for multi-layer adsorption.

The QDs@PMA-$DDA_{0.75}$-$PEG_{0.25}$ still maintained good anti-protein adsorption ability, especially at low Avidin concentration. PEG exhibits significant steric hindrance due to its flexible and elongated structure. When grafted onto the surface of the NPs, PEG forms a physical barrier that can hinder the access of Avidin molecules. This barrier effectively

prevents Avidin from reaching the NPs surface, thereby significantly reducing or completely eliminating adsorption. Furthermore, the hydrophilic nature of PEG may contribute to the reduction in Avidin adsorption. Although Avidin possesses hydrophobic regions that typically facilitate surface interactions, the PEG layer can create a hydrated shell around the NPs. This increased hydrophilicity may lead Avidin to preferentially remain in the aqueous phase rather than adsorbing onto the PEG-modified surface. Additionally, the modification of the surface with PEG may result in a decrease in negative charge. Since Avidin is a positively charged protein, this reduction in surface charge could diminish the electrostatic attraction between the protein and the NPs.

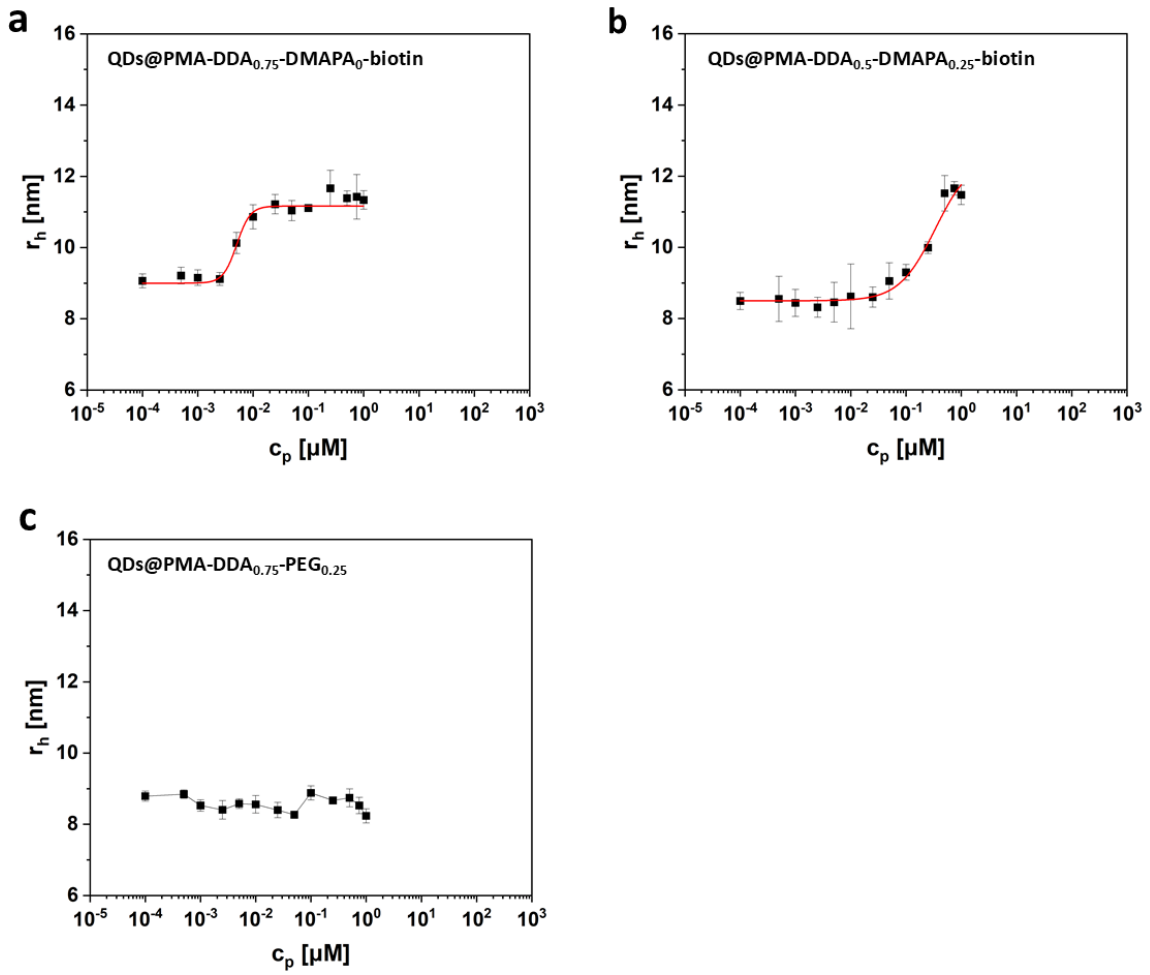

Figure 6-15. Radius(rh)-Concentration(cp) curve of a) QDs@PMA-DDA$_{0.75}$-DMAPA$_0$-biotin, b) QDs@PMA-DDA$_{0.5}$-DMAPA$_{0.25}$-biotin, c) QDs@PMA-DDA$_{0.75}$-PEG$_{0.25}$ of Avidin adsorption. The red line presents the fitting by Hill function.

Table 6-15. Analyzing of FCS data of Avidin adsorption on QDs@PMA-DDA$_{0.75}$-DMAPA$_0$-biotin, QDs@PMA-DDA$_{0.5}$-DMAPA$_{0.25}$-biotin and QDs@PMA-DDA$_{0.75}$-PEG$_{0.25}$. R_0 stands for

the original radius of the NPs, k_d indicates the protein concentration at half saturation stage, n is the Hill coefficient, N_{max} represents the maximum number of proteins that can adsorb onto a single NP, and ΔR_h is the difference between the radius at maximum adsorption and the NP's original radius.

NPs	pH	R_0 [nm]	k_d [μM]	n	N_{max}	ΔR_h [nm]
QDs@PMA-$DDA_{0.75}$-$DMAPA_0$-biotin	7	9.10	0.01	4.44	23.66	2.27
QDs@PMA-$DDA_{0.5}$-$DMAPA_{0.25}$-biotin	7	8.46	0.47	1.30	52.15	2.98
QDs@PMA-$DDA_{0.75}$-$PEG_{0.25}$	7	8.50	---	---	---	---

Through the study of NPs modified with biotin or PEG on their surfaces, we have observed that modifying negatively charged QDs@PMA-$DDA_{0.75}$-$DMAPA_0$ NPs with positively charged proteins that possess specific adsorption capabilities leads to faster and more intense protein adsorption. Additionally, NPs coated with zwitterionic polymers, such as QDs@PMA-$DDA_{0.5}$-$DMAPA_{0.25}$, regain their protein adsorption capacity after being modified with specifically adsorptive proteins. In contrast, NPs coated with PEG-grafted polymers can effectively maintain their anti-adsorption properties under any conditions.

Finally, we have studied the Avidin adsorption on the NPs after cap exchange. The radius(r_h)-concentration(c_p) curve of Avidin adsorption is shown in Figure 6-16, and the corresponding Hill fitting results are shown in the Table 6-16.

The amount of Avidin adsorbed on the surface of QDs@MUA increased significantly starting at a concentration of 0.1 μM, resulting in a rapid rise in the hydration radius of the NPs as the concentration increased. At an Avidin concentration of 1 μM, the hydration radius of the NPs reached approximately 60 nm. Analysis of the data using the Hill model revealed key parameters pertaining to the Avidin adsorption process. The low k_d value for QDs@MUA (0.26 μM) indicates that a substantial amount of Avidin can bind to the NPs even at relatively low concentrations. This strong binding is likely attributed to the significant negative charge present on the surface of QDs@MUA. At pH 7, Avidin remains positively charged, leading to strong electrostatic adsorption.

On a single QDs@MUA nanoparticle, up to approximately 6971 Avidin can bind to the surface, resulting in multilayer adsorption. However, its k_d is lower than that of QDs@PMA-$DDA_{0.75}$-$DMAPA_0$ due to a slightly reduced surface negative charge. The Hill

coefficient value of 5.14 suggests that multiple binding sites on the NPs surface can influence each other, resulting in a strong collective binding effect that promotes the synergistic binding of multiple Avidin molecules. The considerable size increase of QDs@MUA may also be attributed to its lower stability compared to polymer-coated NPs, and when Avidin's concentration increased, the nanoparticles began to aggregate. The polymer coatings can effectively prevent excessive protein adsorption due to significant steric hindrance.

In contrast, QDs@PEG-COOH NPs did not exhibit noticeable changes in particle size as the concentration of Avidin increased, thereby maintaining robust anti-adsorption properties.

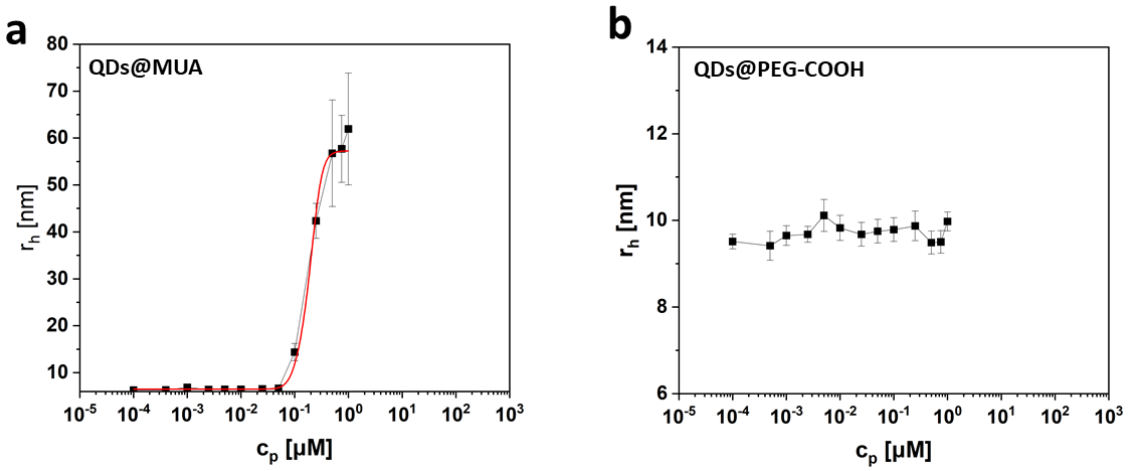

Figure 6-16. Radius(rh)-Concentration(cp) curve of a) QDs@MUA, b) QDs@PEG-COOH of Avidin adsorption. The red line presents the fitting by Hill function.

Table 6-16. Analyzing of FCS data of Avidin adsorption on QDs@MUA and QDs@PEG-COOH. R_0 stands for the original radius of the NPs, k_d indicates the protein concentration at half saturation stage, n is the Hill coefficient, N_{max} represents the maximum number of proteins that can adsorb onto a single NP, and ΔR_h is the difference between the radius at maximum adsorption and the NP's original radius.

NPs	pH	R_0 [nm]	K_D [µM]	n	N_{max}	ΔR_h [nm]
QDs@MUA	7	6.50	0.26	5.14	6971.69	55.40
QDs@PEG-COOH	7	9.50	---	---	---	---

Through our study of Avidin adsorption on these two NPs with direct cap exchange, we found that QDs@MUA NPs possess a substantial number of binding sites available for

Avidin occupancy. This characteristic is highly advantageous for applications requiring high capacity or strong affinity. In contrast, QDs@PEG-COOH NPs demonstrate inherent stability and exhibit excellent anti-adsorption properties.

7. Summary and Future Perspective

7.1 Summary

Conducting protein corona studies under varying pH conditions offers valuable insights into the pH-dependent aspects of protein-NPs interactions. By exploring how pH modulates protein adsorption, conformation, and interactions, researchers can enhance their understanding of NPs behavior and applications in biomedicine, nanotoxicology, and environmental science.

In our research, we conducted various surface modifications on QDs NPs, including encapsulation with polymers of varying surface charges, surface biotinylation, PEGylation, and direct cap exchange. We characterized the properties of the fabricated NPs systems and performed detailed protein adsorption experiments with individual proteins. This allowed us to comprehensively elucidate the mechanisms and factors influencing the formation of the protein corona.

In our first system, we synthesized amphiphilic polymers containing various proportions of DMAPA, which can be protonated in solution to impart a positive charge. When these amphiphilic polymers are applied to the surface of QDs, they facilitate a phase transition that enables the QDs to disperse in aqueous solutions. The varying proportions of DMAPA within the polymer alter the surface charge of the NPs. Notably, QDs@PMA-$DDA_{0.75}$-$DMAPA_0$ exhibits a significant negative surface charge across pH 5 to 9, with minimal variation in charge as pH changes. This characteristic leads to strong adsorption of biomolecules such as BSA, Transferrin, and pepsin, with consistent behavior observed across different pH conditions. In the case of Avidin, despite lacking specific adsorption sites on QDs@PMA-$DDA_{0.75}$-$DMAPA_0$, the pronounced negative charge facilitates the adsorption of a substantial amount of positively charged Avidin. Similarly, for positively charged Lysozyme, QDs@PMA-$DDA_{0.75}$-$DMAPA_0$ demonstrates strong adsorption affinity, which can even result in NPs aggregation at higher concentrations.

After the polymer grafted with DMAPA, the surface of the QDs@PMA-$DDA_{0.5}$-$DMAPA_{0.25}$ NPs exhibited both positive and negative charges. As a result, these zwitterionic NPs were predominantly electrically neutral, with a slight reduction in surface potential observed as the pH gradually increased. The hydration layer that forms on the surface of these zwitterionic NPs effectively resists the adsorption of proteins.

As the proportion of DMAPA in the polymer increases, the QDs@PMA-$DDA_{0.5}$-$DMAPA_{0.5}$ and QDs@PMA-$DDA_{0.25}$-$DMAPA_{0.75}$ NPs are positively charged in the pH range of 5 to 9, although the positive charge gradually weakens as the pH continues to increase. At the same time, as the proportion of DMAPA increases, the hydrophilicity of the NPs also decreases. Changes in surface positive charge and hydrophilicity will have a series of effects on subsequent protein adsorption. Contrary to expectations, QDs@PMA-$DDA_{0.5}$-

$DMAPA_{0.5}$ exhibited no adsorption capacity for proteins in this experiment. This may be attributed to insufficient surface charge on the NPs. The negative charge from the carboxyl groups on the PMA backbone, coupled with the positive charge of DMAPA when protonated, can create a hydration layer that hinders further protein adsorption.

Similarly, QDs@PMA-$DDA_{0.25}$-$DMAPA_{0.75}$ does not align with theoretical predictions. While it shows no affinity for negatively charged pepsin, it demonstrates a higher binding affinity for BSA. This observation indicates that during the formation of a protein corona, electrostatic effects are not necessarily dominant, instead, the structure and hydrophilicity of the protein also play a crucial role.

In our second NPs system, we modified the NPs surfaces through biotinylation and PEGylation. Surface biotinylation enhances the specific binding affinity of the NPs for Avidin, whereas PEGylation has been previously demonstrated to effectively reduce protein adsorption.

The negative charge of QDs@PMA-$DDA_{0.75}$-$DMAPA_0$-biotin and QDs@PMA-$DDA_{0.5}$-$DMAPA_{0.25}$-biotin NPs is partially neutralized compared to NPs without biotin. The adsorption behavior of QDs@PMA-$DDA_{0.75}$-$DMAPA_0$-biotin closely resembles that of QDs@PMA-$DDA_{0.75}$-$DMAPA_0$. However, the introduction of the biotin group enhances the affinity for certain proteins. This improvement is attributed to biotin's influence on the surface charge distribution and hydrophilicity of the NPs. QDs@PMA-$DDA_{0.5}$-$DMAPA_{0.25}$-biotin retains the anti-adsorption properties characteristic of zwitterionic NPs while still demonstrating a strong specific adsorption capacity for avidin. These findings offer valuable insights for the future design of specific adsorption nanomaterials, enabling the reduction of unwanted protein adsorption while preserving affinity for target proteins.

After grafting PEG into the polymer, the negative charge of QDs@PMA-$DDA_{0.75}$-$PEG_{0.25}$ was slightly reduced. However, the NPs continued to exhibit a negative charge within the pH range of 5 to 9. In subsequent experiments, we observed no adsorption of BSA, Transferrin, pepsin, or Avidin onto the NPs surfaces. This lack of adsorption can be attributed to the steric hindrance and hydration layer created by the PEG chains, which effectively prevents protein binding. Interestingly, when the NPs were mixed with Lysozyme, we detected a significant fluctuation in particle size. Nonetheless, this change in size did not suggest protein adsorption, likely due to the strong positive charge of Lysozyme disrupting the stability of the QDs@PMA-$DDA_{0.75}$-$PEG_{0.25}$ NPs.

In our last research system, we conducted a direct ligand exchange on the surface of QDs by replacing the oleylamine ligands with short-chain MUA and long-chain PEG-COOH. This modification enhanced the dispersion of the QDs in aqueous solutions. Unlike the polymer encapsulation method, ligand exchange allows for a faster and more efficient phase transition of hydrophobic QDs. QDs@MUA and QDs@PMA-$DDA_{0.75}$-$DMAPA_0$ exhibit similar adsorption properties, however, they generally demonstrate a higher affinity for proteins compared to polymer-coated NPs. This enhanced affinity may be

attributed to the surface ligands, which reduce steric hindrance and facilitate protein adsorption. When QDs@MUA NPs are mixed with lysozyme, which carries a strong positive charge, the NPs tend to aggregate at low concentrations. This behavior indicates that the stability of QDs@MUA is weaker than that of the polymer-coated NPs.

After the ligand exchange, QDs@PEG-COOH displayed a slight negative charge in solution, as the carboxyl groups at the end of the ligands exhibited minimal variation in surface potential within the pH range of 5 to 9. QDs@PEG-COOH demonstrated good hydrophilicity and maintained excellent colloidal stability across different pH conditions. The nearly neutral surface, combined with the anti-protein adsorption properties conferred by the PEG chains, resulted in no observed protein adsorption by QDs@PEG-COOH NPs in our study.

The experiments indicate that protein adsorption is not solely a result of electrostatic interactions. We should also take the pH environment, the hydrophilic and hydrophobic characteristics of the NPs, and their surface functional groups into account. Consequently, when designing NPs, it is essential to consider their intended applications comprehensively to either minimize the formation of a protein corona or to maximize the effective adsorption of the target protein.

7.2 Future Perspective

Utilizing fluorescence correlation spectroscopy (FCS) to analyze individual proteins adsorption and investigate protein corona formation on NPs with varying surface chemistries at different pH levels offers a comprehensive and multidimensional approach to understanding NPs-protein interactions.

By examining protein corona formation on NPs with diverse surface properties, we can gain insights into how factors such as surface charge, hydrophobicity, and functional groups influence protein adsorption and corona structure. Understanding these interactions is essential for designing NPs with tailored application.

Evaluating protein corona formation under varying pH conditions sheds light on the pH-dependent behavior of both proteins and NPs. FCS enables us to monitor changes in protein binding kinetics and affinity at different pH levels, enhancing our understanding of how pH affects corona assembly.

The findings from this study will offer valuable insights into how surface chemistry, pH, and protein composition impact protein corona formation and stability. These factors are crucial for predicting the biological response, cellular uptake, and potential toxicity of NPs in biomedical and environmental applications.

Our study employing FCS to explore the behavior of individual proteins in the protein corona provides a holistic view of NPs-protein interactions across various conditions. This multidimensional approach paves the way for a deeper understanding of protein corona dynamics and its implications for nanobiology and nanomedicine.

Bibliography

1. Chen, K.-J., et al., *Recent advances in prodrug-based nanoparticle therapeutics.* European Journal of Pharmaceutics and Biopharmaceutics, 2021. **165**: p. 219-243.
2. Heiligtag, F.J. and M. Niederberger, *The fascinating world of nanoparticle research.* Materials today, 2013. **16**(7-8): p. 262-271.
3. Pal, S.L., et al., *Nanoparticle: An overview of preparation and characterization.* Journal of applied pharmaceutical science, 2011(Issue): p. 228-234.
4. Joudeh, N. and D. Linke, *Nanoparticle classification, physicochemical properties, characterization, and applications: a comprehensive review for biologists.* J Nanobiotechnology, 2022. **20**(1): p. 262.
5. Kumar, H., et al., *Metallic nanoparticle: a review.* Biomed. J. Sci. Tech. Res, 2018. **4**(2): p. 3765-3775.
6. Mody, V.V., et al., *Introduction to metallic nanoparticles.* Journal of Pharmacy and bioallied sciences, 2010. **2**(4): p. 282-289.
7. Yan, X., et al., *Bioorthogonal "Click and Release" Reaction-Triggered Aggregation of Gold Nanoparticles Combined with Released Lonidamine for Enhanced Cancer Photothermal Therapy.* Angewandte Chemie International Edition, 2024. **63**(13): p. e202318539.
8. Siddique, A.B., et al., *Synthesis of hydroxyethylcellulose phthalate-modified silver nanoparticles and their multifunctional applications as an efficient antibacterial, photocatalytic and mercury-selective sensing agent.* International Journal of Biological Macromolecules, 2024. **256**: p. 128009.
9. Siqueira Jr, J. and O.N. Oliveira Jr, *Carbon-based nanomaterials*, in *Nanostructures*. 2017, Elsevier. p. 233-249.
10. Maiti, D., et al., *Carbon-based nanomaterials for biomedical applications: a recent study.* Frontiers in pharmacology, 2019. **9**: p. 1401.
11. Gupta, T.K., et al., *Advances in carbon based nanomaterials for bio-medical applications.* Current Medicinal Chemistry, 2019. **26**(38): p. 6851-6877.
12. Song, G., et al., *Hierarchical hollow carbon particles with encapsulation of carbon nanotubes for high performance supercapacitors.* Small, 2024. **20**(3): p. 2305517.
13. Lv, H., et al., *Functional nanoporous graphene superlattice.* Nature Communications, 2024. **15**(1): p. 1295.
14. Rao, J.P. and K.E. Geckeler, *Polymer nanoparticles: Preparation techniques and size-control parameters.* Progress in polymer science, 2011. **36**(7): p. 887-913.
15. Lu, X.-Y., et al., *Polymer nanoparticles.* Progress in molecular biology and translational science, 2011. **104**: p. 299-323.
16. Elsabahy, M. and K.L. Wooley, *Design of polymeric nanoparticles for biomedical delivery applications.* Chemical Society Reviews, 2012. **41**(7): p. 2545-2561.
17. Jafari-Gharabaghlou, D., et al., *Potentiation of Folate-Functionalized PLGA-PEG nanoparticles loaded with metformin for the treatment of breast Cancer: possible clinical application.* Molecular Biology Reports, 2023. **50**(4): p. 3023-3033.

18. Terna, A.D., et al., *The future of semiconductors nanoparticles: Synthesis, properties and applications.* Materials Science and Engineering: B, 2021. **272**: p. 115363.
19. Wang, Z., et al., *Organic semiconducting nanoparticles for biosensor: a review.* Biosensors, 2023. **13**(4): p. 494.
20. Kosco, J., et al., *Generation of long-lived charges in organic semiconductor heterojunction nanoparticles for efficient photocatalytic hydrogen evolution.* Nature Energy, 2022. **7**(4): p. 340-351.
21. García de Arquer, F.P., et al., *Semiconductor quantum dots: Technological progress and future challenges.* Science, 2021. **373**(6555): p. eaaz8541.
22. Cotta, M.A., *Quantum dots and their applications: what lies ahead?* 2020, ACS Publications. p. 4920-4924.
23. Gao, W., et al., *A review on mechanism, applications and influencing factors of carbon quantum dots based photocatalysis.* Ceramics International, 2022. **48**(24): p. 35986-35999.
24. Chung, S., R.A. Revia, and M. Zhang, *Graphene quantum dots and their applications in bioimaging, biosensing, and therapy.* Advanced Materials, 2021. **33**(22): p. 1904362.
25. Gil, H.M., et al., *NIR-quantum dots in biomedical imaging and their future.* Iscience, 2021. **24**(3).
26. Cai, S., et al., *Recent advance in surface modification for regulating cell adhesion and behaviors.* Nanotechnology Reviews, 2020. **9**(1): p. 971-989.
27. Baig, N., I. Kammakakam, and W. Falath, *Nanomaterials: A review of synthesis methods, properties, recent progress, and challenges.* Materials advances, 2021. **2**(6): p. 1821-1871.
28. Guo, Y., et al., *Surface chemical-modification for engineering the intrinsic physical properties of inorganic two-dimensional nanomaterials.* Chemical Society Reviews, 2015. **44**(3): p. 637-646.
29. Biju, V., *Chemical modifications and bioconjugate reactions of nanomaterials for sensing, imaging, drug delivery and therapy.* Chemical Society Reviews, 2014. **43**(3): p. 744-764.
30. Bagwe, R.P., L.R. Hilliard, and W. Tan, *Surface modification of silica nanoparticles to reduce aggregation and nonspecific binding.* Langmuir, 2006. **22**(9): p. 4357-4362.
31. Neouze, M.-A. and U. Schubert, *Surface modification and functionalization of metal and metal oxide nanoparticles by organic ligands.* Monatshefte für Chemie-Chemical Monthly, 2008. **139**: p. 183-195.
32. Srivastava, S. and N.A. Kotov, *Composite layer-by-layer (LBL) assembly with inorganic nanoparticles and nanowires.* Accounts of chemical research, 2008. **41**(12): p. 1831-1841.
33. Malikova, N., et al., *Layer-by-layer assembled mixed spherical and planar gold nanoparticles: control of interparticle interactions.* Langmuir, 2002. **18**(9): p. 3694-3697.
34. Kong, W., et al., *A general strategy for ligand exchange on upconversion nanoparticles.* Inorganic Chemistry, 2017. **56**(2): p. 872-877.
35. Hong, R., et al., *Surface PEGylation and ligand exchange chemistry of FePt nanoparticles for biological applications.* Chemistry of materials, 2005. **17**(18): p. 4617-4621.
36. Li, K. and B. Liu, *Polymer-encapsulated organic nanoparticles for fluorescence and photoacoustic imaging.* Chemical Society Reviews, 2014. **43**(18): p. 6570-6597.

37. Vrignaud, S., J.-P. Benoit, and P. Saulnier, *Strategies for the nanoencapsulation of hydrophilic molecules in polymer-based nanoparticles.* Biomaterials, 2011. **32**(33): p. 8593-8604.
38. Wu, C., C. Szymanski, and J. McNeill, *Preparation and encapsulation of highly fluorescent conjugated polymer nanoparticles.* Langmuir, 2006. **22**(7): p. 2956-2960.
39. Shang, L., K. Nienhaus, and G.U. Nienhaus, *Engineered nanoparticles interacting with cells: size matters.* Journal of nanobiotechnology, 2014. **12**(1): p. 1-11.
40. Barbero, F., et al. *Formation of the protein corona: the interface between nanoparticles and the immune system*. in *Seminars in immunology*. 2017. Elsevier.
41. Caracciolo, G., et al., *Stealth effect of biomolecular corona on nanoparticle uptake by immune cells.* Langmuir, 2015. **31**(39): p. 10764-10773.
42. Corbo, C., et al., *Personalized protein corona on nanoparticles and its clinical implications.* Biomaterials science, 2017. **5**(3): p. 378-387.
43. Lundqvist, M., et al., *The evolution of the protein corona around nanoparticles: a test study.* ACS nano, 2011. **5**(9): p. 7503-7509.
44. García-Álvarez, R. and M. Vallet-Regí, *Hard and soft protein corona of nanomaterials: Analysis and relevance.* Nanomaterials, 2021. **11**(4): p. 888.
45. Akhter, M.H., et al., *Impact of protein corona on the biological identity of nanomedicine: understanding the fate of nanomaterials in the biological milieu.* Biomedicines, 2021. **9**(10): p. 1496.
46. Lee, H., *Molecular modeling of protein corona formation and its interactions with nanoparticles and cell membranes for nanomedicine applications.* Pharmaceutics, 2021. **13**(5): p. 637.
47. Zhdanov, V.P. and N.-J. Cho, *Kinetics of the formation of a protein corona around nanoparticles.* Mathematical biosciences, 2016. **282**: p. 82-90.
48. Treuel, L., et al., *Protein corona–from molecular adsorption to physiological complexity.* Beilstein journal of nanotechnology, 2015. **6**(1): p. 857-873.
49. Liu, X., C. Yan, and K.L. Chen, *Adsorption of human serum albumin on graphene oxide: implications for protein corona formation and conformation.* Environmental Science & Technology, 2018. **53**(15): p. 8631-8639.
50. Kopac, T., *Protein corona, understanding the nanoparticle–protein interactions and future perspectives: A critical review.* International Journal of Biological Macromolecules, 2021. **169**: p. 290-301.
51. Sadeghi, A., et al., *Polymeric nanoparticles and nanogels: how do they interact with proteins?* Gels, 2023. **9**(8): p. 632.
52. Panico, S., et al., *Biological features of nanoparticles: protein corona formation and interaction with the immune system.* Pharmaceutics, 2022. **14**(12): p. 2605.
53. Piella, J., N.G. Bastús, and V. Puntes, *Size-dependent protein–nanoparticle interactions in citrate-stabilized gold nanoparticles: the emergence of the protein corona.* Bioconjugate chemistry, 2017. **28**(1): p. 88-97.
54. Bilardo, R., et al., *Influence of surface chemistry and morphology of nanoparticles on protein corona formation.* Wiley Interdisciplinary Reviews: Nanomedicine and Nanobiotechnology, 2022. **14**(4): p. e1788.

55. Lundqvist, M., et al., *Nanoparticle size and surface properties determine the protein corona with possible implications for biological impacts.* Proceedings of the National Academy of Sciences, 2008. **105**(38): p. 14265-14270.
56. Gref, R., et al., *'Stealth'corona-core nanoparticles surface modified by polyethylene glycol (PEG): influences of the corona (PEG chain length and surface density) and of the core composition on phagocytic uptake and plasma protein adsorption.* Colloids and Surfaces B: Biointerfaces, 2000. **18**(3-4): p. 301-313.
57. González-García, L.E., et al., *Nanoparticles surface chemistry influence on protein corona composition and inflammatory responses.* Nanomaterials, 2022. **12**(4): p. 682.
58. Tomak, A., et al., *Nanoparticle-protein corona complex: understanding multiple interactions between environmental factors, corona formation, and biological activity.* Nanotoxicology, 2021. **15**(10): p. 1331-1357.
59. Ge, C., et al., *Towards understanding of nanoparticle–protein corona.* Archives of toxicology, 2015. **89**: p. 519-539.
60. Carrillo-Carrion, C., M. Carril, and W.J. Parak, *Techniques for the experimental investigation of the protein corona.* Current Opinion in Biotechnology, 2017. **46**: p. 106-113.
61. Carril, M., et al., *In situ detection of the protein corona in complex environments.* Nature communications, 2017. **8**(1): p. 1542.
62. Wang, H., et al., *The protein corona on nanoparticles as viewed from a nanoparticle‐sizing perspective.* Wiley Interdisciplinary Reviews: Nanomedicine and Nanobiotechnology, 2018. **10**(4): p. e1500.
63. Givens, B.E., E. Wilson, and J. Fiegel, *The effect of salts in aqueous media on the formation of the BSA corona on SiO2 nanoparticles.* Colloids and Surfaces B: Biointerfaces, 2019. **179**: p. 374-381.
64. Pujol-Vila, F., et al., *Nanoplasmonic paper-based platform for general screening of biomacromolecules.* Nanomaterials, 2020. **10**(12): p. 2335.
65. Fologea, D., et al., *Electrical characterization of protein molecules by a solid-state nanopore.* Applied physics letters, 2007. **91**(5).
66. González Flecha, F.L. and V. Levi, *Determination of the molecular size of BSA by fluorescence anisotropy.* Biochemistry and molecular biology education, 2003. **31**(5): p. 319-322.
67. Vincent, J.B. and S. Love, *The binding and transport of alternative metals by transferrin.* Biochimica et Biophysica Acta (BBA)-General Subjects, 2012. **1820**(3): p. 362-378.
68. Altamura, S., et al., *Regulation of iron homeostasis: Lessons from mouse models.* Molecular Aspects of Medicine, 2020. **75**: p. 100872.
69. Vesterberg, O. and U. Breig, *Quantitative analysis of multiple molecular forms of transferrin using isoelectric focusing and zone immunoelectrophoresis assay (ZIA).* Journal of Immunological Methods, 1981. **46**(1): p. 53-62.
70. Martel, P., S. Kim, and B. Powell, *Physical characteristics of human transferrin from small angle neutron scattering.* Biophysical Journal, 1980. **31**(3): p. 371-380.
71. Fruton, J.S., *Specificity and mechanism of pepsin action.* Structure–Function Relationships of Proteolytic Enzymes, 1970: p. 222-236.
72. Fruton, J.S., *A history of pepsin and related enzymes.* The Quarterly Review of Biology, 2002. **77**(2): p. 127-147.

73. Giussani, L., et al., *On the compatibility criteria for protein encapsulation inside mesoporous materials.* ChemPhysChem, 2010. **11**(8): p. 1757-1762.
74. Piper, D. and B.H. Fenton, *pH stability and activity curves of pepsin with special reference to their clinical importance.* Gut, 1965. **6**(5): p. 506.
75. Chipman, D.M. and N. Sharon, *Mechanism of Lysozyme Action: Lysozyme is the first enzyme for which the relation between structure and function has become clear.* Science, 1969. **165**(3892): p. 454-465.
76. Salton, M., *The properties of lysozyme and its action on microorganisms.* Bacteriological reviews, 1957. **21**(2): p. 82-100.
77. van der Veen, M., W. Norde, and M.C. Stuart, *Electrostatic interactions in protein adsorption probed by comparing lysozyme and succinylated lysozyme.* Colloids and Surfaces B: Biointerfaces, 2004. **35**(1): p. 33-40.
78. Green, N.M., *Avidin*, in *Advances in protein chemistry*. 1975, Elsevier. p. 85-133.
79. Lesch, H.P., et al., *Avidin-biotin technology in targeted therapy.* Expert opinion on drug delivery, 2010. **7**(5): p. 551-564.
80. Rosano, C., P. Arosio, and M. Bolognesi, *The X-ray three-dimensional structure of avidin.* Biomolecular Engineering, 1999. **16**(1-4): p. 5-12.
81. Li, J.J., et al., *Large-Scale Synthesis of Nearly Monodisperse CdSe/CdS Core/Shell Nanocrystals Using Air-Stable Reagents via Successive Ion Layer Adsorption and Reaction.* Journal of the American Chemical Society, 2003. **125**(41): p. 12567-12575.
82. Zhou, J., et al., *Ideal CdSe/CdS Core/Shell Nanocrystals Enabled by Entropic Ligands and Their Core Size-, Shell Thickness-, and Ligand-Dependent Photoluminescence Properties.* Journal of the American Chemical Society, 2017. **139**(46): p. 16556-16567.
83. Magde, D., R. Wong, and P.G. Seybold, *Fluorescence quantum yields and their relation to lifetimes of rhodamine 6G and fluorescein in nine solvents: Improved absolute standards for quantum yields¶.* Photochemistry and photobiology, 2002. **75**(4): p. 327-334.
84. Grabolle, M., et al., *Determination of the fluorescence quantum yield of quantum dots: suitable procedures and achievable uncertainties.* Analytical chemistry, 2009. **81**(15): p. 6285-6294.
85. Samoc, A., *Dispersion of refractive properties of solvents: Chloroform, toluene, benzene, and carbon disulfide in ultraviolet, visible, and near-infrared.* Journal of Applied Physics, 2003. **94**(9): p. 6167-6174.
86. Jiménez Riobóo, R., et al., *Concentration and temperature dependence of the refractive index of ethanol-water mixtures: Influence of intermolecular interactions.* The European Physical Journal E, 2009. **30**: p. 19-26.
87. Geißler, D., et al., *Excitation wavelength dependence of the photoluminescence quantum yield and decay behavior of CdSe/CdS quantum dot/quantum rods with different aspect ratios.* Physical Chemistry Chemical Physics, 2017. **19**(19): p. 12509-12516.
88. Martynenko, I.V., et al., *Excitation energy dependence of the photoluminescence quantum yield of core/shell CdSe/CdS quantum dots and correlation with circular dichroism.* Chemistry of Materials, 2018. **30**(2): p. 465-471.
89. Sadeghi, S., et al., *Efficient white LEDs using liquid-state magic-sized CdSe quantum dots.* Scientific reports, 2019. **9**(1): p. 10061.
90. Berry, J.D., et al., *Measurement of surface and interfacial tension using pendant drop tensiometry.* Journal of colloid and interface science, 2015. **454**: p. 226-237.

91. Hua, X.Y. and M.J. Rosen, *Dynamic surface tension of aqueous surfactant solutions: I. Basic paremeters.* Journal of Colloid and Interface Science, 1988. **124**(2): p. 652-659.
92. Aliyandi, A., et al., *Cell surface biotinylation to identify the receptors involved in nanoparticle uptake into endothelial cells.* Acta Biomaterialia, 2023. **155**: p. 507-520.
93. Yudhistira, T., et al., *Biotinylated fluorescent polymeric nanoparticles for enhanced immunostaining.* Small Methods, 2023. **7**(4): p. 2201452.
94. Li, P.Y., et al., *PEGylation enables subcutaneously administered nanoparticles to induce antigen-specific immune tolerance.* Journal of controlled release, 2021. **331**: p. 164-175.
95. Suk, J.S., et al., *PEGylation as a strategy for improving nanoparticle-based drug and gene delivery.* Advanced drug delivery reviews, 2016. **99**: p. 28-51.
96. Del Pino, P., et al., *Protein corona formation around nanoparticles–from the past to the future.* Materials Horizons, 2014. **1**(3): p. 301-313.
97. Vilanova, O., et al., *Understanding the kinetics of protein–nanoparticle corona formation.* ACS nano, 2016. **10**(12): p. 10842-10850.
98. Gebauer, J.S., et al., *Impact of the nanoparticle–protein corona on colloidal stability and protein structure.* Langmuir, 2012. **28**(25): p. 9673-9679.

Eidesstattliche

Versicherung/Declaration on Oath

Hiermit versichere ich an Eides statt, die vorliegende Dissertationsschrift selbst verfasst und keine anderen als die angegebenen Quellen und Hilfsmittel benutzt zu haben. Ein Teil der Sprache in dieser Arbeit wurde von chatgpt verfeinert, Sofern im Zuge der Erstellung der vorliegenden Dissertationsschrift generative Künstliche Intelligenz (gKI) basierte elektronische Hilfsmittel verwendet wurden, versichere ich, dass meine eigene Leistung im Vordergrund stand und dass eine vollständige Dokumentation aller verwendeten Hilfsmittel gemäß der Guten wissenschaftlichen Praxis vorliegt. Ich trage die Verantwortung für eventuell durch die gKI generierte fehlerhafte oder verzerrte Inhalte, fehlerhafte Referenzen, Verstöße gegen das Datenschutz- und Urheberrecht oder Plagiate.

Chenxi Yang

Hamburg. 10.10.2024

Acknowledgement

This research could not have been accomplished without the invaluable contributions of many remarkable individuals, each of whom played a vital. I would like to begin by expressing my gratitude to my supervisors, Professor Wolfgang Parak, Professor Alf Mews, Dr. Neus Feliu, and Dr. Florian Schulz. I am particularly thankful to Professor Wolfgang Parak for inviting me to be part of the team at the University of Hamburg and for the opportunity to pursue my doctoral research. I appreciate his vision in designing this comprehensive project, his guidance during challenging phases, and, most importantly, for teaching me how to think critically, interpret, and analyze data in a way that adds coherence and narrative to my research. Throughout my doctoral journey, I gained the ability to apply fundamental knowledge and tools to address complex questions effectively.

I would also like to thank Dr. Florian Schulz for his advice, support and discussions, especially in the writing and optimization of the thesis, which greatly enriched my research work during my doctoral studies.

I would like to thank Dr. Saad Mehmed for helping me with my first response and getting accustomed to the team, and Dr. David for showing me the quantum dots synthesis. I would like to thank Dr. Bing Qi for sharing his insights and advice on protein coronas, Dr. Tianyu Niu from the department of chemistry for helping me when I could not order chemical reagents, and a special thanks to my colleague and friend Dr. Miao Feng for always encouraging and supporting me. I would like to thank my friendly colleagues in the laboratory, Kai-wei Lin, Marie-Charlot Dalchow, Maya Luongo, Jinrui Li, Yuxuan Han, Wenbo Wang, Sarodi Jonak Dutta, Martin Sosniok, Juan Jesus Barrios, Ben Otange, Fernanda, Wanzhu Zhao, Xin Liu, Maria Pozzi, Marvin Skiba, Nils Dageförde we are a harmonious group.

I would like to express my sincere gratitude to PIER Helmholtz Graduate School for providing me with the opportunity to learn various soft skills during my doctoral career. I would also like to thank them for their financial support, which gave me the opportunity to go abroad to attend conferences. I would like to thank MIN faculty for their financial support, which gave me the opportunity to go abroad to attend conferences. I would like to thank the China Scholarship Council for their support, which allowed me to get a scholarship to pursue my doctorate and covered the cost of my study abroad.

Finally, I would like to thank my family and friends in Germany and China for their unconditional support and love. I would like to thank my parents for giving me emotional support all the time. I would like to thank my friends in China for encouraging and

supporting me. I would like to thank the friends I met in Germany for helping me adapt to the German culture and environment better.

List of Hazardous Substances

List of Chemicals and GHS Classifications.

Substance	Signal word	GHS-symbols	Hazard statements	Precautionary statements
Chloroform	Danger		H302 - H315 - H319 - H331 - H336 - H351 - H361d - H372	P202 - P301 + P312 - P302 + P352 - P304 + P340 + P311 - P305 + P351 + P338 - P308 + P313
Cadmium oxide	Danger		H330 - H341 - H350 - H361fd - H372 - H410	P202 - P260 - P264 - P270 - P273 - P304 + P340 + P310
Trioctylphosphine oxide	Danger		H315 - H318 - H412	P264 - P273 - P280 - P302 + P352 - P305 + P351 + P338 - P332 + P313
Trioctylphosphine	Danger		H314	
Selenium	Danger		H301 + H331 - H373 - H413	P260 - P264 - P273 - P301 + P310 - P304 + P340 + P311 - P314
1-octadecene	Danger		H304	P301 + P310 - P331 - P405 - P501
Hydrochloric acid	Danger		H290 - H314 - H335	P234 - P261 - P271 - P280 - P303 + P361 + P353 - P305 + P351 + P338

Nitric acid	Danger		H272 - H290 - H314 - H331	P210 - P220 - P280 - P303 + P361 + P353 - P304 + P340 + P310 - P305 + P351 + P338
Ethanol	Danger		H225 - H319	P210 - P233 - P240 - P241 - P242 - P305 + P351 + P338
N,N-Dimethyldodecylamine	Danger		H302 - H314 - H410	P270 - P273 - P280 - P301 + P312 - P303 + P361 + P353 - P305 + P351 + P338
Cyclohexane	Danger		H225 - H304 - H315 - H336 - H410	P210 - P233 - P273 - P301 + P310 - P303 + P361 + P353 - P331
Ammonium chloride	Warning		H302 - H319	P264 - P270 - P280 - P301 + P312 - P305 + P351 + P338 - P337 + P313
Sodium hydroxide	Danger		H290 - H314	P234 - P260 - P280 - P303 + P361 + P353 - P304 + P340 + P310 - P305 + P351 + P338
Methanol	Danger		H225 - H301 + H311 + H331 - H370	P210 - P233 - P280 - P301 + P310 - P303 + P361 + P353 - P304 + P340 + P311

Tetrahydrofuran	Danger		H225 - H302 - H319 - H335 - H336 - H351	P202 - P210 - P233 - P301 + P312 - P305 + P351 + P338 - P308 + P313
Toluene	Danger		H225 - H304 - H315 - H336 - H361d - H373 - H412	P202 - P210 - P273 - P301 + P310 - P303 + P361 + P353 - P331